Journal of Research

of the

National Bureau of Standards

UNIVERSITY OF MICHIGAN
AUG 13 1956
PHYSICS LIBRARY

JULY 1956

VOLUME 57 NUMBER 1

U. S. DEPARTMENT OF COMMERCE
Sinclair Weeks, Secretary
NATIONAL BUREAU OF STANDARDS
A. V. Astin, Director

JULY • 1956
VOLUME • 57
NUMBER • 1

JOURNAL OF RESEARCH

of the

NATIONAL BUREAU OF STANDARDS

PERIODICALS OF THE NATIONAL BUREAU OF STANDARDS

(Published monthly)

The National Bureau of Standards is engaged in fundamental and applied research in physics, chemistry, mathematics, and engineering. Projects are conducted in fifteen fields: electricity and electronics, optics and metrology, heat and power, atomic and radiation physics, chemistry, mechanics, organic and fibrous materials, metallurgy, mineral products, building technology, applied mathematics, data processing systems, cryogenic engineering, radio propagation, and radio standards. The Bureau has custody of the national standards of measurement and conducts research leading to the improvement of scientific and engineering standards and of techniques and methods of measurement. Testing methods and instruments are developed; physical constants and properties of materials are determined; and technical processes are investigated.

JOURNAL OF RESEARCH

The Journal presents research papers by authorities in the specialized fields of physics, mathematics, chemistry, and engineering. Complete details of the work are presented, including laboratory data, experimental procedures, and theoretical and mathematical analyses. Annual subscription: domestic, $4.00; $1.25 additional for foreign mailing.

TECHNICAL NEWS BULLETIN

Summaries of current research at the National Bureau of Standards are published each month in the Technical News Bulletin. The articles are brief, with emphasis on the results of research, chosen on the basis of their scientific or technologic importance. Lists of all Bureau publications during the preceding month are given, including Research Papers, Handbooks, Applied Mathematics Series, Building Materials and Structures Reports, Miscellaneous Publications, and Circulars. Each issue contains 12 or more two-column pages; illustrated. Annual subscription: domestic, $1.00; 35 cents additional for foreign mailing.

BASIC RADIO PROPAGATION PREDICTIONS

The Predictions provide the information necessary for calculating the best frequencies for communication between any two points in the world at any time during the given month. The data are important to all users of long-range radio communications and navigation, including broadcasting, airline, steamship, and wireless services, as well as to investigators of radio propagation and ionosphere. Each issue, covering a period of one month, is released three months in advance and contains 16 large pages, including pertinent charts, drawings, and tables. Annual subscription: domestic, $1.00; 25 cents additional for foreign mailing.

Order all publications from the Superintendent of Documents
U. S. Government Printing Office, Washington 25, D. C.

The printing of this publication has been approved by the Director of the Bureau of the Budget, May 14, 1956.

Journal of Research of the National Bureau of Standards Vol. 57, No. 1, July 1956 Research Paper 2687

Mixed Path Ground Wave Propagation: 1. Short Distances

James R. Wait

An expression is derived for the mutual impedance between two short vertical antennas on a flat earth with a straight boundary separating two media of differing electrical constants. After making some approximations that are valid at low and medium frequencies and where the antennas are not near the boundary, the integral formula for the field is evaluated for a wide range of the parameters. The numerical results computed in this paper are shown to be in reasonably good agreement with experiment. Finally, the effect of the obliqueness of the boundary is considered by a refinement of the stationary phase evaluation of the integrals.

1. Introduction

Considerable interest has been shown recently in the propagation of ground waves over an inhomogeneous conducting earth. For many purposes, such as estimating coverage of broadcast transmitters, it is usually sufficient to assign an equivalent conductivity to the path. A simple and effective method for estimating this equivalent value from a conductivity profile of the path has recently been proposed by Suda [1].[1] Another technique described by Kirke [2], which is similar, has been called the equivalent-distance method and is also simple to apply. The best known method, however, is due to Millington [3]. Although semiempirical it does appear to be valid for a wide range of frequencies and ground constants. It also predicts the recovery effect that occurs when the wave passes over a boundary from an area of poor conductivity to one of good conductivity. Millington does not provide a theoretical justification for his method, although he does indicate that his formulas for high frequencies are compatible with the expected behavior of the height-gain functions over the media on both sides of the boundary. Clemmow [4] in an elegant dissertation obtains a rigorous solution for a line source on flat earth parallel to a boundary separating two media. He makes a limited comparison of his formula with Millington's method, and shows that the agreement is good. In a more recent theoretical approach to the subject, Bremmer [5] formulates the problem in terms of an integral equation, which he solves by operational methods. After considerable manipulation he succeeds in showing that his result is mathematically equivalent to that of Clemmow. Bremmer considers several limiting cases and also establishes the validity of Millington's formulas at high frequencies.

It is the purpose of the present paper to extend Bremmer's result, with particular attention being paid to the phenomena at low and medium radiofrequencies where it does not seem possible to obtain convenient series expansions for the field by the Bremmer method. For the sake of completeness, the problem is reformulated in terms of mutual impedance between two antennas located on a flat earth, with a straight boundary separating two homogeneous media. In this case there is no doubt as to whether the reciprocity theorem is satisfied or not. The line joining the two antennas makes some angle with the boundary that should not be near zero. An integral equation is obtained for the field which is similar to one formulated by Feinberg [6] for propagation over a rough ground. In the present paper, the integral equation is solved by numerical means for a range of parameters that are appropriate for short distances at low and medium frequencies. It is intended to extend the calculations in a later paper to situations where the earth's curvature must be considered; that is, for distances in miles greater than about $50\lambda^{1/3}$, where λ is the wavelength in meters.

[1] Figures in brackets indicate the literature references at the end of this paper.

2. Formulation

The surface of the earth is considered to be flat and defined by $z=0$ in a simple cartesian coordinate system (x,y,z). Points above the earth correspond to positive values of z. The earth medium to the left of a boundary line defined by $y=x \tan \theta$, as indicated in figure 1, has a conductivity σ and dielectric constant ϵ. The earth medium for points to the right of the boundary line has a conductivity of σ_1 and dielectric constant ϵ_1. Short hertzian dipole antennas are located at the points A and B, which can be located anywhere along the x axis just above the surface of the ground at $z=0$.

It is now assumed that a current I_a applied at the terminals of antenna A would produce electric and magnetic fields $\overline{E}_a$ and $\overline{H}_a$ for the case when the earth media were homogeneous with electrical constants σ and ϵ. A time factor $\exp(i\omega t)$ is implied. The mutual impedance between antennas A and B for this homogeneous case is denoted as Z_{ab}. When the earth becomes inhomogeneous in the manner described above, the fields of antenna A with the same current I_a become $\overline{E}'_a$ and $\overline{H}'_a$, and the mutual impedance becomes Z'_{ab}. It is convenient to regard the change from Z'_{ab} to Z_{ab} as a consequence of the changes of the currents within the earth when it is transformed from a homogeneous to an inhomogeneous state. These currents will result in electric and magnetic fields $\overline{E}'_a - \overline{E}_a$ and $\overline{H}'_a - \overline{H}_a$ and a voltage $I_a(Z_{ab}-Z'_{ab})$ at the terminals of antenna B. A current I_b is now considered to be applied at terminals of antenna B, and the resulting electric and magnetic fields are $\overline{E}_b$ and $\overline{H}_b$ over the homogeneous earth of constants σ and ϵ. It then follows from Ballentine's "corollary I" of the electromagnetic reciprocity theorem [7,8] that

$$Z'_a - Z_{ab} = \frac{1}{I_a I_b} \int \int_S [\overline{E}_b \times \overline{H}'_a - \overline{E}'_a \times \overline{H}_b]_z \, dx \, dy, \tag{1}$$

where the integration extends over the whole ground plane S, and the subscript z indicates that the z or normal component of vector products is taken.

A simplification is now made by introducing the concept of surface impedance [6,8], that is, the tangential electric and magnetic fields on the surface of the earth are assumed to be related by a complex constant of proportionality. More specifically,

$$\left.\begin{aligned} E_x &\simeq -\eta H_y \\ E_y &\simeq \eta H_x \end{aligned}\right\} \tag{2}$$

where η, the surface impedance, is assumed to be equal to the value obtained for a plane wave at grazing incidence on the flat earth. It is given by

$$\eta = 120\pi \frac{i\beta}{\alpha}\left[1+\frac{\beta^2}{\alpha^2}\right]^{\frac{1}{2}}, \tag{3}$$

where $\beta = 2\pi/\text{wavelength}$, and $\alpha = (i\sigma\mu\omega - \epsilon\mu\omega^2)^{\frac{1}{2}}$, with $\mu = 4\pi \times 10^{-7}$. A subscript 1 is to be added to η when the electric constants are σ_1 and ϵ_1.

Equation (1) can now be written

$$I_a I_b \Delta Z = (\eta - \eta_1) \iint_{S_0} (\overline{H}'_{at} \cdot \overline{H}_{bt}) dx dy, \tag{4}$$

where $\Delta Z = Z'_{ab} - Z_{ab}$ is the change of the mutual impedance from the situation of the homogeneous earth of surface impedance η to the inhomogeneous model indicated in figure 1. The quantity $\overline{H}_{bt}$ is the tangential magnetic field of the antenna B over the homogeneous earth, and $\overline{H}_{at}$ is the tangential magnetic field of the antenna A over the inhomogeneous earth.

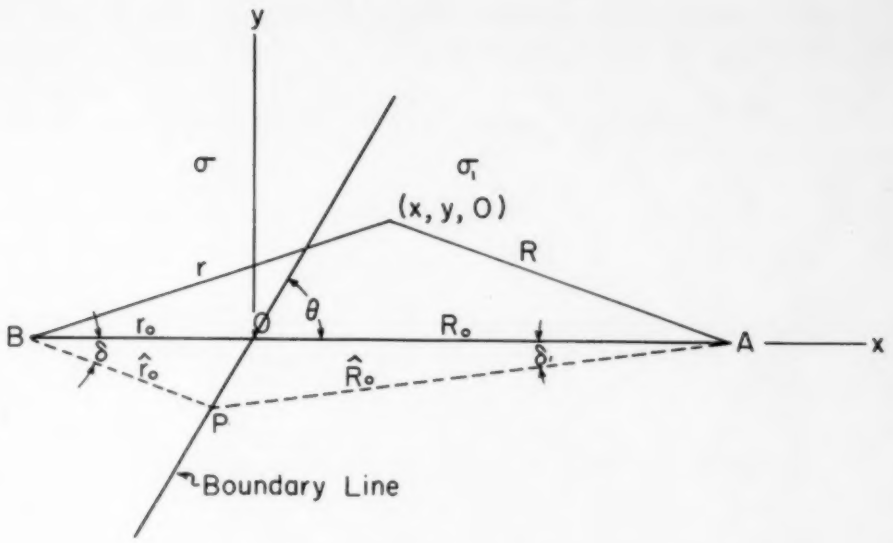

FIGURE 1. *Schematic diagram of antennas A and B on a flat earth with a straight boundary separating two media with different conductivities.*

The integration now extends over the surface S_0 to the right of the boundary line. Since $\overline{H}_{at}$ is not actually known, eq (4) is actually a surface integral equation formulation of the problem. Before attempting to solve it, a simplification can be made if the principle of stationary phase is utilized.

Letting the hertzian antenna at B have an effective height h_b, the tangential magnetic field at P, a distance r from B, considering the earth as homogeneous and flat, is given by

$$\overline{H}_{bt}=\frac{i\beta I_b h_b}{2\pi r}\, e^{-i\beta r}\left(1+\frac{1}{i\beta r}\right) F(r,\eta)(\overline{i}_r\times\overline{i}_z), \tag{5}$$

where $F(r,\eta)$ is Sommerfeld's ground-wave attenuation factor defined by

$$F(r,\eta)=1-i2p^{1/2}e^{-p}\int_{\alpha=ip^{1/2}}^{\infty} e^{-\alpha^2}d\alpha, \tag{6}$$

where

$$p=+\frac{i\beta r}{2}\,\frac{\beta^2}{\alpha^2}\left(1+\frac{\beta^2}{\alpha^2}\right)=-\frac{i\beta r}{2}\left(\frac{\eta}{120\pi}\right)^2$$

is the numerical distance. Equation (6) is not exact, being an approximation valid for $\beta^2\ll|\alpha|^2$. $\overline{i}_r$ and $\overline{i}_z$ are unit vectors in the directions of increasing r and z, respectively. The function $F(r,\eta)$ has been treated numerically by Norton [9] and others. The tangential magnetic field $\overline{H}'_{at}$ at a distance R from A is of the form

$$\overline{H}'_{at}=\frac{i\beta I_a h_a}{2\pi R}\, e^{-i\beta R}\left(1+\frac{1}{i\beta R}\right) F'(R,\eta,\eta_1)(\overline{i}_R\times\overline{i}_z), \tag{7}$$

where $F'(R,\eta,\eta_1)$ is some function of R, η, and η_1, and can be expected to be slowly varying compared to $e^{-i\beta R}$. $\overline{i}_R$ is a unit vector in the direction of increasing R.

Using eq (5) and (7) and denoting the angle between the vectors $\bar{i}_r$ and $\bar{i}_R$ as $\underline{\delta}$, it follows that the expression for the mutual increment ΔZ can be written

$$\Delta Z=-(\eta-\eta_1)\frac{\beta^2 h_a h_b}{4\pi^2}\iint_{S_0}\frac{e^{-i\beta(r+R)}}{rR}\left(1+\frac{1}{i\beta r}\right)\left(1+\frac{1}{i\beta R}\right)F(r,\eta)\times F'(r,\eta,\eta_1)\cos\underline{\delta}\,dxdy, \tag{8}$$

where

$$r=[(r_0+x)^2+y^2]^{1/2} \text{ and}$$

$$R=[(R_0-x)^2+y^2]^{1/2}.$$

The major contribution to the integrand occurs when the phase of the exponential term is nearly constant, since the others are relatively slowly varying. With this in mind, the exponent is expanded in a powers series in y^2 as follows:

$$r+R\simeq r_0+R_0+\frac{y^2}{2}\left[\left(\frac{1}{r_0+x}\right)+\left(\frac{1}{R_0-x}\right)\right] \text{ for } R_0>x>0$$

and

$$r+R\simeq r_0-R_0+2x+\frac{y^2}{2}\left[\left(\frac{1}{r_0+x}\right)+\left(\frac{1}{x-R_0}\right)\right] \text{ for } x>R_0, \tag{9}$$

where terms in y^4, y^6, etc., are neglected. A further approximation to the integrand in eq (8) is to replace $(1+1/i\beta r)$ and $(1+1/i\beta R)$ by unity. This will be justified if the antenna A or B is not near the boundary (i. e., βR_0 and $\beta r_0 \gg 1$). This is essentially equivalent to stating that the effect of the induction field of the antennas is not considered so far as the boundary is concerned.

The integral expression for ΔZ now has the following approximate form:

$$\Delta Z=+\frac{(\eta_1-\eta)\beta^2 h_a h_b}{(2\pi)^2}\frac{e^{-i\beta(r_0+R_0)}}{(r_0+R_0)^{\frac{1}{2}}}\int_{x=0}^{R_0}\frac{F(r_0+x,\eta)F'(R_0-x,\eta,\eta_1)}{(r_0+x)(R_0-x)}\times\left[\int_{-\infty}^{+\infty}e^{-i\alpha^2y^2}\,dy\right]dx, \tag{10}$$

where

$$\alpha^2=\frac{\beta}{2}\left[\frac{R_0+r_0}{(r_0+x)(R_0-x)}\right].$$

The integration over x only extends from 0 to R_0, because the contribution from the integrand for $x>R_0$ is negligible due to the presence of the rapidly varying function $e^{-2i\beta x}$.

3. Numerical Solution

The mutual impedance Z between the two short antennas A and B for the homogeneous ground of electrical constants σ and ϵ is given by

$$Z=\frac{h_a h_b i\mu\omega}{2\pi(r_0+R_0)}e^{-i\beta(r_0+R_0)}F(r_0+R_0,\eta)\left[1+\frac{1}{i\beta(r_0+R_0)}-\frac{1}{\beta^2(r_0+R_0)^2}\right]. \tag{11}$$

It is now convenient to express the mutual impedance Z' between the antennas on the inhomogeneous ground as follows:

$$Z'=\frac{h_a h_b i\mu\omega}{2\pi(r_0+R_0)}e^{-i\beta(r_0+R_0)}F'(r_0+R_0,\eta_1,\eta)\left[1+\frac{1}{i\beta(r_0+R_0)}-\frac{1}{\beta^2(r_0+R_0)^2}\right], \tag{12}$$

where F' is the unknown attenuation function. The latter bracketed term can be replaced by unity because $\beta(r_0+R_0)$ is large compared to 1. Employing eq (10), (11) and (12), it follows that

$$F'(r+R_0,\eta,\eta_1)\simeq F(r_0+R_0,\eta)-i\epsilon_0\omega(\eta-\eta_1)\left(\frac{d^{1/2}}{2\pi i\beta}\right)\int_0^{R_0}\frac{F(r_0+x,\eta)F'(R_0-x,\eta_1,\eta)dx}{[(r_0+x)(R_0-x)]^{\frac{1}{2}}}. \tag{13}$$

This is an integral equation for F'. It is immediately apparent when $x<0$ such that A and B are to the left of the boundary

$$F'(r_0+R_0,\eta,\eta_1)\simeq F(r_0+R_0,\eta).$$

In other words, subject to our stationary phase approximation, the attenuation function F' between A and B, when they are located on one side of the boundary, is characteristic only of the electrical constants σ and ϵ of the homogeneous ground between them. For exactly the same reason, the function $F'(r_0+x,\eta,\eta_1)$, where it occurs in the integrand of equation, for the general case of $x>0$, can be replaced by $F(r_0+x,\eta_1)$, which is characteristic of propagation from A to the point $x(>0)$ over a homogeneous ground of electrical constants σ_1 and ϵ_1.

After a change of variable, the final expression for F' can be written in dimensionless form, yielding

$$F'=F(p_0)-i\left(\frac{p_0}{\pi}\right)^{\frac{1}{2}}(1-\sqrt{K})\int_0^{p_0V/K}\frac{F(p)F(p_0-Kp)}{\sqrt{p(p_0-Kp)}}dp \tag{14}$$

with [2]

$$F(p)=1-i2p^{\frac{1}{2}}e^{-p}\int_{ip^{1/2}}^{\infty}e^{-\alpha^2}d\alpha$$

and

$$p_0=-\frac{i\beta(r_0+R_0)}{2}\left(\frac{\eta}{120\pi}\right)^2$$

$$K=\frac{\sigma_1+i\omega\epsilon_1}{\sigma+i\omega\epsilon}\quad\text{and}\quad V=\frac{R_0}{R_0+r_0}.$$

The above expression for F' is then given in terms of the attenuation function $F(p_0)$, characteristic of propagation between A and B on a homogeneous ground, and a correction term that accounts for the change of the electrical constants of the ground to the right of the boundary. It should be noted that p_0 is the "numerical distance" between A and B with regard to the earth medium to the left of the boundary, whereas p_0V/K is the numerical distance between the boundary to the point B with regard to the earth medium to the right of the boundary. Unfortunately this expression, which involves an integration over products of error functions, is not readily expressible in closed form. However, the integral can be approximated in certain limiting cases. For example, when $p_0(1-V)$ and p_0V/K are small compared to 1, the power series expansion for the functions $F(p)$ and $F(p_0-Kp)$ can be employed. This has the form

$$F(p)=1-i(\pi p)^{\frac{1}{2}}-2p+i\sqrt{\pi}p^{\frac{3}{2}}\pm\text{ ---------}. \tag{15}$$

It then follows without difficulty that

$$F'=F(p_0)+2i\left(\frac{p_0}{\pi}\right)^{\frac{1}{2}}\left(1-\frac{1}{\sqrt{K}}\right)\tan^{-1}\left(\frac{V}{1-V}\right)-2p_0(1-\sqrt{K})\left[\frac{1}{K}(1-\sqrt{1-V})+\left(\frac{V}{K}\right)^{\frac{1}{2}}\right], \tag{16}$$

[2] For large distances, the function F must be modified to account for earth curvature. This will be considered in section 2.

plus terms in $p_0^{3/2}$, p_0^2, etc. Another special case is when p_0 is large compared to 1, so that only the leading term in the asymptotic expansion of $F(p_0-Kp)$ need be considered; and furthermore, V is assumed to be small compared to unity. In this instance

$$\frac{F(p_0-Kp)}{(p_0-Kp)^{1/2}} \simeq -\frac{1}{2(p_0-Kp)^{3/2}} \simeq -\frac{1}{2p_0^{3/2}}.$$

The power series formula for $F(p)$ is then employed, yielding, after integrating term by term:

$$\frac{F'}{F(p_0)} \simeq 1-\frac{2i(1-\sqrt{K})}{\sqrt{\pi}}\left[p_1^{1/2}-\frac{i\sqrt{\pi}}{2}p_1-\frac{2p_1^{3/2}}{3}+\frac{i\sqrt{\pi}}{4}p_1^2+\frac{4}{3}\frac{p_1^{5/2}}{5}-\frac{i\sqrt{\pi}}{2}\frac{p_1^3}{6}-\frac{8}{15}\frac{p_1^{7/2}}{7}+\cdots\right], \quad (17)$$

where $p_1=p_0V/K$.

There are probably other limiting cases which will enable the integration with respect to p to be effected; however, it is believed that for application to low and medium radiofrequencies the values of p_0 are in general neither large nor small compared to one. With this in mind, it is considered desirable to evaluate F' by a numerical integration for a range of p_0, V, and K. It should be noted that, for the general case, p_0 and K are complex so there are actually five parameters to consider for the two-media problem. In this paper, attention will be restricted to frequencies where the displacement currents in the ground can be neglected. That is, the ratios $\epsilon\omega/\sigma$ and $\epsilon_1\omega/\sigma_1$ are assumed to be small compared to unity, therefore $p_0=\pi[(R_0+r_0)/\lambda]$ $(\epsilon_0\omega/\sigma)$ and $K(=\sigma_1/\sigma)$ are real quantities. This is usually justified for frequencies less than 1,000 kc for typical ground constants [10].

Employing the numerical values of the function $F(p)$ and $F(p_0-Kp)$. the integral in eq (14) is evaluated by a graphical method. The function $F'(p_0, V,K)$ is then plotted as a function of p_0 from 0.1 to 5 for various values of K and V in figures 2 to 11. It is believed that the results plotted in this form can be adapted to a large number of practical situations. The curves are not shown beyond $p_0=5$, since this usually corresponds to higher frequencies where displacement currents are nonnegligible.

It is of considerable interest at this stage to compare these numerical results with those computed using Millington's method [3]. His empirical formula for $F'(p_0, V,K)$ in the notation of the present paper would read

$$F'(p_0,V,K)=\left[F(p_0/K)F(p_0)\frac{F[p_0(1-V)]F(p_0V/K)}{F[p_0(1-V)/K]F(p_0V)}\right]^{1/2}. \quad (18)$$

Values computed from this formula for the cases $K=2$ and $K=\infty$ are indicated by ○ and ●, respectively, on figures 2 to 11. The agreement is quite reasonable, and therefore further support is given to the validity of the Millington method, which has been known to predict correctly, within 1 db or so, the attenuation over certain mixed paths. It is believed, however, that differences are not of sufficiently small order to be neglected if fairly precise values of the fields in amplitude and phase are required.

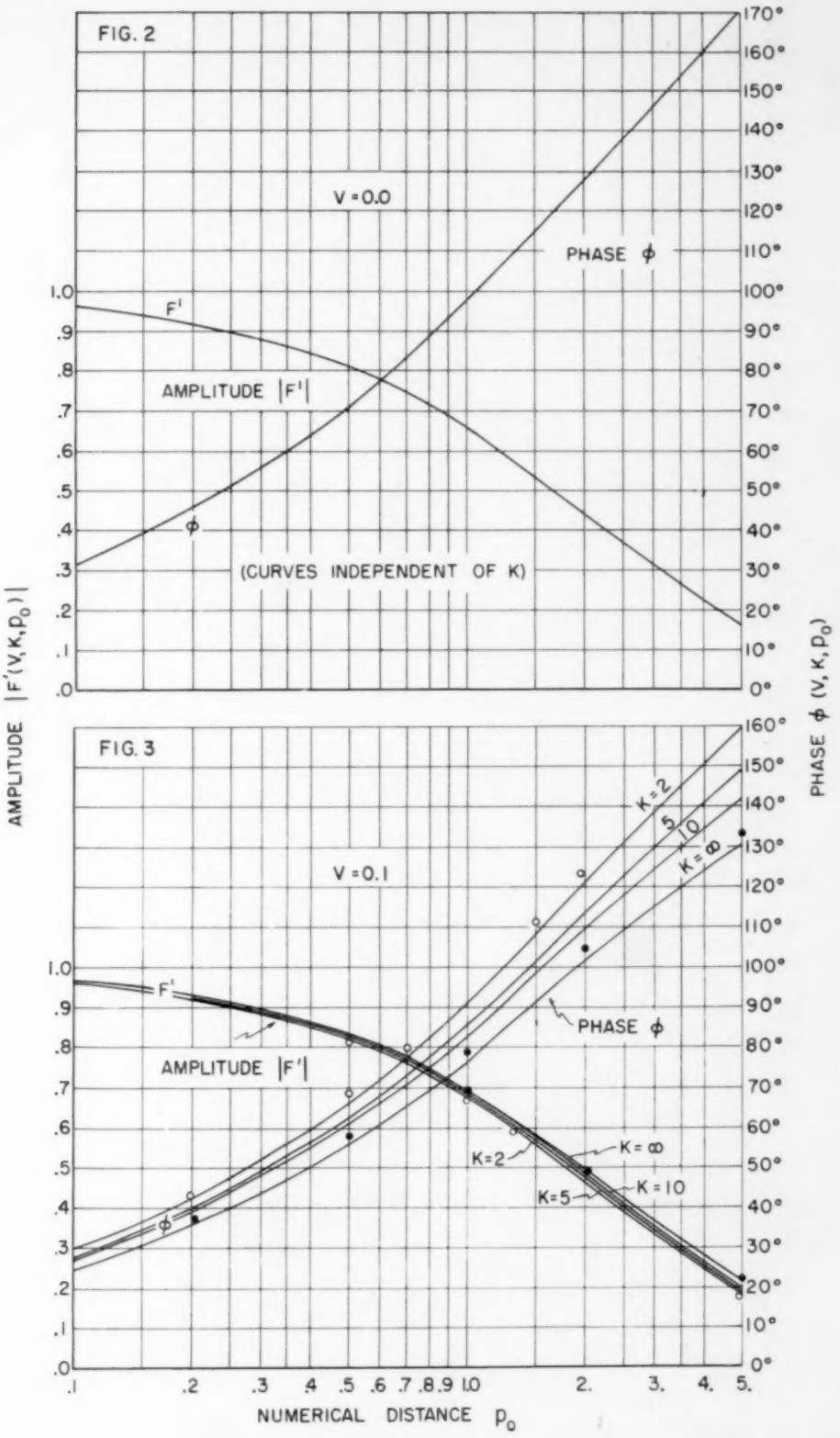

FIGURES 2 AND 3. *Attenuation function $|F'|e^{i\phi'}$ for transmission between A (or B) and B (or A) over a mixed path plotted as a function of the numerical distance p_0.*

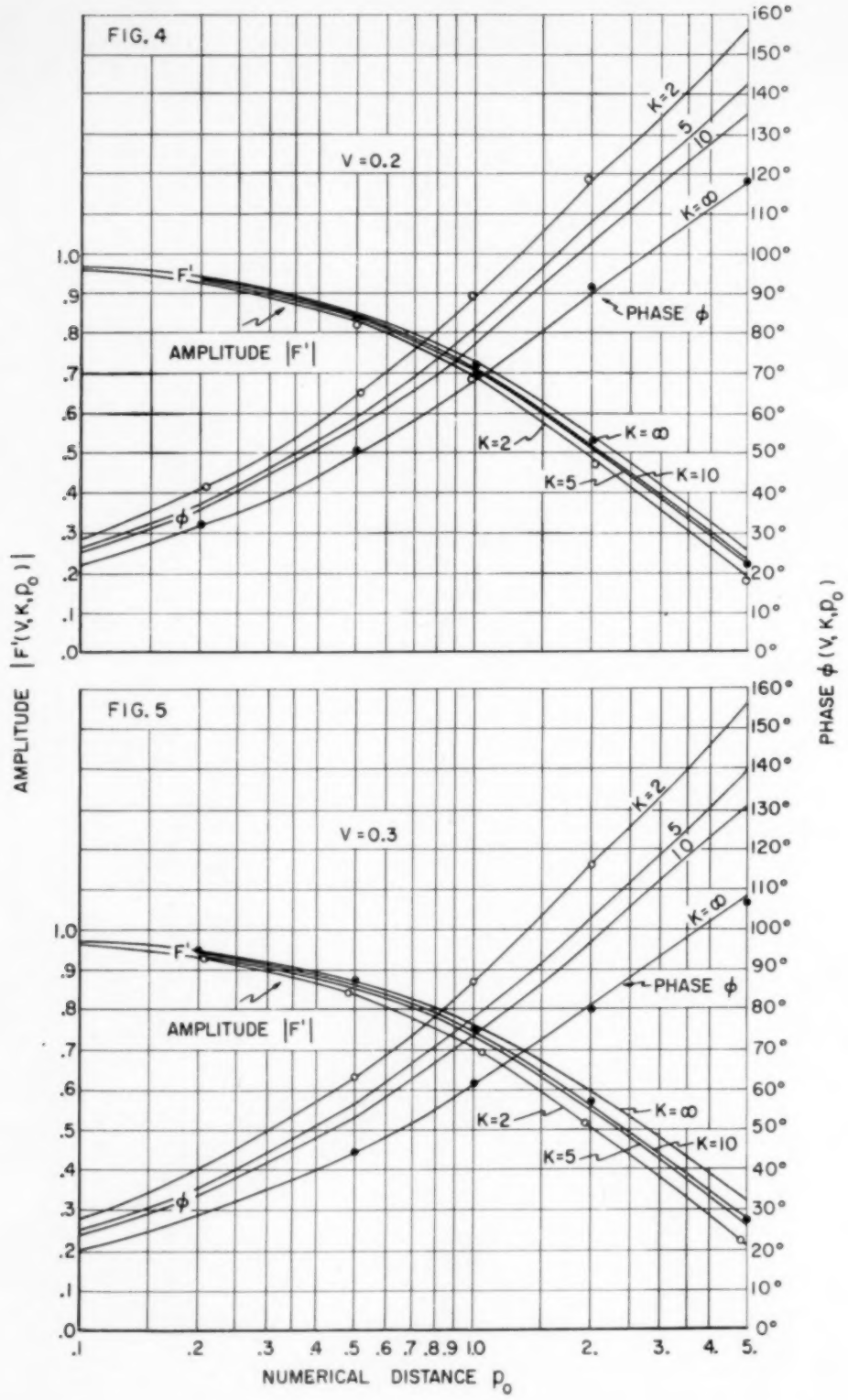

FIGURES 4 AND 5. *Attenuation function $|F'|e^{i\phi'}$ for transmission between A (or B) and B (or A) over a mixed path plotted as a function of the numerical distance p_0.*

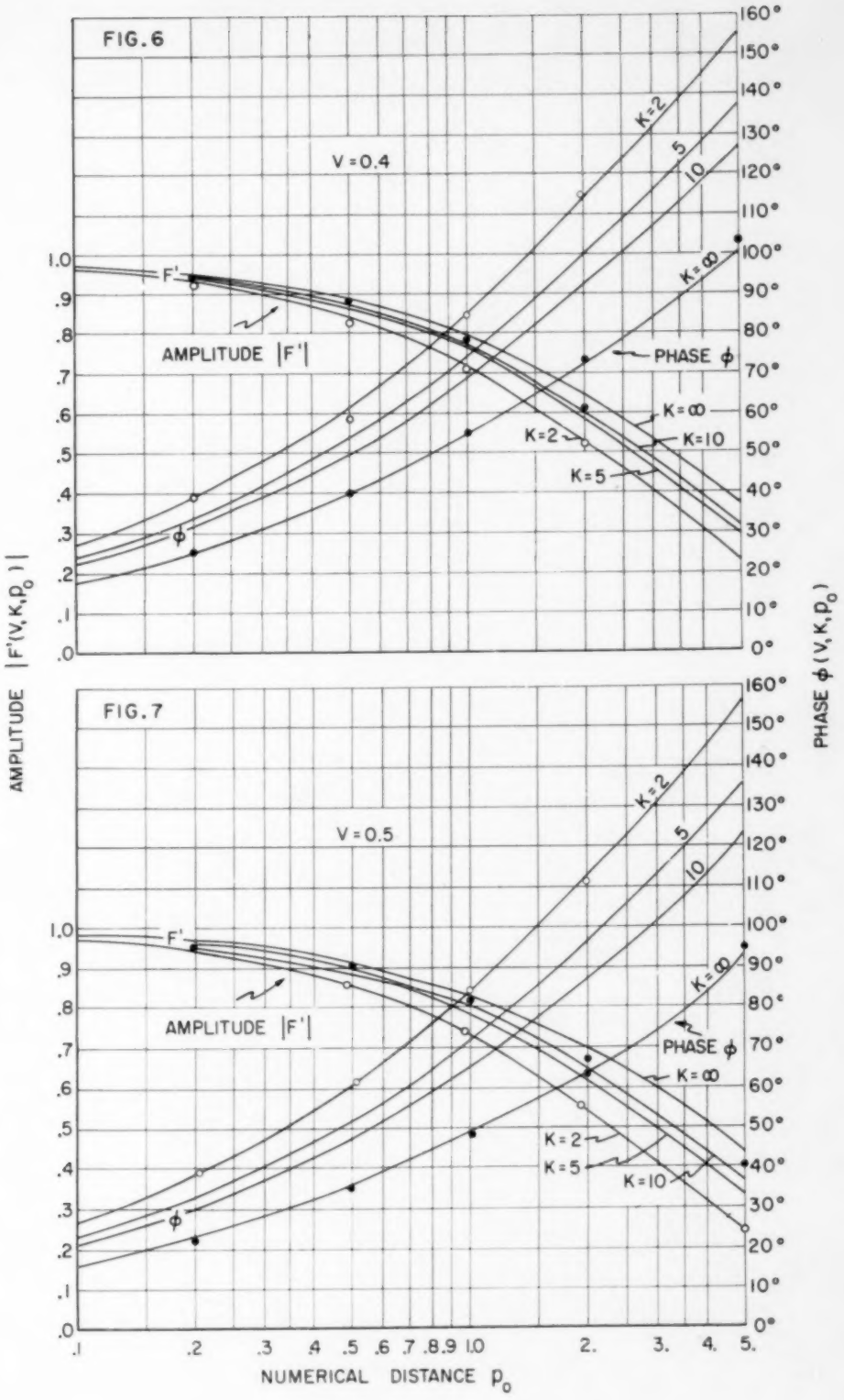

FIGURES 6 AND 7. *Attenuation function $|F'|e^{i\varphi'}$ for transmission between A (or B) and B (or A) over a mixed path plotted as a function of the numerical distance p_0.*

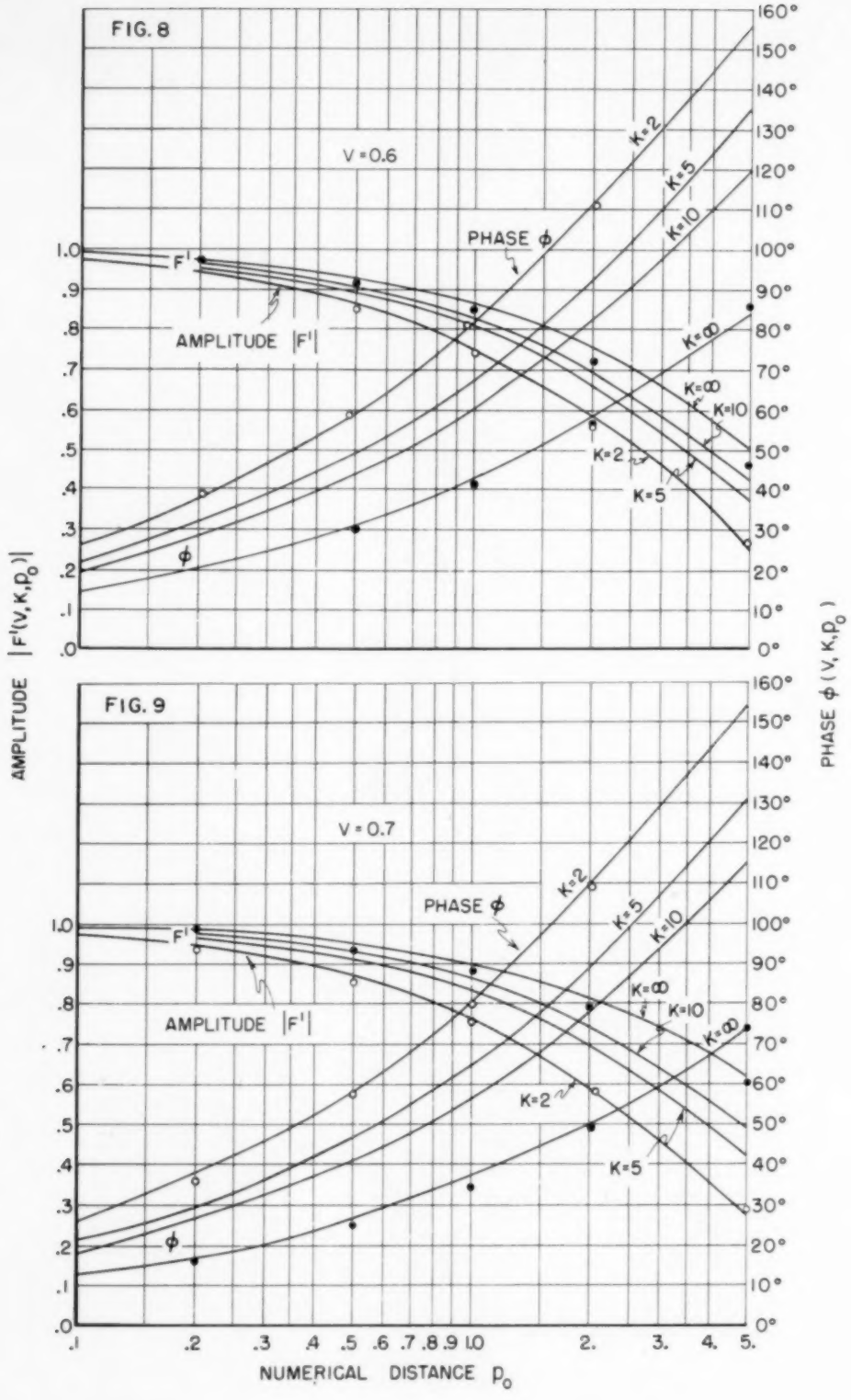

FIGURES 8 AND 9. *Attenuation function $|F'|e^{i\phi'}$ for transmission between A (or B) and B (or A) over a mixed path plotted as a function of the numerical distance p_0.*

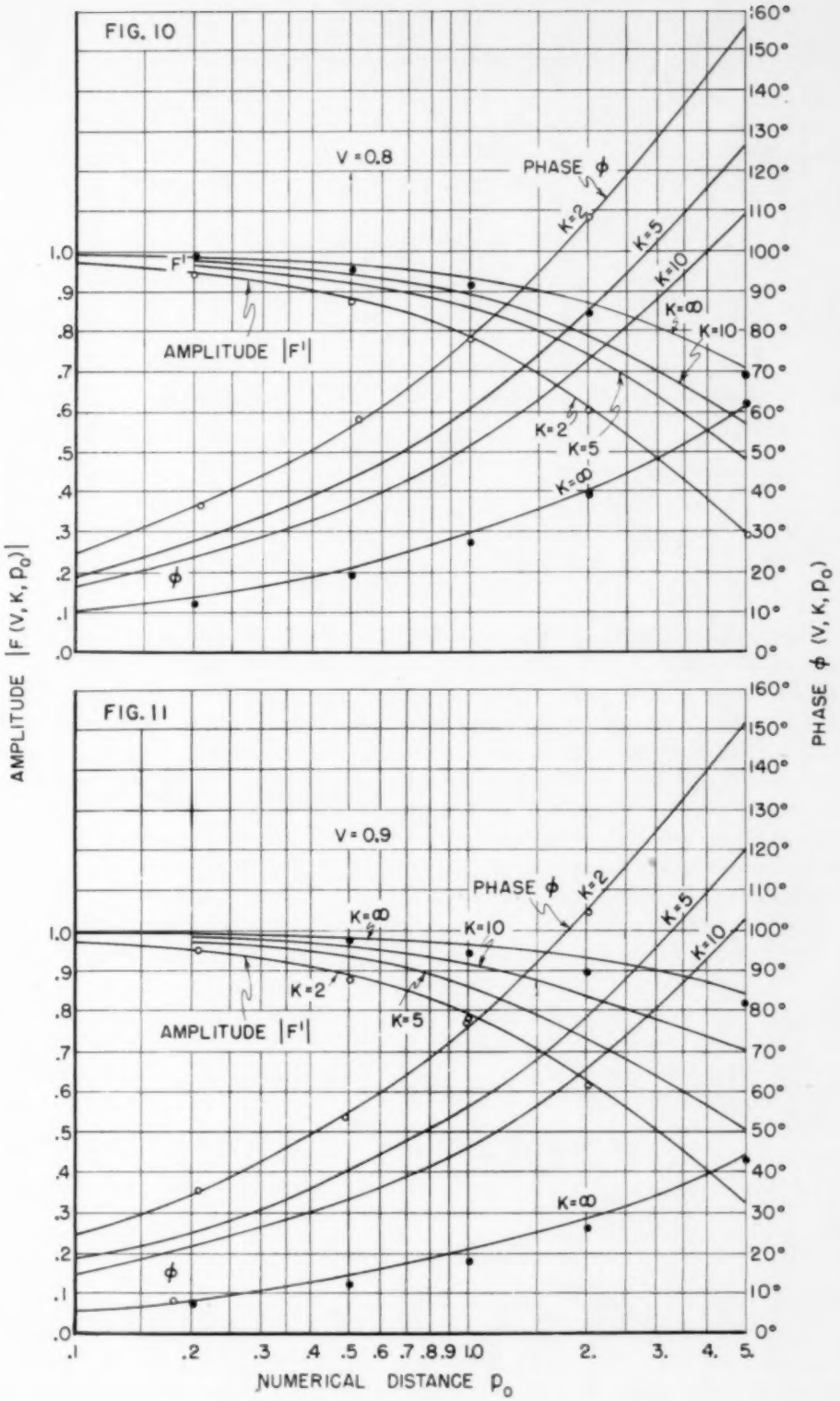

FIGURES 10 AND 11. *Attenuation function $|F'|e^{i\varphi'}$ for transmission between A (or B) and B (or A) over a mixed path plotted as a function of the numerical distance p_0.*

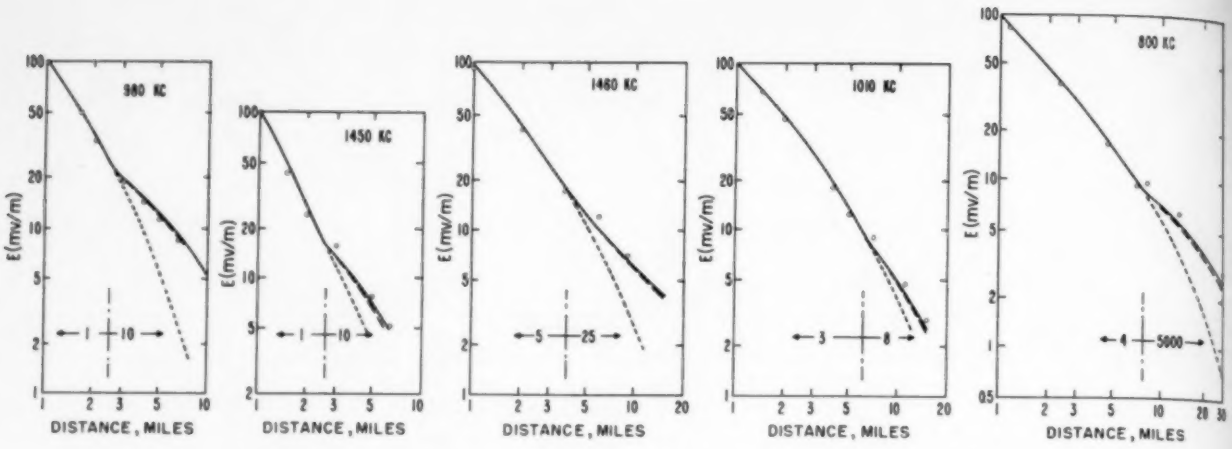

FIGURE 12. *Field strength versus distance curves for various mixed paths.*

The conductivity in millimhos per meter to the left and right of the boundary is shown on each curve. The experimental results were communicated to the author privately by P. A. Field, formerly of the Canadian Broadcasting Corporation. ————, From parametric curves; — —, computed by Millington method; ○,experimental (P. A. Field); - - - - - -, curve, assuming homogeneous ground throughout ($V=K=0$).

4. An Application

To illustrate the application of these parametric curves, the field strength in millivolts per meter is shown plotted in figure 12 as a function of the distance ($=r_0+R_0$) in miles for five different mixed paths. The curves are normalized so that the field strength at 1 mile is 100 mv/m. Experimental values supplied by P. A. Field are also indicated. The curves calculated by the Millington method are also shown in figure 12. The conductivities on the near and far sides of the boundary are indicated on the figures and are expressed in millimhos per meter. The agreement between the computed and experimental results is quite good. For these short distances the curves calculated by the Millington method fell slightly below the curves computed from the integral formula. In view of the uncertainty in the exact physical features of the ground, the difference between the two methods of calculation hardly seems significant for these situations. It is interesting, however, to note that the Millington method in four out of five cases underestimates the recovery effect to a greater degree than the integral method. The dotted curves in figure 12 correspond to the case where the ground is homogeneous throughout, and has the conductivity of the earth on the transmitter side of the boundary. The difference between the solid and dotted curves is a measure of the recovery effect, and it is apparent that the theory indicates a gradual transition at the boundary and does not show any sudden or transient features at the boundary. It would seem from the experimental results that there is actually some type of disturbance at the boundary between the two media which is not predicted by the theory. It is believed that a more rigorous evaluation of the integral equation is necessary to describe the nature of the field near the boundary.

5. The Refraction Effect

Although this problem was formulated for the mutual impedance between antennas A and B on either side of an oblique boundary, the consequent path of stationary phase did not depend on the inclination angle θ. In other words, any refraction effects were neglected. It is the purpose of this section to revise the stationary phase evaluation of the integral to account for the changes of phase velocity between the two media. It is admitted that the procedure is not rigorous and is based on certain physical ideas that have their roots in geometrical optics.

With regard to figure 1, the direct ray AOB between the antennas would represent the path of stationary phase if refraction effects were neglected. Of course, if the boundary was at a

right angle to AOB (i. e., $\theta=90°$), it would be rigorously justified to assume AOB was the path of the stationary phase. It can be expected, however, that for the oblique boundary the path of stationary phase would be along a line APB, where P was displaced along the boundary from O by an amount q. Furthermore, it can be anticipated that q would be small compared to r_0 and R_0. The location of the point P can be best obtained by regarding q as a variable quantity in order to find when the total phase along APB is stationary or when it is a minimum. This is essentially a statement of Fermat's principle in optics. The difference between the phase along the paths AOB and APB are now considered to be due to two factors: (1) the actual increase of path length, and (2) the change of the ratios of the path lengths for the two respective media. For example, if the left-hand medium is more poorly conducting than the right-hand medium (i. e., $K>1$), the phase velocity is relatively less to the left of the boundary, so that AP is less than AO. More explicitly, the total phase Φ over the path APB can be written

$$\Phi(q)=\beta(\hat{r}_0'+\hat{R}_0')+\phi'(\hat{V},K,\hat{p}_0) \tag{19}$$

where

$$\hat{r}=[r_0^2+q^2-2r_0q\cos\theta]^{\frac{1}{2}}$$

$$\hat{R}_0=[R_0^2+q^2+2R_0q\cos\theta]^{\frac{1}{2}}$$

$$\hat{V}=\frac{\hat{R}_0}{\hat{r}_0+\hat{R}_0} \text{ and } \hat{p}_0=-\frac{i\beta(\hat{r}+\hat{R}_0)}{2}\left(\frac{\eta}{120\pi}\right).$$

The function $\phi(\hat{V},K,\hat{p}_0)$ in the above expression is taken to be of the same form as the function $\phi(V,K,p_0)$ previously computed. The general scheme is then to vary q to find where $\Phi(q)$ is stationary. For the present purpose, however, it is convenient to make some further approximations utilizing the fact that q is small. The phase function then becomes

$$\Phi(q)\simeq\beta(r_0+R_0)\left[1+\frac{\sin^2\theta}{2}\left(\frac{q}{d}\right)^2\frac{1}{V(1-V)}\right]+\phi'(\hat{V},K,\hat{p}_0), \tag{20}$$

where

$$\hat{V}\simeq V+\frac{q}{d}\cos\theta, \quad d=r_0+R_0,$$

and

$$\hat{p}_0\simeq p_0\left[1+\frac{\sin^2\theta}{2}\left(\frac{q}{d}\right)^2\frac{1}{V(1-V)}\right]\simeq p_0.$$

The terms containing higher powers in (q/d) have been neglected and, in fact, in the expression for p_0, the term containing $(q/d)^2$ can be also dropped, since $\phi'(V,K,p_0)$ is a relatively slowly varying function of p_0. It is now convenient to express $\phi'(V)$ as a Taylor expansion, as follows:

$$\phi'(\hat{V})=\phi'(V)+\frac{q\cos\theta}{r_0+R_0}\left[\frac{d\phi'(\hat{V})}{d\hat{V}}\right]_{\hat{v}=v}+\left[\frac{q\cos\theta}{r_0+R_0}\right]^2\frac{1}{2}\left[\frac{d^2\phi'(V)}{d\hat{V}^2}\right]_{\hat{v}=v} \tag{21}$$

Because q is small compared to r_0+R_0, only the first term or two of the expansion are significant. The phase function now becomes

$$\Phi(q)\simeq\beta(r_0+R_0)+\phi'(V,K,p_0)-\frac{q\cos\theta}{r_0+R_0}\delta(V)+\frac{\sin^2\theta}{V(1-V)}\pi\frac{d}{\lambda}\left(\frac{q}{d}\right)^2, \tag{22}$$

where $\delta(V)=-d\phi(V)/dV$ is essentially a positive quantity. The right-hand side of the equation is a quadratic in q and has a minimum or stationary value when

$$\frac{q}{d}=\frac{q_0}{d}=\frac{\cos\theta\,\delta(V)\,V(1-V)\lambda}{2\sin^2\theta\,\pi(r_0+R_0)}. \tag{23}$$

This value of q, namely, q_0, which makes $\Phi(q)$ stationary, is then a measure of the deviation of the direction of the phase of the ground wave as it crosses the boundary. The appropriate values of $\delta(V)$ can be obtained directly from the parametric curves of $\phi'(p_0, V, K)$. Actually, it is a little more meaningful to consider the angles δ and δ_1, which are the angles OBP and OAP in figure 1. These can be called bearing errors, as they are a measure of the change of direction of the phase front relative to a direct unimpeded wave between A and B. In terms of q_0, the bearing errors, expressed in degrees, are given by

$$\delta \simeq \frac{q_0}{r_0+R_0} \frac{1}{(1-V)} \sin\theta \frac{180}{\pi}$$

and

$$\delta_1 \simeq \frac{q_0}{r_0+R_0} \frac{1}{V} \sin\theta \frac{180}{\pi}.$$

Employing typical values of the parameters and letting $K=\infty$, values of δ and δ_1 were computed and are:

V	$\frac{\epsilon_0\omega}{\sigma}$	$\frac{r_0+R_0}{\lambda}$	$\theta=45°$		$\theta=60°$	
			δ	δ_1	δ	δ_1
0.2	0.01	50	0.06	0.24	0.03	0.14
.2	.01	100	.03	.14	.02	.08
.2	.001	50	.02	.08	.01	.04
.2	.001	100	.01	.06	.01	.03
.5	.01	50	.10	.10	.06	.06
.5	.01	100	.06	.06	.03	.03
.5	.001	50	.03	.03	.02	.02
.5	.001	100	.02	.02	.01	.01
.8	.01	50	.26	.06	.17	.04
.8	.01	100	.16	.04	.09	.02
.8	.001	50	.08	.02	.05	.01
.8	.001	100	.06	.02	.04	.01

It might seem surprising at first glance that these values are so small. This is as should be expected, however, because the absolute phase velocities of the ground wave over the two media differ only by a fraction of one percent [10]. It is noted that the bearing errors are largest when the antenna is near the boundary, and where the separation between antennas A and B is 50 wavelengths or less. Of course, as the obliqueness of the boundary becomes more noticeable (i. e., $\theta<45°$) the calculated values of δ and δ_1 would be larger. One should be cautious, however, in attempting to apply this method to the case where the boundary makes a small angle with the line AB between the antennas. In such an instance the approximation used in evaluating the basic integral by a stationary phase principle becomes invalid.

6. Conclusion

The results obtained in this paper provide a theoretical check of the Millington semi-empirical method of calculating the amplitude and phase of a wave crossing a boundary separating two media. The parametric curves presented here should be convenient for making predictions for propagation along a two-media path at low and medium frequencies. It is also indicated that the refraction effects for a wave crossing the boundary obliquely are very small.

I record my thanks to Loris Perry, who carried out most of the computations.

7. References

[1] K. Suda, Field-strength calculations—new method for mixed paths, Wireless Engineer **31**, 249 (1954).

[2] H. L. Kirke, Calculations of ground wave field strength over a composite land path, Proc. Inst. Radio Engrs. **37**, 489 (1949).

[3] G. Millington, Ground wave propagation over an inhomogeneous smooth earth, part 1, Proc. Inst. Elec. Engrs. **96**, 53 (1949).

[4] P. C. Clemmow, Radio propagation over a flat earth across a boundary separating two different media, Trans. Roy. Soc. (London) **246**, 1 (1953).

[5] H. Bremmer, The extension of Sommerfeld's formula for the propagation of radio waves over a flat earth to different conductivities of the soil, Physica **20**, 441 (1954).

[6] E. Feinberg, Propagation of radio waves over an actual surface, Izdatel'stbo Akademii Nauk S. S. S. R. (Moscow), 109–131 (1944).

[7] S. Ballantine, Reciprocity in electromagnetic mechanical, acoustical, and interconnected systems, Proc. Inst. Radio Engrs. **17**, 929 (1929).

[8] G. D. Monteath, Application of the compensation theorem to certain radiation and propagation problems, Monograph No. 3, Proc. Inst. Elec. Engrs. **98**, 1 (1951).

[9] K. A. Norton, Calculation of the ground wave field intensity, Proc. Inst. Radio Engrs. **29**, 623 (1941).

[10] J. R. Wait and L. L. Campbell, Transmission curves for ground wave propagation at low radio frequencies, Report R. 1, Defence Research Telecommunications Establishment, Ottawa, Canada (1952). (Extensive amplitude and phase data are given in this report for frequencies from 15 to 500 kc for a wide range of conductivities and dielectric constants.)

BOULDER, December 7, 1955.

Journal of Research of the National Bureau of Standards Vol. 57, No. 1, July 1956 Research Paper 2688

Effect of Object Frequency on Focal Position of Four Photographic Objectives

Fred W. Rosberry

Three wide-angle aerial-camera lenses of 6-inch nominal focal length and one smaller lens of 32-millimeter focal length were given photographic resolving-power tests. Targets were of the parallel line type with several groups of three lines representing a wide range of lines-per-millimeter values. The image plane of best focus was visually located, and exposures were made at four different positions inside of this focus and the same number outside. Measurement of the resultant negatives by a recording microdensitometer revealed the image contrast of the various line-space frequency groups at the nine focal positions. Curves are presented showing the focal positions of maximum image contrast for four values of line-space frequency.

1. Introduction

During the past decade, there has been considerable interest in the effect of target contrast on image contrast and resolving power in the image plane. Investigation of the relationships between these quantities has shown the existence of a number of associated phenomena, among which is a shift in the plane of best focus with target pattern frequency. Any appreciable shift will affect the selection of the proper focal plane in a fixed-focus camera, such as an aerial camera [1, 2].[1] The Optical Instruments laboratory has therefore made an investigation of this phenomenon.

Of the lenses on hand at the time this investigation was being planned, three, representing a good, medium, and fair quality as shown by previous resolving power tests, were chosen for testing. They were all wide-angle aerial camera lenses of nominally 6-in. focal length, made by the same manufacturer. A fourth lens was later included representing a different type and of only 32-mm (1.3-in.) focal length.

2. Apparatus and Procedure

To measure the contrast rendition, or contrast in the image plane of a lens, by a photographic procedure, extreme care had to be taken to control the other factors that can affect contrast. Some of these factors are exposure, development, and variation in emulsion from one photographic plate to another. Uniform exposure was maintained by the use of an automatic timing device, with relatively long exposure times such as 2 or 3 sec instead of small fractions of a second as obtained by shutters. Development was maintained uniform by putting as many different exposures as possible on one plate and by agitation during development. The variation in characteristics between plates out of the same box is very small, but this was further reduced by cutting large plates into smaller ones, thus making two or more from one.

[1] Figures in brackets indicate the literature references at the end of this paper.

The targets used in this investigation were the 75-line step contrast and the 200-line step contrast targets, which are variations of those previously reported [3]. The 75-line target consists of 25 groups of 3-line patterns. The line widths and spacings in a given pattern are equal; however, the values vary from one pattern to the next by a ratio equal to $\sqrt[6]{2}$. The range of resolving power for this master target is therefore from 0.2 to 3.2 lines/mm. The range of the 200-line target is from 0.2 to 2 lines/mm, which means that the actual widths of lines and spaces vary from 2.5 to 0.25 mm. This range is covered in a continuously varying linear manner with 200 lines and 200 spaces contained in a distance of 180 mm. The zero line is 20 mm from the origin, so that the over-all length of the resolving-power portion of the chart is 200 mm (fig. 1). The length of the lines is 185 mm, thus giving the contrast scale approximately the same length as the frequency scale. Along the length of the lines the targets are divided into nine areas of different line-space contrast values. The 75-line target had a contrast range in these nine areas from 0.22 to a high of 3.19 on the density scale. The same nine areas on the 200-line target had a range from 0.10 to 1.51.

Although two targets were used in this investigation, they were not used simultaneously. The target under observation was mounted on the axis and in front of the lens being tested. As the targets are transparencies, it was necessary for them to be uniformly illuminated from behind. This was accomplished by using a light box of such design that only diffusely reflected light, which was quite uniform and free of hot spots, fell upon the target.

The camera used for exposing the test plates consists of two major components, namely, the lens mount and the camera back (fig. 2). A set of ways similar to a lathe bed supports both components, each mounted on its own carrier or saddle, thus allowing for the necessary movement of one with respect to the other by means of a lead screw. This movement is necessary to accommodate lenses of different focal lengths. The camera back itself is provided with three micrometer screws, by means

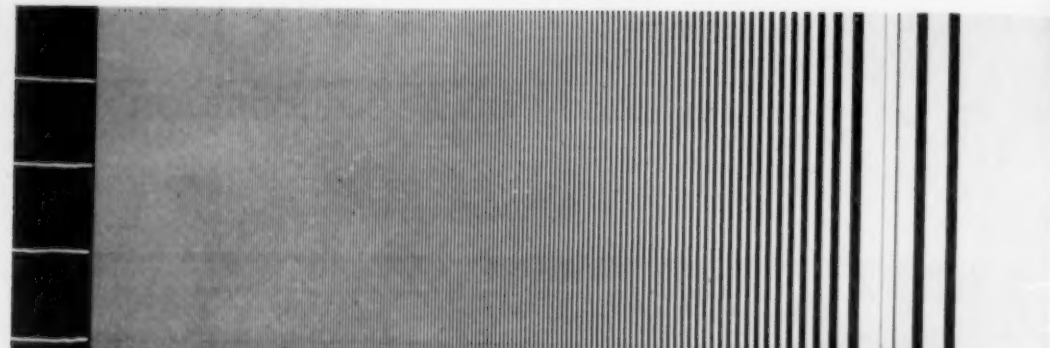

FIGURE 1. *The 200-line step contrast target as used in this investigation.*
The 75-line target was similar except for the 3-line grouping of the lines in the pattern.

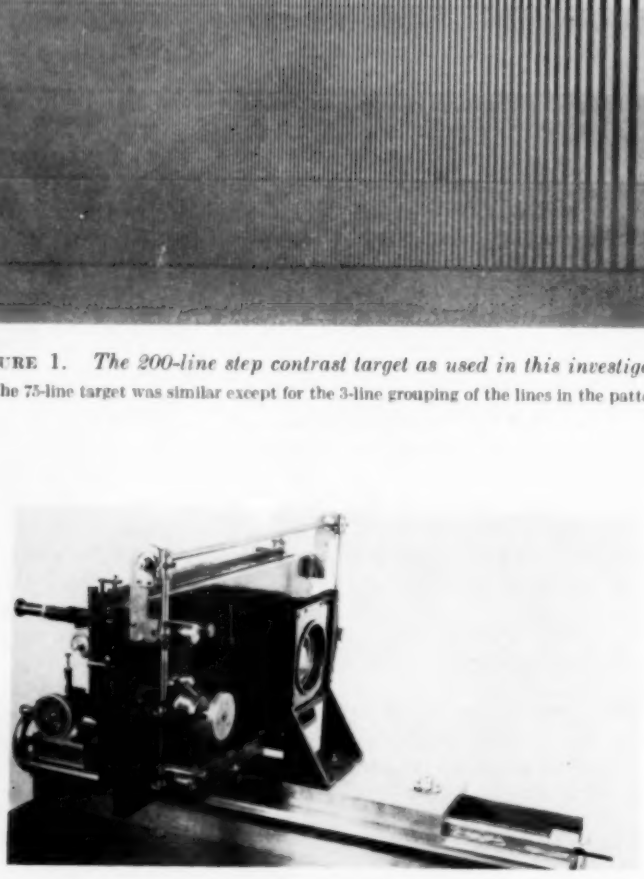

FIGURE 2. *Bench showing lens, plate carrier, and focusing microscope.*

of which small precisely measured axial displacements of a millimeter or less may be made. The plate holder can also be moved vertically in a plane perpendicular to the lens axis, allowing successive images to be taken on a single plate, one above the other. Changes in the focal position of amounts as small as 0.2 mm are easily accomplished with the micrometer adjustment. A microscope is mounted on the same saddle as the camera back and focused on the plane of the emulsion.

The lens mount supports the lens rigidly in place and carries the necessary bellows and light shields to protect the negative from stray light. The mount is constructed so that it holds a metal lens board measuring 6 in. square, which in turn carries the lens under test.

The distance between lens and target was equal to 26 focal lengths of the lens under test. With this lens-to-target spacing the image distance is a little longer than for an infinitely distant target, but it is believed that there is very little change in the resolving power characteristics. Theoretical considerations indicate that the lens-to-target distance can be reduced to as low as 15 focal lengths without significant change in the resolution characteristics from those for infinitely distant objects.[2]

With the lens-target distance set at 26 focal lengths for the 6-in. lenses, the effective spacing of lines in the target on the image plane was 5.0 to 79.6 lines/mm for the 75-line target. With the 32-mm lens, the lens-to-target distance was 51 focal lengths, giving a range of 10 to 100 lines/mm for the 200-line target. Focusing was accomplished by properly spacing the camera-back and the lens until a well defined image appeared on a ground glass, which was in the position the photographic plate would occupy during photographing. The microscope was then focused on the plane of the ground glass and locked in that position. With the ground glass removed, it was then possible to view the image directly and make any small focusing adjustments necessary. The micrometer was then set so that the plate carrier was 0.8 mm inside of the best visual focus, and a panchromatic photographic plate set in the carrier. Using the vertical ways of the camera back, the plate was racked to its uppermost position and the first exposure made. The plate was then moved away from the lens by 0.2 mm and lowered enough to allow the image to be put above the first and another exposure made. This procedure was repeated until nine exposures were made, covering the range from 0.8 mm inside to 0.8 mm outside of the visually estimated focus. After developing in Dk-60a for 5 min and fixing, this plate was then ready for measurement.

The density of each line and space for three of the target contrast levels were the quantities to be measured. These were determined by using a recording microdensitometer. The test negative was located on the plate carrier of the instrument, properly oriented, and brought into good focus. One contrast area of one focal position of the test negative was then scanned and the local values of line and space density were automatically recorded in the form of a graph. The negative was then relocated so that the same contrast area on the next adjacent image, representing the next focal position, was then ready for scanning. The instrument was refocused at each change in negative position. All focal positions were covered by this procedure, and this constituted a run. Other runs were made for the two remaining contrast areas to be measured. Each run was repeated two more times with the results averaged to minimize any variation in measurement that still might exist, thus making three runs of the three contrast areas, with each run covering the nine focal positions.

3. Results of Measurement

The graph produced by the microdensitometer consisted of curves on a strip of chart paper graduated with a logarithmic scale of photographic density whose limits were zero and infinity. The quantity measured was the amount of light transmitted by a very small area of the test negative. Because of the line and space characteristic of the negative being scanned, the recording pen was traveling from near one end of the scale to near the other, thus indicating the highest transmission or minimum density at a space and the maximum density at a line. These data were tabulated by reading, on the log scale, the maximum and minimum for each cycle. The difference of the two was called contrast (C). The 75-line target, which was divided into 25 groups of 3 lines and had the line frequency constant for each group, was averaged to determine the maximums and minimums for each group. A graphical representation of these data is shown in figures 3 and 4. The curves are grouped according to the particular lens under investigation and the target contrast. Each curve represents the amount of contrast in the image at various focal positions for a specified image frequency. Some of the curves show a bar indicating the calculated depth of focus for the adjacent frequency or resolving power. The depths of focus herein referred to were calculated from the formula $d=4b/a$, where d is the depth of focus in millimeters, b is the f-number, and a is the resolving power in lines per millimeter, for which the depth of focus is sought [3]. This formula was developed for use with high-contrast targets, which should be taken into account when viewing the results. Theoretically the curve should reach zero value of image contrast at about the same points as indicated by the ends of the depth-of-focus line. The range of the depth of focus is shown only for the two curves of highest frequency, as the range of focal positions is not great enough to include the depth-of-focus range at the lower frequencies.

[2] Private communication from D. P. Feder.

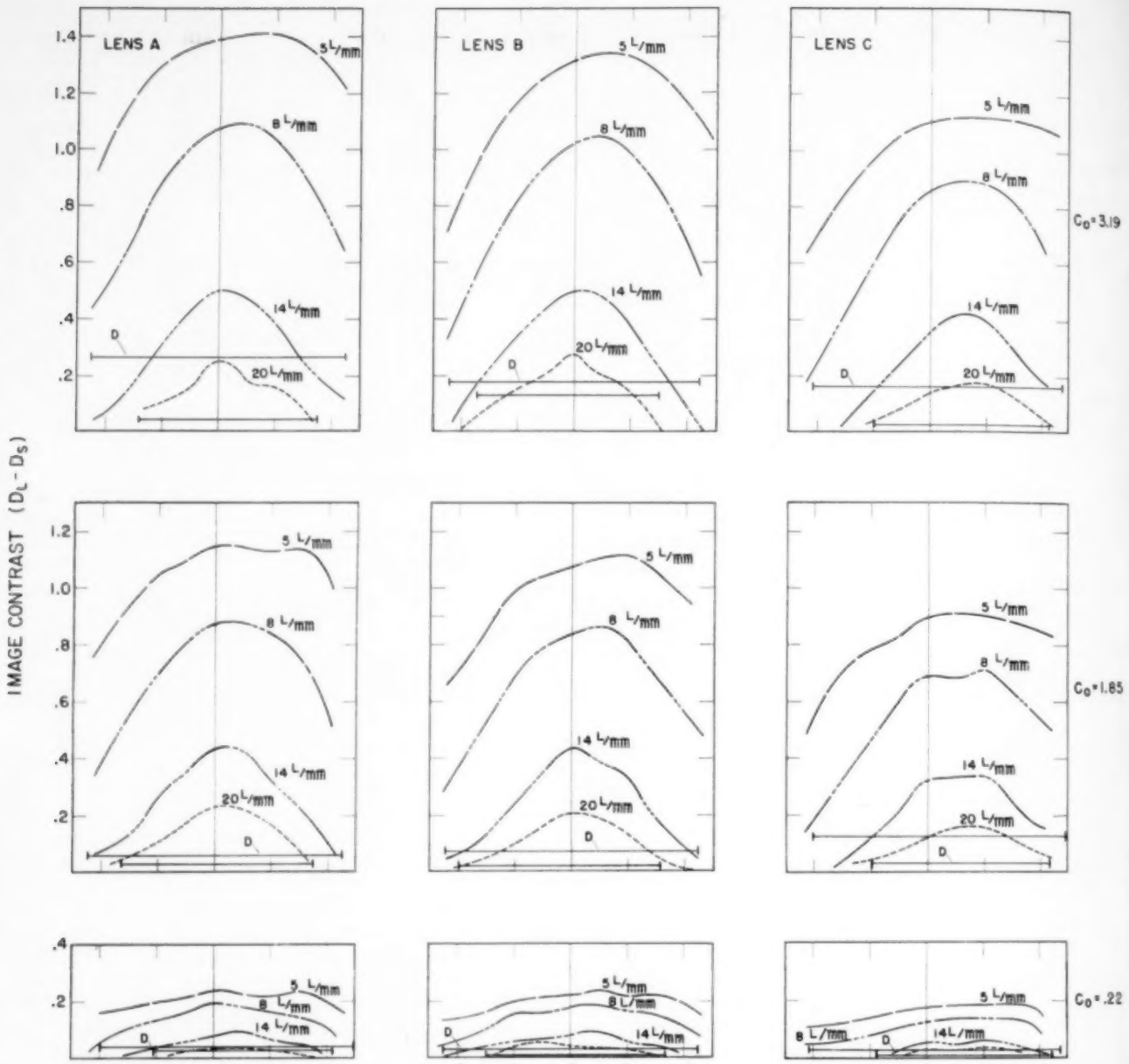

FIGURE 3. *Curves showing the contrast in the image at various focal positions of four line-frequency patterns at three values of target contrast for the three wide-angle aerial camera lenses.*

L/mm, lines per millimeter; D_L, photographic density of line; D_s, photographic density of space. The lines marked "*D*" indicate the range of the calculated depth of focus.

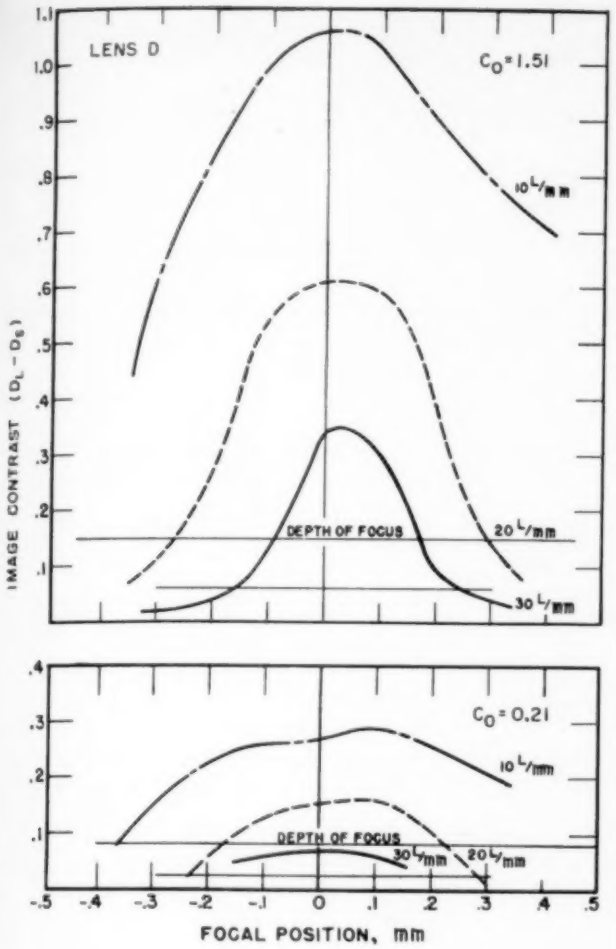

FIGURE 4. *Contrast-focal position curves for 32-mm lenses.*
These curves are similar to those of figure 3 for 6-in. lenses.

4. Discussion

Contrast can be expressed as the difference between two densities (ΔD), or it can be expressed as a ratio of the two transmissions T_1/T_2. Both methods are in use, with perhaps the former more common. Some of the curves were plotted by both methods, and although each illustrated the point well, the ΔD procedure lent itself better to data from the microdensitometer. One point rather clearly shown by these curves is the relatively small amount of shift in the optimum focus for the four frequencies plotted. This of course is a quality that will change from one lens to another and is somewhat dependent on the individual lens aberrations.

The three wide-angle aerial camera lenses were given resolution tests prior to this investigation, and the results of these tests established that their resolution characteristics were within the range covered by the average lens of this type. Distortion measurements also indicate that the sample lenses are not outside the average. The lenses tested herein are

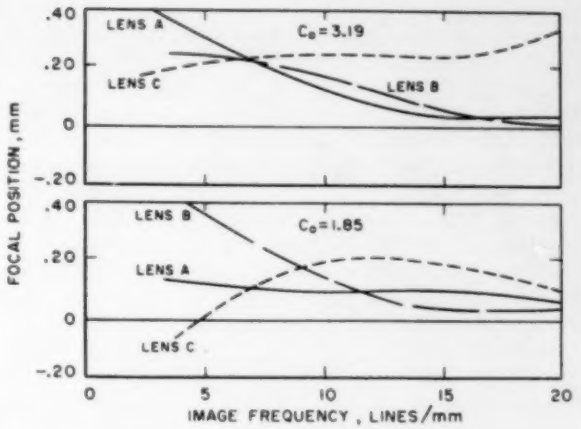

FIGURE 5. *Curves showing the shift from an arbitrary zero of the focal position giving highest contrast for various line frequencies at two target-contrast levels.*
The same three lenses are shown in figure 4.

quite consistent in showing very little shift of focus at the two higher target contrasts; at the low target or object contrast (C_o=0.22) the shift is even less noticeable. The sets of curves shown in figure 5 summarize the findings for the three 6-in. wide-angle lenses. The amount of shift (from an arbitrary zero) of the focal position giving highest contrast is plotted for four values of image frequency. The two plots represent the results obtained with two different target contrasts. The focal position measured along the ordinate of the graph was determined from the crest of the corresponding contrast curve shown in figure 3. The contrast curves for the lower frequencies are rather flat-topped, which makes precise location of the peaks difficult. Shifting of the plane of best focus with object frequency as indicated herein is very small for lenses of near average quality.

As focal settings become more precise, the position of best focus becomes more difficult to locate. A zone is found within which a position of best resolution and another position of highest contrast rendition are located. This effect is present at all points in the field and, as the range of this zone of best focus is less than the inherent field curvature of a lens, critical focusing over the entire field becomes extremely difficult. The residual spherical aberration in the lens is probably a cause of this focal shift. The position for maximum contrast of broad lines is where the circle of confusion is the smallest and not necessarily where the resolution is best.

The present work accordingly confirms the results of earlier workers [1, 2, 5] that a difference in focal setting exists between the settings for best resolution and for best contrast rendition. However, it emphasizes the fact that this difference is usually so small that it is seldom advantageous to set for the position of maximum contrast rendition for low-frequency patterns as opposed to setting for the position of maximum resolution. For example, in some earlier work [1, 2], the difference in focal setting

for frequencies in the image of 4.1 and 20.6 lines/mm was indicated to be as high as 0.03 in., or 0.76 mm. It was further indicated that the improvement in contrast rendition would be quite appreciable at the lower frequencies in setting at the optimum image contrast for those frequencies with marked loss at the higher frequencies. It is clear from the results shown in this paper for the three lenses, shown in figure 3, that the shift in focal settings between frequencies of 5 and 20 lines/mm is at most 0.20 mm. Moreover, the slight gain in contrast rendition by setting at the maximum for the low frequency is not sufficient to warrant accepting the appreciable loss in contrast rendition at the higher frequencies. It is probable that some few lenses of a given type show focal shifts as high as 0.76 mm, but it seems likely that such lenses are the exception rather than the rule.

The author expresses appreciation for the interest and advice rendered by Francis E. Washer and Robert E. Stephens.

5. References

[1] Duncan E. MacDonald, Photogrammetric Eng. **17,** 383 (1951).
[2] Robert N. Colwell, Photogrammetric Eng. **20,** 433 (1954).
[3] Francis E. Washer and Fred W. Rosberry, J. Opt. Soc. Am. **41,** 597 (1951).
[4] Francis E. Washer, J. Research NBS **34,** 187 (1945) RP1636.
[5] R. N. Hotchkiss, F. E. Washer, and F. W. Rosberry, J. Opt. Soc. Am. **41,** 600 (1951).

Washington, November 20, 1955.

Journal of Research of the National Bureau of Standards Vol. 57, No. 1, July 1956 Research Paper 2689

An Examination of the 1955 Helium Vapor-Pressure Scales of Temperature

E. Ambler and R. P. Hudson

In a previous communication, magnetic thermometer calibrations in the region 1.3° to 4.2° K were used to examine the internal consistency of two provisional helium vapor-pressure scales of temperature. Since that article went to press, these scales have been made available in their final form, and further measurements have also been made. The results of all the measurements, seven runs in all and with two different apparatuses, are used here to examine the latter scales. The results of six runs were self-consistent and could be reconciled with the empirical scale of Clement et al. (T_{55E}) to within 2 millidegrees, and with the calculated scale of Van Dijk and Durieux (T_{55}) to within 5 millidegrees. The remaining run showed better agreement with T_{55}. It appears, therefore, that the previous assessment of the T_{55} scale may have been a little too favorable. The most critical interpretation of the findings is that the present technique of vapor-pressure measurement is not sufficiently precise to discriminate between the two scales.

1. Introduction

In a recent publication [1][1] the authors examined the internal consistency of two vapor pressure-absolute temperature (p-T) relations through the calibration of a magnetic thermometer in the range 1.3° to 4.2° K. One such relation was that of Clement, Logan, and Gaffney [2], based upon an empirical equation, and the other a thermodynamic calculation by Van Dijk and Durieux [3].

After reference [1] had been prepared for publication both the new p-T relations were modified by their respective authors. Clement based his final temperature scale [4] (to be referred to by T_{55E}) on the experimental data of several authors, including Ambler and Hudson, obtained in one of two ways, viz, a measurement of the vapor pressure using (a) a separate vapor-pressure bulb, or (b) the pressure over the liquid helium bath plus an appropriate correction for the "hydrostatic head," when a heat source was employed to maintain a constant flow of bubbles up through the liquid. Van Dijk [5] has increased his temperature values slightly in the region 3.3° to 4.3° K so that his p-T curve is tangent to a curve through the gas-thermometer data of Berman and Swenson [6] near the normal boiling point. Temperatures derived from this new scale will be denoted by T_{55}.

Concurrent with this work, the present authors carried out further measurements, employing the "second apparatus" of [1] to augment the meager amount of data obtained therewith. This was especially important as these same data were not in very close accord with those obtained with the "first apparatus."

The present paper deals with an examination for internal consistency of the T_{55} and T_{55E} tabulation, based upon all of the magnetic thermometer calibrations referred to above.

2. Experimental Procedure

The apparatus has been described in detail in [1] (see fig. 1, b, and text therein). The only modification in procedure was the employment of a manostat [2] to control the temperature of the bath. This proved very useful in that the system came to equilibrium twice as fast as previously and enabled one to obtain twice as many points per run. (It may be of interest to record that at the lowest temperature employed (1.3° K), where the magnetic thermometer is extremely sensitive, the bridge reading remained constant to within the equivalent of 10^{-5} deg for periods in excess of 5 min.)

3. Results

The data obtained in the new series of measurements are summarized in table 1. The pressures, p, have been corrected to 20° C and standard gravity, and the bridge readings, n, have been corrected for nonlinearity in the mutual-inductance decades.

The data of table 1 and those of table 1 in [1] will now be discussed in relation to T_{55} and T_{55E}.

[1] Figures in brackets indicate the literature references at the end of this paper.

[2] The authors are indebted to L. D. Roberts of the Oak Ridge National Laboratory for a drawing of this device. The original design is due to H. S. Sommers, Los Alamos, Rev. Sci. Instr. **25**, 793 (1954).

TABLE 1. *Corresponding values of pressure in millimeters of mercury, p (corrected to 20° C and standard gravity) and bridge dial setting, n (corrected for nonlinearity in decade scale)*

January 4, 1956				January 18, 1956					
p	n	p	n	p	n	p	n	p	n
751.42	17.6077	124.33	20.5650	740.46	17.7534	40.395	22.8654	13.398	25.1098
717.24	17.6786	97.26	21.0243	670.52	17.8968	37.766	23.0118	9.016	25.9244
716.63	17.6797	37.994	22.8817	583.62	18.1039	32.392	23.3234	5.963	26.7913
628.73	17.8697	31.771	23.2392	489.08	18.3710	32.418	23.3208	4.017	27.6320
506.19	18.1953	24.846	23.7329	360.65	18.8495	24.012	23.9254	4.031	27.6271
357.75	18.7391	14.945	24.7613	197.36	19.8600	24.115	23.5168	2.984	28.2729
241.05	19.3912	8.123	26.0191	101.97	21.0572	18.124	24.4938	1.633	29.6006

3.1. Comparison With T_{55} Temperature Scale

The data were analyzed according to the procedure outlined in [1]. When the constants A and B in the formula

$$n-B=A/T \qquad (1)$$

nave been determined, a value of temperature, "magnetic temperature," T_m, is at once calculable for a given value of n. The corresponding value of p leads to T_{55} from the p-T table and $\Delta T=T_{55}-T_m$ may be plotted as a function of absolute temperature. This is done in figure 1. The values of A and B used for each run are summarized in table 2.

TABLE 2. *Values of constants A and B in equation 1 for T_{55} evaluation*

Date	A	B
June 7, 1955	−34.0565	19.2841
June 8, 1955	−34.0085	19.2644
June 16, 1955	−34.0553	19.2896
June 17, 1955	−34.0404	19.2809
August 17, 1955	23.5765	11.3537
January 4, 1956	23.6073	11.9922
January 18, 1956	23.6069	12.1151

It is evident that only the results of August 17, 1955—the first run with the second apparatus—can be brought into very close accord with the T_{55} tabulation. The rest of the data can, however, be brought into very close harmony with each other by suitable choices for A and B in each case, and the entire group deviates considerably from the zero line with a maximum of +4.5 millidegrees at 3.6° K. There appears, furthermore, to be a discontinuity in the region of the lambda-point. (As described in detail in [1], the choice of A and B is made so as to give an optimum fit throughout the entire range of measurement. The implicit assumption is that the T_{55} scale is nowhere in error by a large amount.)

3.2. Comparison With T_{55E} Temperature Scale

Figure 2 was obtained by a procedure analogous to that leading to figure 1, now using T_{55E} instead of T_{55}. Small changes in the values of A and B were necessary as may be seen by consulting table 3 and comparing with table 2.[3] With this temperature scale it is possible to restrict the value of ΔT within the limits of ±2 millidegrees. The discontinuity at the lambda-point is still evident. (Although such a discontinuity is more likely due to faults in the measuring technique than genuinely anomalous behavior of the p-T curve, it has been observed by other investigators. See, for example, Erickson and Roberts [7].)

TABLE 3. *Values of constants A and B in equation 1 for T_{55E} evaluation*

Date	A	B
June 7, 1955	−34.1649	19.3138
June 8, 1955	−34.1461	19.3027
June 16, 1955	−34.1703	19.3167
June 17, 1955	−34.1555	19.3100
August 17, 1955	23.6639	11.3273
January 4, 1956	23.6935	11.9680
January 18, 1956	23.6962	12.0917

4. Discussion

In [1] reasons were given for reposing more trust in the results obtained with the second apparatus (August 1955 data) than in those for the first apparatus (June 1955). These were based upon the attempted improvement in design and the fact that a (rather rough) measurement of the bath pressure plus the hydrostatic-head correction agreed with p measured in the bulb system, within the limits of error of measurement. It can be seen, however, that the measurements of January 1956 reproduce the earlier results obtained with a different apparatus, and fail to agree with the first measurements, using the same apparatus. At the same time, the quality of the second apparatus, as determined by the above-mentioned criteria, had not changed. We have been unable to find a plausible explanation for the discrepancies, which must therefore be held to indicate the degree of trustworthiness for the entire series of experiments. Hence, while the present results viewed as a whole favor T_{55E} to the disadvantage of T_{55}, it is probably correct to conclude that the presently used techniques of vapor-pressure measurement are

[3] It may be noticed, further, that in all cases the constant A decreased slightly on the second day of a 2-day series. This effect, though very small, seems to be real.

not sufficiently precise to resolve the discrepancy between the two scales. This latter is illustrated in figure 3 where we have plotted $T_{55E} - T_{55}$ as a function of T.

In conclusion, it should perhaps be emphasized that although use was made of the results in [1] in the development of T_{55E}, no greater weight was accorded them than any other of four additional independent investigations over the same temperature range. This accounts for the systematic deviation in the regions 1.3° to 2.2°K and 3.6° to 4.2°K, visible in figure 2.

5. References and Notes

[1] E. Ambler and R. P. Hudson, J. Research NBS **56,** 99 (1956) RP2654.
[2] J. R. Clement, J. K. Logan, and J. Gaffney, Phys. Rev. **100,** 743 (1955).
[3] H. Van Dijk and M. Durieux, Proc. Conf. de Phys. des Basses Temperatures, Paris 1955; Commun. No. 145, p. 595.
[4] J. R. Clement (unpublished). This scale is the one referred to in the "note added in proof" to reference 2.
[5] H. Van Dijk (private communication). It is understood that copies of this scale are available on request to the Kamerlingh Onnes Laboratory.
[6] R. Berman and C. A. Swenson, Phys. Rev. **95,** 311 (1954).
[7] R. A. Erickson and L. D. Roberts, Phys. Rev. **93,** 957 (1954).

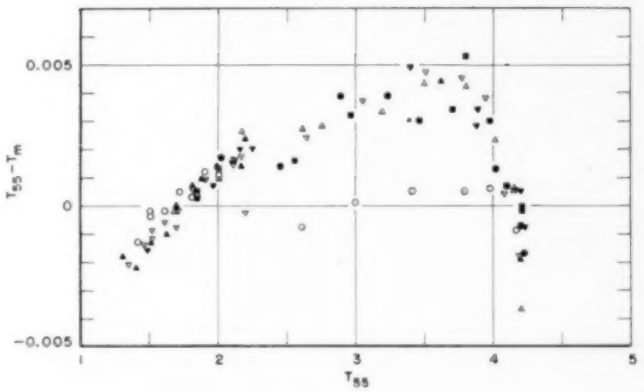

FIGURE 1. *Deviation of T_{55} (from vapor pressure) from T_m (from bridge reading) as a function of T.*

Apparatus I: ●June 7, 1955; ▲June 8, 1955; ■June 16, 1955; ▼June 17, 1955.
Apparatus II: ○August 17, 1955; △January 4, 1956; ▽January 18, 1956.

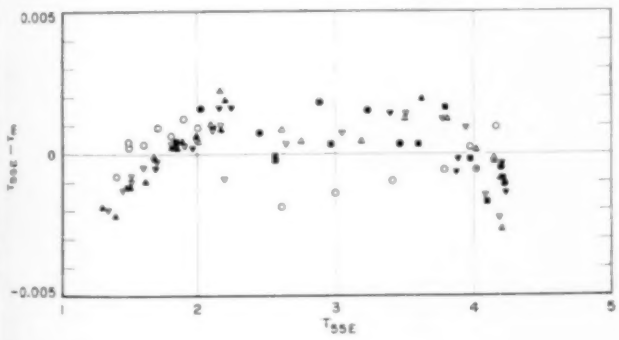

FIGURE 2. *Deviation of T_{55E} from T_m as a function of T.*
For symbol code, see caption to figure 1.

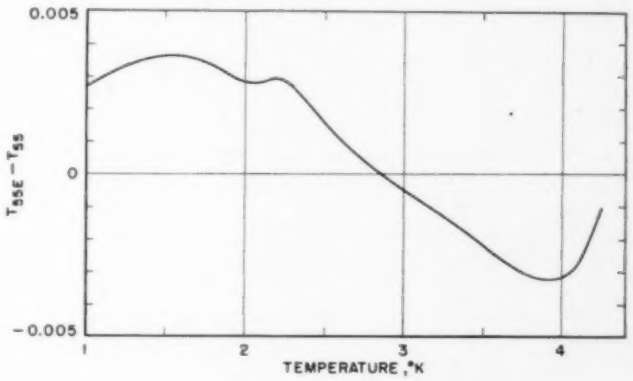

FIGURE 3. *Deviation of T_{55E} from T_{55} as a function of T.*

WASHINGTON, April 10, 1956.

Journal of Research of the National Bureau of Standards Vol. 57, No. 1, July 1956 Research Paper 2690

Heats of Formation of Xonotlite, Hillebrandite, and Foshagite

Edwin S. Newman

The heats of solution of synthetic xonotlite, $5CaO \cdot 5SiO_2 \cdot H_2O$, hillebrandite, $2CaO \cdot SiO_2 \cdot H_2O$, and a sample of naturally occurring foshagite, $5CaO \cdot 3SiO_2 \cdot 3H_2O$, were determined in a mixture of nitric and hydrofluoric acids, and their heats of formation from the oxides were calculated to be −92.6, −34.7, and −94.6 kilocalories per mole, respectively.

1. Introduction

The system CaO-SiO_2-Al_2O_3-Fe_2O_3-H_2O includes the major constituents of portland and high-alumina cements and the reaction products formed by the hydration of these materials. In connection with the hydrothermal study of parts of that system [1,2] [1] being conducted at the National Bureau of Standards, the heats of solution of the reaction products and of related minerals are being determined. The heats of solution of these materials and of the reactants from which they theoretically can be formed are measured in appropriate acid solutions in a precision-type calorimeter. The data, combined with literature values for the heats of formation of the reactants [3], permit the calculation of the heats of formation of substances related to the products of hydration of the cements. Appropriate thermochemical equations can be written and the computed heats of reaction can be compared with observed measurements [4,5] for the further elucidation of the hydration reactions occurring between water and hydraulic cements. The present paper gives the results of measurements made with calcium hydroxide and silica gel as reactants and of synthetic hillebrandite, $2CaO \cdot SiO_2 \cdot H_2O$, and xonotlite, $5CaO \cdot 5SiO_2 \cdot H_2O$, as products. In addition, the heat of solution of a sample of the mineral foshagite was determined.

2. Materials, Apparatus, and Procedure

2.1. Materials

Reagent-quality nitric and hydrofluoric acids, calcium carbonates (low alkali), calcium hydroxide, and precipitated silica (silicic acid) were used. Calcium hydroxide for heat-of-solution measurements was prepared by igniting $CaCO_3$ for 72 hours at 1,000° C and treating the resulting CaO with water [10] at 250° C for 2 days. The crystals of $Ca(OH)_2$ obtained were dried, without washing, in a vacuum over magnesium perchlorate and stored in a tightly stoppered bottle in a desiccator over saturated KOH until used. The ignition loss of this material was 24.30_7 percent, to be compared with 24.31_4 percent calculated from the formula.

The reagent-quality silicic acid used for the heat-of-solution measurements had a water content of 12.82 percent and a nonvolatile residue of 0.023 percent when treated with hydrofluoric acid. The silica was kept over saturated $MgCl_2 \cdot 6H_2O$ solution for 2 weeks before its heat of solution was determined. At that time the water content was about 20 percent. According to Mulert [9], whose data were used in calculating the heat of formation of SiO_2-aq given in reference [3], the heat of solution of hydrated silicic acid per mole of silica does not change with further increase in water content.

Xonotlite was prepared from $Ca(OH)_2$ and silicic acid. These materials were mixed together in a CaO/SiO_2 ratio of 1.000 by tumbling for several hours in a glass bottle with a few wooden balls. Twenty grams of this mixture was prepared and heated overnight at 950° C in a platinum dish, cooled in a desiccator and flooded with freshly boiled distilled water. The dish was transferred to a small bomb and heated at 250° C. The flooding and transfer of the dish and the closure of the bomb were made as rapidly as possible to minimize exposure to CO_2 in the air. The bomb was opened at the end of 2 weeks and the hardened mass of surface-dry material ground quickly to pass through a No. 28 sieve and dried for 2 hours in a vacuum over $Mg(ClO_4)_2$.

Three samples of synthetic hillebrandite, $C_2SH(B)$ [11], were prepared in a similar manner by heating the material with water at 242°, 178°, and 152° C for 7, 16, and 14 days, respectively. These samples also, as well as selected fibers of foshagite from Crestmore, Calif., were crushed rapidly to pass a No. 28 sieve and dried.

The samples were analyzed for SiO_2, $Fe_2O_3 + Al_2O_3$, CaO, and MgO by the methods described in Federal Specification SS–C–158c. Loss on ignition was determined by heating 1-g samples at 1,200° C. The CO_2 content was determined on 2-g samples, and the water content was taken as the difference between the loss on ignition and the CO_2 content. X-ray patterns, obtained by using a recording X-ray diffractometer with copper radiation 1.5418 A, were used to confirm the identity of the samples by comparison with published patterns [12].

[1] Figures in brackets indicate the literature references at the end of this paper.

TABLE 1. *Analyses of calorimeter samples*

Determinations	$Ca(OH)_2$	SiO_2-aq[a]	Xonotlite		Hillebrandite						Foshagite	
			Computed [b]	Observed	Computed [b]	Observed					Computed [b]	Observed
						1	2	3	4	5		
	%	%	%	%	%	%	%	%	%	%	%	%
Ignition residue	75.69	87.18	96.99	96.54	90.53	67.57	89.25	89.29	89.48	91.74	89.50	88.45
CaO	[c] 75.69	.....	46.83	45.91	58.96	(43.55)	57.52	(57.55)	58.64	60.03	54.49	48.91
SiO_2	.....	[c] 87.16	50.16	48.86	31.57	(23.89)	31.56	(31.57)	31.02	31.86	35.01	36.60
CO_2	0.15	.....	.....	0.27	.....	(1.27)	1.68	(1.68)	0.35	0.04	.....	2.67
H_2O [d]	24.16	12.82	3.01	3.19	9.47	(31.16)	9.07	(9.03)	10.17	8.22	10.50	8.88
R_2O_3	.....	.....	.....	0.21	.....	(0.09)	0.12	(0.12)	0.14	0.26	.....	0.50
MgO	.....	.....	.....	.31	.....	.....	.....	.....	.69	.08	.....	2.61
HF residue	.....	0.023	.....	.....	.....	.....	.....	.....	.....	.....	.....	.....
Analysis, total	100.00	100.00	100.00	98.75	100.00	(99.96)	99.95	(99.95)	101.01	100.49	100.00	100.17

[a] As taken from stock bottle. [b] Computed from formula $5CaO\text{-}5SiO_2\text{-}H_2O$ for xonotlite; $2CaO\text{-}SiO_2\text{-}H_2O$ for hillebrandite; and $5CaO\text{-}3SiO_2\text{-}3H_2O$ for foshagite. [c] By difference. [d] Loss on ignition minus CO_2.

The results of the chemical analyses are given in table 1. For easy comparison there are also included the analyses of the silicates computed from the formulas. The first sample of hillebrandite, prepared considerably before the others, was found to contain excess moisture. It was dried further and analyzed and its heat of solution again measured. Subsequently, its ignition loss and heat of solution were redetermined. This material appears as hillebrandite samples 1, 2, and 3 in the tables. Figures in parentheses in table 1 represent its analysis as sample 2 computed to its moisture content as samples 1 and 3.

The agreement between observed and calculated compositions was satisfactory for the synthetic preparations. The foshagite, however, had undergone considerable alteration. The sample consisted of selected fibers, taken from a 50-g fibrous mass. Perhaps 30 percent of the sample was of somewhat lower index than reported for foshagite, and some brownish material was present.

2.2. Apparatus and Procedure

The calorimeter has been adequately described elsewhere [6, 7]. It was operated so that the final temperature was always within a few hundredths of a degree of 25°C. Since the heat capacities of the reactants were used in computations, the isothermal heats of solution at 25°C were obtained. The energy equivalent of the calorimeter was determined electrically, using the defined calorie of 4.1840 absolute joules. The heat capacities of the samples, introduced at room temperature, were taken as 0.2 cal/deg-g. The calculated correction for the sensible heat introduced with a sample rarely amounted to as much as 0.05 cal/g.

The acid charge used had a total weight of 600.0 g, of which 11.0 ml (12.6 g) was 48 percent HF, the remainder being 2.000 N HNO_3 (at 25° C). Its composition therefore [8] was 0.30HF, 1.10 HNO_3, 29.10H_2O. The sample weight was generally 1 g. When silica gel containing 20 percent of H_2O was being dissolved, the HF/SiO_2 molar ratio was 22.8, well in excess of the value of six, beyond which the heat of solution of silica in hydrofluoric acid becomes constant [9]. It was observed that 3-g samples of portland cement containing about 1.8 g of combined CaO could be dissolved without precipitation of CaF_2, but that when dissolving $Ca(OH)_2$ alone the sample weight had to be reduced to 0.7 g. Under these conditions there was no weighable or visible precipitate of CaF_2, but with 0.8-g samples of $Ca(OH)_2$ a faintly visible haze remained in the solution after filtration had removed 0.6 mg of precipitated CaF_2. Consequently approximately 0.7-g samples of $Ca(OH)_2$ were used to determine the heat of solution of that substance. It was assumed that the heat of the dilution effects caused by the differences in the concentrations of the final solutions were negligible, and no corrections were made.

3. Results and Discussion

The observed heats of solution are given in table 2. The amount of $CaCO_3$ equivalent to the CO_2 was calculated for each sample, and its heat of solution, 86 cal/g [4], deducted from the observed heat of solution. The total CaO was reduced by an equivalent amount. The heats of solution of the samples per mole of SiO_2, A, were calculated by the formula $A=a(100\times60.06/P)$, where a is the observed heat of solution of the sample, corrected for CO_2, P is the percentage of silica in the sample as given in table 1, and 60.06 is taken as the molecular weight of SiO_2. These calculated values are given in table 3. Empirical formulas, calculated from table 1 corrected for CO_2, are also given in table 3. In making the foregoing calculations for the foshagite, an equivalent amount of CaO was substituted for the MgO found by analysis.

The heat of solution of C/S[2] moles of $Ca(OH)_2$ was calculated for each sample and added to the heat of solution of 1 mole of SiO_2, $0.828H_2O$ to determine the heats of solution of the reactants from which the

[2] Conventionally, CaO, SiO_2, and H_2O are represented by the letters C, S, and H, respectively, $2CaO\text{-}SiO_2\text{-}H_2O$ being represented by the formula C_2SH.

TABLE 2. *Results of calorimetric measurements*

Calorimeter energy equivalent	Heats [a] of solution								
	$Ca(OH)_2$ [b]	SiO_2-aq [c]	Xonotlite	Hillebrandite					Natural foshagite
				1	2	3	4	5	
cal/ohm [d]	*cal/g*	*cal/g*	*cal/g*	*cal/g*	*cal/g*	*cal/g*	*cal/g*	*cal/g*	*cal/g*
5723.2	429.97	468.72	490.87	[e] 354.4	462.40	460.62	470.47	490.39	437.94
5720.2	429.69	468.64	490.92	[e] 351.0	461.57	459.00	470.32	489.19	438.67
5716.9	429.32	466.81	490.67	.....	461.79	459.53	469.94	488.47	438.66
5718.8	429.31	470.86	491.66	.....	.....	459.46	469.14	488.51	439.31
5717.0	429.26	470.00	490.16	.....	.....	459.96	468.91	488.48	438.67
.....	430.24	468.51	490.42	.....	.....	459.36	469.29	489.39	437.27
Average 5719.2	429.63	468.92	490.78	352.7	461.92	459.66	469.68	489.07	438.42
Std. dev. of avg [f] 1.2	0.17	0.57	0.21	1.7	0.25	0.23	0.27	0.31	0.29

[a] 1-g sample in 600-g $HF+HNO_3$ mixture ($0.30HF$, $1.10HNO_3$, $29.10H_2O$).
[b] 0.7-g sample in 600-g $HF+HNO_3$ mixture ($0.30HF$, $1.10HNO_3$, $29.10H_2O$).
[c] Sample stored over saturated solution of $MgCl_2 \cdot 6H_2O$. Relative humidity 33 percent. Ignition residue of sample 80.11 percent, equivalent to 80.09 percent of SiO_2, 0.02 percent of HF residue, 19.89 percent of H_2O. $H/S=0.828$.
[d] $\Delta R/\Delta T$ is 0.1010 at 25° C; 5719.2 cal/ohm is approximately 577.6 cal/deg.
[e] 1-g sample in 425-g $HF+HNO_3$ mixture ($0.22HF$, $0.78HNO_3$, $20.61H_2O$) in vacuum-flask calorimeter.
[f] Standard deviation of average $=\sqrt{[\Sigma r^2-(\Sigma r)^2/n]/n(n-1)}$.

TABLE 3. *Heat of reaction of* $Ca(OH)_2$ *and* $SiO_2 \cdot 0.83H_2O$

Sample	Empirical Formula [a]	Heat of solution [b]		Heat of reaction, ΔH
		Products	Reactants	
		kcal/mole	*kcal/mole*	*kcal/mole*
$Ca(OH)_2$	$1.00CaO \cdot 1.00H_2O$	.....	[c] 31.88	.....
SiO_2-aq	$1.00SiO_2 \cdot 0.83H_2O$	.....	35.16	.....
Xonotlite	$0.98CaO \cdot 1.00SiO_2 \cdot 0.21H_2O$	59.06	66.40	−7.34
Hillebrandite:				
1	$1.88CaO \cdot 1.00SiO_2 \cdot 4.35H_2O$	88.04	95.09	−7.05
2	$1.88CaO \cdot 1.00SiO_2 \cdot 0.96H_2O$	87.31	95.09	−7.78
3	$1.88CaO \cdot 1.00SiO_2 \cdot 0.96H_2O$	86.82	95.09	−8.27
4	$2.01CaO \cdot 1.00SiO_2 \cdot 1.09H_2O$	90.80	99.24	−8.44
5	$2.02CaO \cdot 1.00SiO_2 \cdot 0.86H_2O$	92.18	99.56	−7.38
		Weighted average		−7.91
Foshagite	$1.44CaO \cdot 1.00SiO_2 \cdot 0.81H_2O$ [d]	71.13	81.06	−9.93

[a] Calculated from analysis, corrected for $CaCO_3$.
[b] Corrected for $CaCO_3$.
[c] Kilocalorie per mole of $Ca(OH)_2$.
[d] 2.61 percent of MgO assumed equivalent to 3.63 percent of CaO.

samples can be considered to be formed by the equation

$$(C/S)Ca(OH)_2+SiO_2,\ 0.828H_2O \rightarrow (C/S)CaO \cdot SiO_2 \cdot (H/S)H_2O+(C/S+0.828-H/S)H_2O+\Delta H. \quad (1)$$

The sum of the heats of solution of the reactants minus the heats of solution of the products is equal to the heat of the reaction. The partial molal heat content of the water in HNO_3, $26.3H_2O$ is approximately 0.002 kcal/mole; in HF, $100H_2O$ it is about 0.0004 kcal/mole [13]. These quantities, which represent approximately the heat of solution of the water produced in the reaction, are negligible.

In table 3 are given the calculated heats of reaction of $Ca(OH)_2$ and silica gel to form the samples used in this investigation. These values are given on the basis of 1 mole of silica. The hydrated calcium silicates as occurring in nature or as prepared in the laboratory have variable composition. On the assumption that the heats of reaction per mole of silica would be the same for the substances with formulas generally accepted [11], the heats of formation of $5CaO \cdot 5SiO_2 \cdot H_2O$, $2CaO \cdot SiO_2 \cdot H_2O$, and $5CaO \cdot 3SiO_2 \cdot 3H_2O$ from lime, quartz, and liquid water were calculated. To perform these calculations, the heat of formation [3] of $Ca(OH)_2$, SiO_2-aq, and liquid water were substituted in eq (1) together with the heats of reaction as determined from the heat-of-solution measurements. The heats of formation of the hydrated calcium silicates were then obtained as the sum of the heats of formation of the reactants plus the heat of the reaction minus the heat of formation

of the water appearing on the right side of eq (1). Using the heats of formation thus obtained for the silicates, thermochemical equations were written for the reactions forming $5CaO{\cdot}5SiO_2{\cdot}H_2O$, $2CaO{\cdot}SiO_2{\cdot}H_2O$, and $5CaO{\cdot}3SiO_2{\cdot}3H_2O$ from lime, quartz, and liquid water, and the heats of the reactions calculated in the usual manner [3]. The values obtained are given in table 4.

TABLE 4. *Heats of formation of hydrated calcium silicates*

Name	Bogue designation [11]	Formula [a]	Heat of formation, ΔH, from CaO(c), SiO_2(c, quartz) and H_2O(l)
			kcal/mole
Xonotlite	C_6S_6H	$5CaO{\cdot}5SiO_2{\cdot}H_2O$	−92.6
Hillebrandite	$C_2SH(B)$	$2CaO{\cdot}SiO_2{\cdot}H_2O$	−34.7±0.9
Foshagite	$C_4S_3H_2$	$5CaO{\cdot}3SiO_2{\cdot}3H_2O$	−94.6

[a] The heats of formation from the oxides are calculated on the basis of these formulas. The heats of reaction of the reactants $Ca(OH)_2$ and SiO_2-aq to form the individual compounds was taken from table 3 and the heats of formation of the reactants from the oxides calculated from NBS Circular 500 [3].

4. Summary

The heats of solution of synthetic xonotlite, hillebrandite, and natural foshagite have been determined in a mixture of nitric and hydrofluoric acids, and their heats of formation from the oxides have been calculated to be −92.6, −34.7, and −94.6 kcal/mole, respectively.

5. References

[1] R. B. Peppler and L. S. Wells, J. Research NBS **52,** 75 (1954) RP2476.
[2] R. B. Peppler, J. Research NBS **54,** 205 (1955) RP2582.
[3] Selected values of chemical thermodynamic properties, NBS Circular 500 (U. S. Government Printing Office, 1952).
[4] S. Brunauer, G. C. Hayes, and W. E. Hass, J. Phys. Chem. **58,** 279 (1954).
[5] C. Brisi, Ricerca sci. [7] 24, 1436 (1954).
[6] E. S. Newman and L. S. Wells, J. Research NBS **20,** 825 (1938) RP1107.
[7] E. S. Newman, J. Research NBS **54,** 347 (1955) RP2597.
[8] International Critical Tables, National Research Council (McGraw-Hill Book Co., Inc., New York, N. Y., 1933).
[9] O. Mulert, Z. anorg. u. allgem. Chem. **75,** 198 (1912).
[10] T. Thorvaldson and W. G. Brown, J. Am. Chem. Soc. **52,** 80 (1930).
[11] R. H. Bogue, Mag. of Concrete Research **14,** 87 (Dec. 1953).
[12] H. F. McMurdie and E. P. Flint, J. Research NBS **31,** 225 (1943) RP1560.
[13] L. S. Wells and K. Taylor, J. Research NBS **19,** 215 (1937) RP1022.

WASHINGTON, February 24, 1956.

Journal of Research of the National Bureau of Standards Vol. 57, No. 1, July 1956 Research Paper 2691

Effect of Camera Tipping on the Location of the Principal Point [1, 2]

Francis E. Washer

Asymmetric distortion is introduced in a lens-camera combination when the camera is incorrectly alined for calibration. A method is described whereby the magnitude and direction of the angle of camera tipping can be determined from analysis of the asymmetric values of distortion for the case of the object lying at equal but opposite angles from the central line of sight. The displacement of the central image from the principal point of autocollimation is then readily determined. Theoretical analysis of the problem is given and the results confirmed by experiment. The point of symmetry and the principal point of autocollimation coincide for the case of no prism effect present on the lens.

1. Introduction

One of the problems that arises during the calibration of precision aerial-mapping cameras is the accurate location of the proper principal point [1] [3] with respect to the center of collimation (the point determined by the intersection of lines joining opposite pairs of collimation index markers). The principal point in photogrammetry is defined as the point at the foot of the perpendicular drawn from the interior perspective center to the plane of the photograph. The proper manner of locating this point has long been a subject of discussion. There are at present three different procedures that are employed in locating a point which is believed to be a sufficiently close approximation to the true principal point.

The first method, which has enjoyed considerable popularity, locates a point called the principal point of autocollimation [2, 3], which is the center of the image formed in the emulsion plane by the camera lens from an incident beam of parallel light, which, in the object space, is perpendicular to the emulsion plane. This point has usually been designated "center cross" [4] by the writer for convenience. This point is located by the simplest of the three methods, and its popularity undoubtedly derives from this simplicity. To locate it, one needs only to aim an autocollimating telescope at a distant object. The camera is then interposed between the object and the telescope; a plane parallel plate with a mirror surface is pressed against the focal plane. With the aid of the autocollimating telescope, one can easily adjust the camera until its focal plane is normal to the line of sight of the telescope. The reflecting plate is then replaced by a photographic plate and the distant object is photographed. If the collimation index markers are simultaneously photographed, one can then easily locate the center cross with respect to the center of collimation.

The second method, which was developed at the Bureau, is based on the knowledge that most lenses suffer from small errors in centering that cause the lens to behave (in a first approximation) as though it were composed of a well-centered lens plus a thin prism [4, 5]. This is further accentuated in the calibration of precision cameras by the presence in front of the lens of a filter that is seldom truly plane parallel, which accordingly introduces a true prism effect. This prism effect causes a displacement of the center cross from the position it would have occupied in the absence of prism effect. This immediately poses the question as to which of these locations should properly be regarded as the principal point. It has been the custom at the Bureau to regard the point that would normally have been occupied by the center cross in the absence of prism effect as the proper principal point of the photograph. It is an invariant point when located under standard conditions of locating the center cross and is not affected by subsequent changes in filters having different degrees of surface parallelism. The actual shift of the principal point from the center cross is easily determined from analysis of the asymmetric distortion pattern produced by such prism effect.

The third method came out of attempts to calibrate cameras by a field method [6]. It was not customary nor readily practicable to aim the camera at the central target of a given target-array with the aid of an autocollimating telescope and, consequently, small errors of alinement sometimes were present. Such errors of alinement, called camera tipping, can produce an asymmetric distortion pattern similar but not identical to that produced by prism effect. In the analysis of the measurements made under these conditions of test, it was found possible to make the distortion pattern symmetrical by appropriate adjustment of the angles and image separations from the central image by computable increments. The point about which the distortion is tolerably symmetrical is called the point of symmetry.

It is evident that for an ideal lens-camera combination, where no tipping of the camera occurs and where there is no prism effect in the lens, all three methods will lead to the same result. In other words, for this case, the principal point of autocollimation (or center cross), the principal point, and the point of

[1] This is the second paper of a series dealing with problems that relate to the calibration of precision airplane mapping cameras (see reference [13] at the end of this paper).

[2] This work was sponsored in part by the U. S. Air Force.

[3] Figures in brackets indicate the literature references at the end of this paper.

symmetry will be identical. In the present paper, the effect of camera tipping on the displacement of the central image from the original position of the center cross is considered. The magnitude of the asymmetric distortion introduced by such tipping is evaluated theoretically and confirmed experimentally. A method of determining the magnitude of the angle of camera tipping is shown for the case of equal opposite angles. The identity of the principal point of autocollimation and the point of symmetry is shown for the case of a lens having no prism effect.

2. Effect of Improper Alinement of Camera for Test

When the camera is being calibrated under conditions such that the focal plane of the camera is not normal to the line drawn to it from the central target, the calibration data are likely to show the presence of asymmetric distortion [7, 8, 9]. This asymmetric distortion is sometimes confused with the asymmetric distortion produced by prism effect in the lens [4, 10]. It is, however, much simpler to eliminate the asymmetry of the distortion values arising from camera tipping than it is to eliminate or reduce the asymmetrical distortion arising from prism effect. In this section, the effect of camera tipping upon the values of focal length and distortion is considered.

2.1. Determination of the Equivalent Focal Length

In figure 1, N is the rear nodal point of an ideal lens, L; O is the point where a perpendicular dropped from N intersects the focal plane, consequently NO is equal to f, the equivalent focal length. The points of intersection with the focal plane of rays inclined at angles β with the optical axis are designated X and Y. As L is an ideal lens having no distortion,

$$OX=OY=f \tan \beta. \tag{1}$$

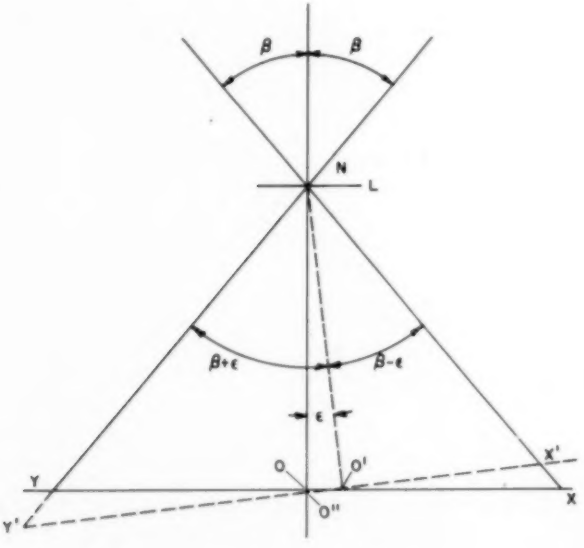

FIGURE 1. *Schematic drawing showing the image shift produced by rotating the camera by amount ϵ about an axis normal to the plane of the paper and passing through the rear nodal point N of the lens L.*

Let the camera be rotated by amount ϵ about a line through N normal to the plane of the paper. The foot of the perpendicular from N moves to O', the image of the central ray is at O'', and the images formerly found at X and Y are at X' and Y'. The relations connecting the various quantities and distances are

$$O'O''=f \tan \epsilon \tag{2}$$

$$O''X'=f \tan(\beta-\epsilon)+f \tan \epsilon \tag{3}$$

and

$$O''Y'=f \tan(\beta+\epsilon)-f \tan \epsilon. \tag{4}$$

The distances $O''X'$ and $O''Y'$ are the only quantities directly measurable. It is clear from figure 1 that

$$O''X'+O''Y'=f \tan(\beta-\epsilon)+f \tan(\beta+\epsilon) \tag{5}$$

or

$$O''X'+O''Y'=\frac{2f \tan \beta}{\cos^2 \epsilon(1-\tan^2 \beta \tan^2 \epsilon)}, \tag{6}$$

whence

$$f=\frac{O''X'+O''Y'}{2 \tan \beta} \cos^2 \epsilon(1-\tan^2 \beta \tan^2 \epsilon). \tag{7}$$

For small ϵ, the term $(1-\epsilon^2)$ can be substituted for $\cos^2 \epsilon$, and ϵ^2 for $\tan^2 \epsilon$. By neglecting the term in ϵ^4, eq (7) becomes

$$f=\frac{O''X'+O''Y'}{2 \tan \beta}[1-\epsilon^2(1+\tan^2 \beta)]. \tag{8}$$

For very small values of ϵ, the term in ϵ^2 can be dropped, and the expression becomes simply

$$f=\frac{O''X'+O''Y'}{2 \tan \beta}. \tag{9}$$

Thus, the equivalent focal length, f, can be determined to a good degree of approximation by using the measured values of $O''X'$, $O''Y'$, and the known value of β. The value of f, so determined, will be correct to the nearest thousandth of a millimeter for $\epsilon \leq 10$ min for values of the focal length of the order of 150 mm. If eq (9) is used when $\epsilon > 10$ min, the values of f will be higher than the true value, the error running as high as 0.012 mm for $\epsilon=30$ min. In such case it is necessary to determine ϵ by the method shown in a later portion of this paper and to use this value of ϵ in eq (8). The value of f determined with eq (8) agrees with the true value for values of ϵ as high as 30 min.

2.2. Asymmetric Distortion Produced by Improper Alinement

When a camera is tipped in the manner described in section 2.1, it is found that an asymmetric distortion is introduced by such tipping. This distortion affects the relative location in the image plane even as does the distortion inherent in the lens arising from lens aberrations. There is, however, one pronounced difference. Whereas distortion arising from lens aberrations is symmetric about the optical axis, distortion arising from camera tipping is decidedly asymmetric.

In this section, the magnitude of this asymmetric distortion will be derived in terms of β and ϵ for the case of a lens that is distortion-free as far as lens aberrations are concerned. By referring to figure 1, when distortion is computed from the measurable quantities in the usual manner, the distortion, D_1, on one side is

$$D_1=O''X'-OX \tag{10}$$

or

$$D_1=f[\tan(\beta-\epsilon)+\tan\epsilon-\tan\beta], \tag{11}$$

which may be written

$$D_1=f\tan\beta\tan\epsilon\frac{(\tan\epsilon-\tan\beta)}{1+\tan\beta\tan\epsilon}, \tag{12}$$

which for small values of ϵ is equivalent to

$$D_1=f\epsilon\tan\beta[\epsilon(1+\tan^2\beta)-\tan\beta(1+\epsilon^2)], \tag{13}$$

or on neglecting the term in ϵ^3,

$$D_1=-f\epsilon\tan^2\beta+\frac{f\epsilon^2\tan\beta}{\cos^2\beta}. \tag{14}$$

The distortion, D_2, for the other side is

$$D_2=O''Y'-OY \tag{15}$$

or

$$D_2=f[\tan(\beta+\epsilon)-\tan\epsilon-\tan\beta], \tag{16}$$

which for small values of ϵ can be shown to be

$$D_2=f\epsilon\tan^2\beta+\frac{f\epsilon^2\tan\beta}{\cos^2\beta}. \tag{17}$$

On inspection of the equations for D_1 and D_2, it is obvious that for small ϵ the second term containing ϵ^2 will be very small compared to the first term in both equations. It is, therefore, clear that D_1 is approximately equal to D_2 in magnitude but is opposite in sign. The effect of camera tipping is, accordingly, an introduction of a symmetric distortion whose magnitude is a function of β and ϵ. It is worthy of mention that, when one is analyzing the results of measurement made on a camera whose direction of tipping is unknown, the sign of the distortion values can serve as a guide in determining the angle of tipping and the resultant direction of displacement of the central image from the true position of the center cross or point of symmetry. The point of symmetry or true position of the center cross lies on the same side of the central image as those points showing maximum negative distortion. To express it another way, the central image is displaced from the center cross toward those points showing maximum positive distortion. To illustrate the effect of camera tipping, computed values of D_1 and D_2 are listed in table 1 for the case of a camera tipped through an angle $\epsilon=20$ min. Even for this relatively large amount of tip, it can be seen that D_1 is nearly equal to D_2 but is opposite in sign.

TABLE 1. *Asymmetric distortion, D_1 and D_2, induced in the image plane by tipping a camera, equipped with a lens having an equivalent focal length of 150 mm, through an angle $\epsilon=20$ min*

β	Distortion			
	Average asymmetric distortion		Resultant average distortion in image	
	D_1	D_2	$\frac{D_2-D_1}{2}$	$\frac{D_2+D_1}{2}$
deg	*mm*	*mm*	*mm*	*mm*
7.5	−0.014	0.016	0.015	0.001
15	−.061	.064	.063	.002
22.5	−.147	.152	.150	.002
30	−.287	.295	.291	.004
37.5	−.507	.520	.514	.006
45	−.863	.883	.873	.010

a. Evaluation of the Distortion

The values of the distortion assigned to a camera-lens combination are usually obtained by averaging the values measured at the two corresponding opposite angular separations from the axis along a single diameter. This corresponds to the evaluation of

$$D=\frac{D_1+D_2}{2}. \tag{18}$$

In the present case, the contribution of lens aberrations to the distortion has been assumed zero, so if D is not zero, the departure therefrom is a consequence of the camera tipping alone. It is evident that for small values of ϵ

$$\frac{D_1+D_2}{2}=\frac{f\epsilon^2\tan\beta}{\cos^2\beta}. \tag{19}$$

Values of D have been computed for selected values of ϵ and are shown in table 2. It is readily apparent that camera tipping does induce a resultant distortion that is not eliminated by the averaging process. This error in distortion produced by camera tipping can be safely neglected for values of ϵ less than 10 min but may assume serious proportions for values of ϵ greater than 20 min.

TABLE 2. *Distortion induced in a normally distortion-free lens by tipping the camera, equipped with a lens having an equivalent focal length of 150 mm, through a small angle* ϵ

β	Distortion for ϵ of—			
	10 min	20 min	30 min	1°
deg	*mm*	*mm*	*mm*	*mm*
7.5	0.000	0.001	0.002	0.006
15	.000	.002	.003	.013
22.5	.001	.002	.006	.022
30	.001	.004	.009	.035
37.5	.002	.006	.014	.056
45	.003	.010	.023	.091

For the case of a real lens having measurable inherent distortion, it may be inferred that the distortion at a given angle β is given reasonably closely by eq (18) provided that ϵ is kept less than 15 min. If one is dealing with a lens which is required to show less than $0\pm.020$ mm of distortion referred to the equivalent focal length, it is possible to induce an error of ± 0.003 mm in the distortion referred to the calibrated focal length if ϵ is as great as 30 min. It is also likely that small additional errors may arise in averaging for those values of β where the distortion characteristics of the lens are changing rapidly with β. Even in such instances, the errors in distortion will usually be small compared with the total distortion.

b. Evaluation of the Angle of Camera Tipping

When a camera is tested under conditions such that the test targets are symmetrically located about the central target, it is possible to evaluate ϵ, the angle of camera tipping, in a very simple manner. It can be shown for small values of ϵ that

$$\frac{D_1-D_2}{2}=-f\epsilon\tan^2\beta. \tag{20}$$

When D_1, D_2, f, and β are known, ϵ can be computed from the relation

$$\epsilon=\frac{(D_1-D_2)}{2f\tan^2\beta}. \tag{21}$$

This expression is, of course, computed for the case of a distortion-free lens but can be used quite satisfactorily for a lens having distortion arising fron lens aberrations. This apparent anomaly results from the fact that the lens aberration is symmetrical about the axis and has the same value at $+\beta$ and at $-\beta$. Consequently, when the difference, D_1-D_2, is formed, the contribution to this difference from lens aberration is negligible, the only real contribution being the difference in lens distortion between the angles $\beta+\epsilon$ and $\beta-\epsilon$, which is usually very small for small values of ϵ. This difference can become appreciable in regions where the distortion is changing rapidly with angle. In such cases, a correction can be made, if one knows the usual values of the distortion for the given type of lens, which usually will be satisfactory. Table 1 lists the value of $(D_2-D_1)/2$ for one case of camera tipping. If ϵ is evaluated from the values listed, it will be found that the above approximation (eq (21)) yields the correct value of ϵ.

The value of the equivalent focal length, f, used in eq (21) is the approximate value determined with the aid of eq (9). The departure of this value of f from its corrected value will usually be too small to affect significantly the accuracy of the determination of ϵ. However, the value of ϵ, derived from eq (21), is sufficiently accurate for use in eq (8) to determine the correct value of the equivalent focal length f.

2.3. Point of Symmetry

It is clear from the foregoing discussion that if a camera is not properly alined for test and if computations of equivalent focal length and distortion are nonetheless performed in the usual manner, marked asymmetries in the distortion pattern will appear. The magnitude of the asymmetry will, of course, depend upon the amount the camera is tipped from the condition of proper alinement. In the field calibration method when the camera is not initially so alined that the focal plane is normal to the line connecting the front nodal point of the lens and the center target, an appreciable amount of asymmetric distortion is introduced. Methods have been developed that tend to reduce the magnitude of the asymmetric distortion. This usually involves locating a new point in the image plane with respect to which the distortion pattern becomes more nearly symmetrical. This point is called the "point of symmetry" [6, 11].

In the absence of prism effect, point O in figure 1 is the principal point of the camera, and the distance $O'O''$ is the shift of the central target image from the principal point. As $O'O''=f\tan\epsilon$, and as the value of $f\tan\epsilon$ can be deduced from the measured value of the asymmetric distortion for a given value of β, the location of the principal point can be determined. For this condition the principal point and point of symmetry are identical.

When both prism effect and camera tipping are present, the value of $f\tan\epsilon$ gives the location of the point of symmetry for a selected value of β. For these conditions, the principal point and the point of symmetry do not coincide.

3. Experimental Verification for Tipped Camera

In the calibration of precision cameras by the field method, it is usual to locate a point about which the distortion is symmetrical. This point is called the point of symmetry [6] and this point is sometimes set into coincidence with the center of collimation instead of setting the principal point into coincidence with the center of collimation. The prevailing practice at most calibrating laboratories is to set either the principal point or the principal point of autocollimation [2] into coincidence with the center of collimation (or fiducial center). The principal point is located at the foot of the perpendicular dropped from the center of the exit pupil for the paraxial rays

to the image plane and is the point customarily brought into coincidence with the center of collimation by the Bureau. The principal point of autocollimation is the image of an infinitely distant point located in the object space on a line perpendicular to the focal plane of the camera. This point is identical to the point referred to as the center cross in calibration made by the Bureau. In the absence of prism effect, the point of symmetry, principal point, and the center cross should coincide. The truth of the foregoing assertion is readily proved experimentally and the balance of this section is devoted to a simple experimental proof.

3.1. Experimental Arrangement

The camera selected for test was one which on calibration has been found to have negligible prism effect. The separation of the principal point and the center of collimation was less than 0.010 mm; and the separation of the center cross and the principal point was too small to be measured. This camera was placed on the camera calibrator and tipped about a horizontal axis lying in a plane defined by the optical axes of the collimator banks III and IV (see figures 2 and 3 for diagrammatic sketches of the trace of this plane in the focal plane of the camera). To achieve a measured amount of camera tipping, a small prism was mounted in front of the autocollimating telescope, and the telescope alined to point at the center of the reticle in the central collimator of the camera calibrator. The prism was then removed. The camera under study was then placed in position on the calibrator. An optical plane parallel was set on the focal plane and the camera was tipped until its focal plane was normal to the optical axis of the autocollimating telescope. The measured deviation of the line of sight produced by the prism was 0.2583°. The tip of approximately 15 min accordingly may be expected to produce its maximum effect along the diagonal that is the intersection of the focal plane and the plane defined by the optical axes of the collimators in banks I and II.

In making the first negative (hereafter referred to as plate 1A), the camera was so oriented in azimuth, that marker A (which designates the line of flight) lay between the radial rows of images formed by the camera lens of the targets contained in the collimators of banks II and IV. Because of the tipping, all of the collimation markers are moved with respect to the target images toward quadrant I. Accordingly when the location of the central image is determined with respect to the center of collimation, O, it will be displaced from the center of collimation along the diagonal toward the corner of quadrant II. The amount of this tip was measured directly and found to be approximately 0.2583°. In making the second, or check, negative (plate 2B), the camera is rotated 180° about the optic axis of the lens with all other conditions remaining unchanged. Accordingly for plate 1A, the central image should appear in the quadrant *AOD*, and displaced from *O* in direction II, while for plate 2B, the central image should appear in the quadrant *BOC* and displaced from *O* in the direction II. In the 180° rotation the direction II remains unchanged and *AOD* is replaced by *BOC*.

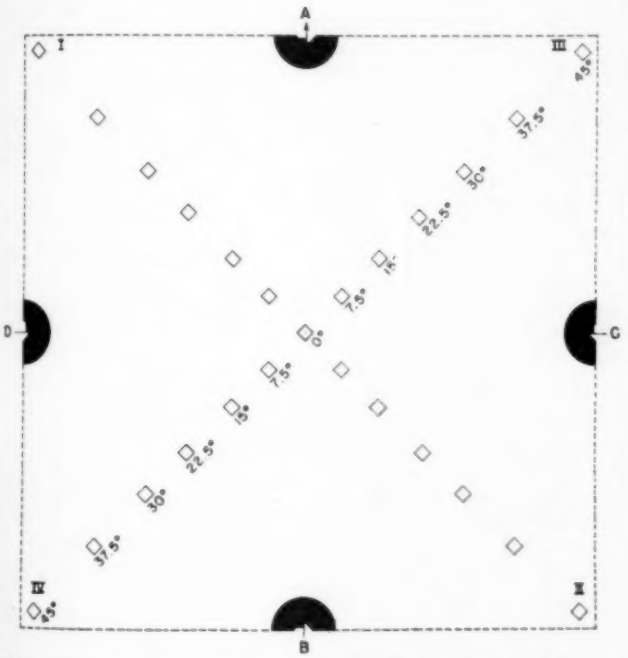

FIGURE 2. *Schematic drawing of test negative obtained on camera calibrator showing the position of the collimation markers A, B, C, and D and the images of the various collimator targets.*

The four radial banks are indicated by the numerals I, II, III, and IV. This figure is to be considered in connection with plate 2B, figure 4.

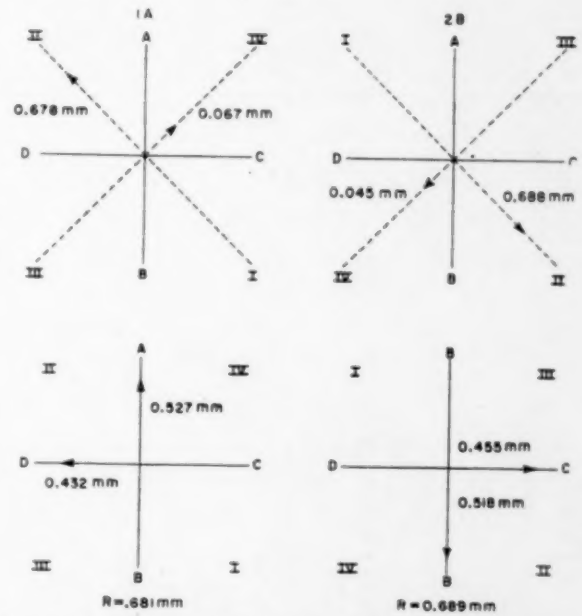

FIGURE 3. *Displacement of the center image from the center of collimation produced by a camera tipping of approximately 15 min.*

The upper sketches show the displacements computed from the distortion measurements. The lower sketches show the displacement resolved along the coordinate axes defined by the collimation index markers.

3.2. Results of Measurement

The distances separating all images on the negative from the image of the central collimator target were measured and are listed in tables 3 and 4 under the heading r. (The image of the central collimator target corresponds to O'' in figure 1, and the values of r are the measured values of $O''X'$ and $O''Y'$ for a series of values of β.) The symbols at the top and bottom of the columns headed $f \tan \beta$ indicate the orientation of the row of images with respect to the collimator banks and the fiducial markers in the focal plane (see figs. 2 and 3). The values of equivalent focal length were determined with the aid of eq (9) using the measured values of β, and the value of f for each diameter appears at the top of the proper column. By using the proper f for each set of measurements, the values of $f \tan \beta$ are computed, and the value of the distortion, D, obtained from the relation

$$D = r - f \tan \beta. \tag{22}$$

These values are shown under the headings $f \tan \beta$ and D. It is clear from the measurements that the principal effect has been produced along the directions I and II as planned. The asymmetric distortion appearing along the diameter I and II is shown graphically as curve 1 in figure 5. It may be noted that D_I (hereafter referred to as I) and D_{II} (hereafter designated II), although opposite in sign, are of unequal magnitudes. This difference in magnitude is, in large part, a consequence of the large value of distortion inherent in the lens itself.

TABLE 3. *Measured values of distances separating images at angle β from the center image for plane 1A*

Camera tipped by approximately 15 min (deviation of normal by 0.5 prism diopter). D is the distortion for each angle.

β	f=153.368 mm C I B			f=153.359 mm B III D		
	r	$f \tan \beta$	D	r	$f \tan \beta$	D
deg	*mm*	*mm*	*mm*	*mm*	*mm*	*mm*
45	152.368	153.197	−0.829	153.259	153.508	−0.249
37.5	117.234	117.562	−.328	117.784	117.785	−.001
30	88.313	88.464	−.151	88.653	88.612	.041
22.5	63.389	63.467	−.078	63.585	63.572	.013
15	41.023	41.062	−.039	41.126	41.126	.000
7.5	20.168	20.184	−.016	20.203	20.202	.001
0	0	0	0	0	0	0
7.5	20.184	20.168	0.016	20.204	20.205	−0.001
15	41.121	41.061	.060	41.127	41.108	.019
22.5	63.633	63.474	.159	63.609	63.563	.046
30	88.775	88.467	.308	88.695	88.616	.079
37.5	118.029	117.563	.466	117.848	117.778	.070
45	153.690	153.205	.485	153.378	153.512	−.134
	A II D			C IV A		

TABLE 4. *Measured values of distances separating images at angle β from the center image for plate 2B*

Conditions identical with those for 1A except camera is rotated 180° about its optical axis.

β	f=153.341 mm D I A			f=153.356 mm A III C		
	r	$f \tan \beta$	D	r	$f \tan \beta$	D
deg	*mm*	*mm*	*mm*	*mm*	*mm*	*mm*
45	152.346	153.170	−0.824	153.280	153.504	−0.224
37.5	117.222	117.542	−.320	117.793	117.782	.011
30	88.299	88.449	−.150	88.655	88.610	.045
22.5	63.386	63.456	−.070	63.586	63.570	.016
15	41.020	41.055	−.035	41.127	41.125	.002
7.5	20.164	20.181	−.017	20.204	20.202	.002
0	0	0	0	0	0	0
7.5	20.181	20.164	0.017	20.202	20.204	−0.002
15	41.121	41.054	.067	41.120	41.107	.013
22.5	63.630	63.463	.167	63.601	63.561	.040
30	88.769	88.452	.317	88.682	88.614	.068
37.5	118.026	117.543	.483	117.829	117.775	.054
45	153.701	153.178	.523	153.356	153.508	−.152
	B II C			D IV B		

These values are shown under the headings $f \tan \beta$ and D. It is clear from the measurements that the principal effect has been produced along the directions I and II as planned. The asymmetric distortion appearing along the diameter I and II is shown graphically as curve 1 in figure 5. It may be noted that D_I (hereafter referred to as I) and D_{II} (hereafter designated II), although opposite in sign, are of unequal magnitudes. This difference in magnitude is, in large part, a consequence of the large value of distortion inherent in the lens itself.

a. Evaluation of the Angle of Camera Tipping

Tables 5 and 6 show the evaluation of the angle of camera tipping ϵ from the distortion arising from the camera tipping. Values of $f \tan \epsilon$ are computed from the relation

$$f \tan \epsilon = \frac{D_2 - D_1}{2 \tan^2 \beta} \tag{23}$$

derived in section 2.2 (b). For convenience in computation, the average values of $\tan \beta$ and $\tan^2 \beta$ for the actual measured angles are listed in table 7. The values of $f \tan \epsilon$ are quite constant for the larger angles of β for any one set of computations. For plate 1A the values range from 0.658 mm at 45° to 0.691 mm at 30°, with the values of 22.5° and 37.5° falling within this range. The simple average for these four values is 0.678 mm, with the maximum departure being −0.020 at 45° for a deviation of approximately 3 percent. This spread of values can be appreciably reduced if one corrects for the presence of distortion, which in this case would raise the value of $f \tan \epsilon$ at 45° by 0.018 to 0.676 while producing changes not exceeding ±0.002 mm for any of the other three values. Although this would substantially reduce the spread, this correction changes the average by less than 1 percent; it does not therefore appear worthwhile to include it in the present discussion. The values of $f \tan \epsilon$ at the smaller values of β are less reliable, as a small error in r produces a large error in $f \tan \epsilon$; for example, an error of ±0.001 mm in r at β=7.5° produces an error in $f \tan \epsilon$ of ±0.029 mm. The values of $f \tan \epsilon$ at 7.5° and 15° accordingly are not used in evaluating the average value of $f \tan \epsilon$. This type of error decreases rapidly with increasing β and becomes negligible for angles greater than 30°. Some of the small discrepancies at the larger angles doubtless arise as mentioned from the small differences in lens distortion at $\beta+\epsilon$ and $\beta-\epsilon$ which are small but noticeable for large ϵ. These errors are, however, small in comparison to the larger values of $f \tan \epsilon$.

TABLE 5. *Computation of f tan ϵ or displacement of the center image induced by camera tipping from distortion values in Table 3 for plate 1A*

β	I	II	$\frac{II-I}{2}$	f tan ϵ
deg	mm	mm	mm	mm
45	−0.829	0.485	0.657	0.658
37.5	−.328	.466	.397	.676
30	−.151	.308	.230	.691
22.5	−.078	.159	.118	.688
15	−.039	.060	.050	.698
7.5	−.016	.016	.016	.924
Average (22.5° to 45°) f tan ϵ=0.678 mm, tan ϵ=0.004421, and ϵ=0.2533°.				
β	III	IV	$\frac{IV-III}{2}$	f tan ϵ
deg	mm	mm	mm	mm
45	−0.249	−0.134	0.058	0.058
37.5	−.001	.070	.036	.061
30	.041	.079	.019	.057
22.5	.013	.046	.016	.093
15	.000	.019	.008	.111
7.5	.001	−.001	−.001	−.058
Average (22.5° to 45°) f tan ϵ=0.067 mm, tan ϵ=0.000437, and ϵ=0.0250°. Resultant f tan ϵ=0.681 mm, resultant tan ϵ=0.004440, and ϵ=0.2544°.				

TABLE 6. *Computation of f tan ϵ or displacement of the center image induced by camera tipping from the distortion values in table 4 for plate 2B*

β	I	II	$\frac{II-I}{2}$	f tan ϵ
deg	mm	mm	mm	mm
45	−0.824	0.523	0.674	0.675
37.5	−.320	.483	.402	.684
30	−.150	.317	.234	.703
22.5	−.070	.167	.118	.689
15	−.035	.067	.051	.711
7.5	−.017	.017	.017	.982
Average (22.5° to 45°) f tan ϵ=0.688 mm, tan ϵ=0.004486, and ϵ=0.2570°.				
β	III	IV	$\frac{IV-III}{2}$	f tan ϵ
deg	mm	mm	mm	mm
45	−0.224	−0.152	0.036	0.036
37.5	.011	.054	.022	.037
30	.045	.068	.012	.036
22.5	.016	.040	.012	.070
15	.002	.013	.006	.083
7.5	.002	−.002	−.002	−.115
Average (22.5° to 45°) f tan ϵ=0.045 mm, tan ϵ=0.000293, and ϵ=0.0168°. Resultant f tan ϵ=0.689, resultant tan ϵ=0.004492, and ϵ=0.2574°.				

Although care was taken to ensure that the maximum effect of camera tipping would take place along diagonals I and II, the setting in azimuth was not quite perfect so a small effect of the tip manifested itself in directions III and IV. The computation of this component of f tan ϵ is shown in the lower portions of tables 5 and 6. The full magnitude of f tan ϵ is then obtained by finding the square root of the sum of the squares of the two orthogonal components. The resultant f tan ϵ for plate 1A is 0.681, and the corresponding value for plate 2B is 0.689. It is evident that excellent agreement exists between the values, even though the camera was rotated 180° and the direction of the effect thereby reversed.

TABLE 7. *Values of average tangent and tangent squared for use in interpreting data from camera calibrator*

The measured values of β are used in computing tan β.

β	tan β	tan $^2\beta$
COLLIMATOR BANKS I AND II		
deg		
7.5	0.1315530	0.0173062
15	.2677322	.0716805
22.5	.4138446	.1712674
30	.5768210	.3327225
37.5	.7665412	.5875854
45	.9989116	.9978244
COLLIMATOR BANKS III AND IV		
7.5	0.1317395	0.0173553
15	.2681092	.0718825
22.5	.4144998	.1718101
30	.5778216	.3338778
37.5	.7680095	.5898386
45	1.0009800	1.0019610

The values of f tan ϵ computed from the measurements of plates 1A and 2B are the amounts by which the center image has been displaced from the position it occupies when the camera under test has been properly oriented by autocollimation. As the center image was initially in near coincidence with the center of collimation, the computed displacement, f tan ϵ, can be regarded as a displacement with respect to the center of collimation. The magnitudes and directions of f tan ϵ derived from tables 5 and 6 are shown in the upper part of figure 4 for plates 1A and 2B. In the lower part of the figure, the displacements, originally determined along the diagonals, have been resolved into their components along AB and CD, which form the reference system afforded by lines connecting opposite pairs of collimation index markers. The resultant, R, for each plate is shown at the bottom. It is clear that there is remarkably good agreement between the values of R for plates 1A and 2B.

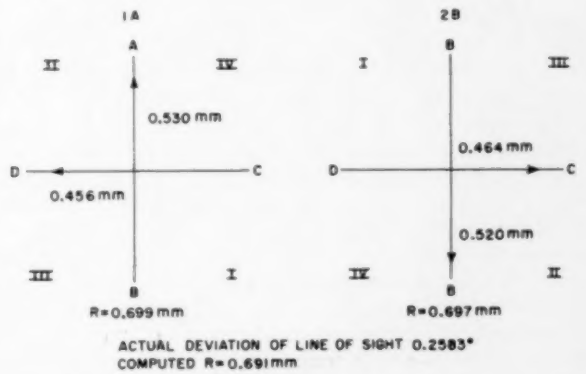

FIGURE 4. *Measured displacement of the center image from the center of collimation on plates 1A and 2B.*

The computed R is the resultant displacement expected for the measured amount of camera tipping introduced.

Finally, the positions of the displaced center image were measured on the plates themselves with respect to the center of collimation. The results of these measurements are shown in figure 4. Also shown in the lower part of figure 4 is the actual measured value of the induced angle of camera tipping, which is 0.2583°, and the computed value of $f \tan \epsilon$ derived from this value of ϵ. Comparison of these results with those shown in figure 3 demonstrates that the displacements of the center image computed from the asymmetrical values of the distortion agree in direction and magnitude with the observed shift that actually took place. The small discrepancies that remain may be attributed to several factors that include the presence of a small residual prism in the lens, small additional distortions induced by tipping not completely compensated, small amounts of plate curvature, and small errors in r and β.

Accordingly the resultant $f \tan \epsilon$ has been determined in three ways with the following results: (1) $f \tan \epsilon$ has been computed from the measured values of the asymmetric distortion, and its average value for plates 1A and 2B is 0.685 mm; (2) $f \tan \epsilon$ has been measured directly on the negative with respect to the center of collimation, and its average value for plates 1A and 2B is 0.698; (3) finally, $f \tan \epsilon$ has been computed on the basis of the known value of the induced camera tipping, and its value is 0.691. In view of the relatively large value of $f \tan \epsilon$, it is clear that excellent agreement exists among the three methods. This accordingly justifies the use of eq (23) in evaluating the angle of camera tipping from the asymmetric values of distortion and provides a simple method of locating the point of symmetry on the basis of distortion measurements.

b. Evaluation of the Distortion

In point of symmetry operations, it is customary to equalize the distortions. This can be done in the present case by subtracting the distortion produced by tipping from the measured values. This is done in table 8 for one diagonal of plate 1A. In table 8, column 1 lists the values of the measured asymmetric distortion for one diagonal, and column 2 lists the average asymmetric distortion computed for $f \tan \epsilon = 0.678$ mm. By adding the values in 2 to those in 1, the resultant lens distortion is obtained, which is shown in column 3. The distortion values in 3 are nearly equal for corresponding values of β. This process is shown graphically in figure 5. In the figure, curve 1 shows the values of the distortion computed with the displaced central image as the center. Curve 2 shows the amount of this distortion attributable to camera tipping. Curve 3 shows the amount of distortion still remaining after the correction for camera tipping is applied. It is evident that curve 3 is already quite symmetrical and closely approximates a typical distortion curve for this variety of wide-angle lens. In the table, column 4 shows the complete equalization obtained by averaging. Column 5 shows the difference between 3 and 4 and leads to the belief that complete equalization was not achieved because of the introduction

TABLE 8. *Adjustment of distortion values from tipped camera data for plate 1A, collimator banks I and II*

EFL=153.368 mm, $f \tan \epsilon = 0.678$ mm, CFL=153.310 mm.

β	1 [a]	2	3	4	5	6	7
deg	*mm*	*mm*	*mm*	*mm*	*mm*	*mm*	*mm*
45	−0.829	0.678	−0.153	−0.172	0.019	0.058	−0.114
37.5	−.328	.398	.070	.069	.001	.044	.113
30	−.151	.226	.075	.078	−.003	.033	.111
22.5	−.078	.116	.038	.040	−.002	.024	.064
15	−.039	.049	.010	.010	.000	.016	.026
7.5	−.016	.012	−.004	.000	−.004	.008	.008
0	0	0	0	0	0	0	0
7.5	.016	−0.012	.004	.000	.004	-----	-----
15	.060	−.049	.011	.010	.001	-----	-----
22.5	.159	−.116	.043	.040	.003	-----	-----
30	.308	−.226	.082	.078	.004	-----	-----
37.5	.466	−.398	.068	.069	−.001	-----	-----
45	.485	−.676	−.191	−.172	−.019	-----	-----

[a] Column:
1. Initial asymmetric values of distortion.
2. $f \tan \epsilon \tan^2 \beta$ (contribution from camera tipping).
3. Value of distortion compensated for camera tipping.
4. Averaged values of distortion referred to equivalent focal length.
5. Departure of compensated distortion from average.
6. $\Delta f \tan \beta$, where $\Delta f = 0.058$ mm.
7. Values of distortion referred to calibrated focal length.

of a small amount of residual distortion induced by plate tipping. Column 6 shows the correction in distortion introduced by changing from the EFL to the CFL by amount $\Delta f = 0.058$ mm. Column 7 shows the values of the distortion referred to the calibrated focal length. These final values of the distortion referred to the CFL are nearly the same as those obtained from the properly oriented camera; the small differences arising from the uncompensated distortion introduced by camera tipping, which in this instance would not exceed ± 0.003 mm.

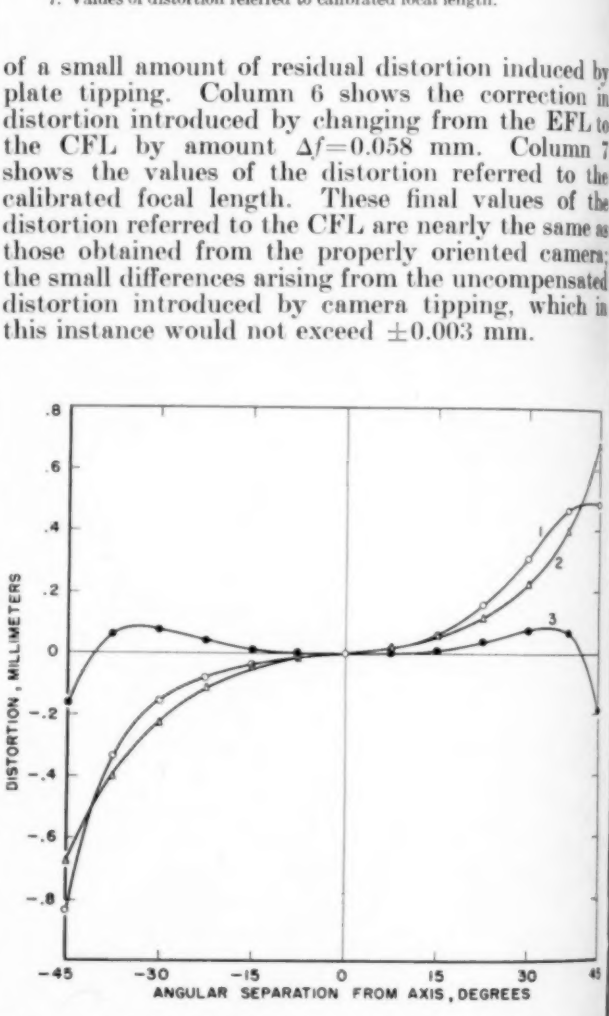

FIGURE 5. *Evaluation of the true values of distortion from the asymmetric measured values.*

The open circles (curve 1) show the actual values of distortion as initially determined from the measurements. The triangles (curve 2) show the values of asymmetric distortion produced by a tipping of amount $\epsilon = 0.2533°$ (see table 8 or 15.2 min. The closed circles (curve 3) show the symmetrical distortion pattern remaining when curve 2 is subtracted from curve 1.

4. Discussion

When a camera under calibration is initially so alined that the focal plane of the camera is not normal to the line joining the front nodal point of the lens and the distant target, the values of the distortion based on the assumption that the central image is indeed in its proper position will be asymmetrical about this point. The values of the distortion at points located at equal but opposite angles from the center can be used to evaluate the magnitude and direction of the displacement of the central image from its position for the condition of true normality. On making this correction, which can be done in a simple manner, the point of symmetry can be readily located. For the case of no prism effect on the lens, the point so located is the point of autocollimation or center cross. Accordingly it is clear that for these conditions, the point of autocollimation and point of symmetry are identical and can be regarded as the true principal point of the camera.

The author expresses his appreciation to other members of the staff for assistance rendered during the course of this work. The negatives used in the confirmatory experiments were made by W. P. Tayman. Measurements on the negatives were made by W. R. Darling. The drawings were made by E. C. Watts.

5. References

[1] United States Department of Agriculture Specification No. A–APC–1102 (as approved March 1940).

[2] Report of International Commission I—Proposal for international photogrammetric lens tests, Photogrammetria **III,** 103 (1950–1951).

[3] R. H. Field, A device for locating the principal point markers of air cameras, The Canadian Surveyor, July 1949 (N. R. C. No. 1979).

[4] F. E. Washer, Locating the principal point of precision airplane mapping cameras, J. Research NBS **27,** 405 (1941) RP1428.

[5] F. E. Washer and F. A. Case, Calibration of precision airplane mapping camera, Photogrammetric Engineering **XVI**, 502 (1950); J. Research NBS **45,** 1 (1950) RP2108.

[6] E. D. Sewell, Field calibration of aerial mapping cameras, Photogrammetric Engineering, **XVI**, 363, (1948); Manual of Photogrammetry by the American Society of Photogrammetry, 137-176 (1952).

[7] J. V. Sharp and H. H. Hayes, Effect on map production of distortions in photogrammetric systems, Photogrammetric Engineering **XV,** 159 (1949).

[8] J. V. Sharp, Increased accuracy of the multiplex system, Photogrammetric Engineering **XV,** 430 (1949).

[9] J. V. Sharp, Basic factors in photogrammetric instrument performance, Photogrammetric Engineering **XVI,** 118 (1950)

[10] P. D. Carman, Photogrammetric errors from camera lens decentering, J. Opt. Soc. Am. **39,** 951 (1949).

[11] R. Roelofs, Distortion, principal point, point of symmetry and calibrated principal point, Photogrammetria **II,** 49 (1950–1951).

[12] W. Roos, Über die Definition des Bildhauptpunktes und der Aufnahmeachse, Allgem. Vermess Nachr. (Bildm. u. Luftbildwesen), p. 235 (1950).

[13] F. E. Washer, Sources of error in various methods of airplane camera calibration. Photogrammetric Engineering **XXII** (to be published in September 1956).

WASHINGTON, March 22, 1956.

Journal of Research of the National Bureau of Standards Vol. 57, No. 1, July 1956 Research Paper 2692

Mass Spectra of Some Lead Alkyls

Edith I. Quinn, Vernon H. Dibeler, and Fred L. Mohler

Monoisotopic mass spectra are given for the compounds: tetramethyllead, trimethylethyllead, dimethyldiethyllead, methyltriethyllead, tetraethyllead, tetrapropyllead, trimethyl-*n*-butyllead, trimethyl-*sec*-butyllead, trimethyl-*tert*-butyllead, and tetra-*iso*-butyllead. Relations between relative probabilities of ion formation and molecular structure are observed for several ion configurations and are discussed briefly.

1. Introduction

The systematic comparison of the mass spectra of a group of related compounds not only affords a basis for chemical analysis but also provides information on the molecular structure and relative probabilities of bond dissociation processes. Organometallic compounds are particularly interesting for this purpose, and studies of mass spectra have been reported for a number of these, including the tetramethyl compounds of the group IV elements [1],[1] lead and mercury alkyls [2], and the cyclopentadienyl compounds of V, Cr, Fe, Co, Ni, Re, Ru, Mn, and Mg [3].

The concomitant data of isotope abundance ratios obtained for the metallic elements in organometallic compounds is also of interest. Although possible interference from ions formed by rearrangement during the ionization-dissociation process (e. g., hydride ions) preclude their use for discovering rare isotopes, satisfactory agreement has been obtained in the comparison of routine analyses of lead, using the halides and the tetramethyl compound [4], and of mercury, using the element and the dimethyl compound [5].

The present study, made possible through a gift of the lead alkyls from the Ethyl Corp., Detroit, extends the published mass spectral data of lead alkyls to include trimethylethyllead, dimethyldiethyllead, methyltriethyllead, tetra-*n*-propyllead, trimethyl-*n*-butyllead, trimethyl-*sec*-butyllead, trimethyl-*tert*-butyllead, and tetra-*iso*-butyllead. Relative dissociation probabilities are compared for the several molecules and conclusions noted with regard to molecular structure and mass spectra.

2. Experimental Details

Mass spectra were obtained by using a Consolidated 21–103 mass spectrometer and conventional procedures. In preliminary experiments, liquid samples were introduced through a gallium-covered porous glass frit [6]. However, considerable holdup was observed for the heavier liquids, and as a result the sample pressure did not reach a steady value and pump-out time was excessive. The use of a mercury-sealed orifice [7] avoids these difficulties. There was no indication of reaction between the mercury and the lead alkyls.

[1] Figures in brackets indicate the literature references at the end of his paper.

A resolving power of about 1 in 500 was obtained by reducing the width of the collector slit from 32 to 6 mils and by the use of a high potential on the "metastable suppressor." This electrode is located between the collector slit and the collector, and in addition to filtering out ions that have lost energy through metastable transitions, it also acts as a virtual limiting slit.

Table 1 lists the lead alkyls and the purities as stated by the supplier. The tetramethyllead and tetraethyllead were part of the same samples used in a previous study [2]. Recognized impurities in the samples were principally alkyl halides, except in the case of the trimethyl-*tert*-butyllead, which contained *tert*-butanol in excess of the total reported impurity and may have resulted from some decomposition of the sample. Mass spectral contributions of these impurities were subtracted from the lead alkyl spectra. Impurities consisting of other organo-lead compounds are not easily identified. One check on the purity is to compare the spectrum of the vapor in contact with an excess of liquid with the spectrum obtained when a small sample of liquid is completely vaporized. In the first spectrum, lower vapor-pressure impurities are suppressed whereas those with higher vapor pressures are enhanced. This technique disclosed approximately 0.1 percent of trimethylethyllead and dimethyldiethyllead in the tetramethyllead sample.

TABLE 1. *Purity of lead alkyls as reported by the supplier*

Compound	Formula	Purity
		%
Trimethylethyllead	$(CH_3)_3PbC_2H_5$	99+
Dimethyldiethyllead	$(CH_3)_2Pb(C_2H_5)_2$	99
Methyltriethyllead	$CH_3Pb(C_2H_5)_3$	99+
Tetra-*n*-propyllead	$(n\text{-}C_3H_7)_4Pb$	95
Trimethyl-*n*-butyllead	$(CH_3)_3Pb(n\text{-}C_4H_9)$	95
Trimethyl-*sec*-butyllead	$(CH_3)_3Pb(sec\text{-}C_4H_9)$	95
Trimethyl-*tert*-butyllead	$(CH_3)_3Pb(tert\text{-}C_4H_9)$	99
Tetra-*iso*-butyllead	$(i\text{-}C_4H_9)_4Pb$	95

The relative abundance of lead isotopes in natural ores is subject to large variations. "Common lead," which is frequently a mixture from several sources, may also exhibit variations. In this research, the isotope ratios are computed independently for each compound. However, as the preparation of the samples dates to 1934 and the

origin of the leads is unknown, small variations in the isotope ratio observed in these samples, although probably real, are not a matter of scientific interest.

3. Results

The polyisotopic spectra of the lead alkyls have been submitted for publication elsewhere [8]. As dissociation processes are difficult to interpret from mass spectra of molecules containing elements with a number of isotopes of comparable abundance, monoisotopic spectra are computed. First, contributions of ions containing C^{13} and D are subtracted in the conventional manner by using a C^{12}/C^{13} ratio of 91.0 and an H/D ratio of 6700. Common lead is composed of four isotopes with the approximate percentage abundances: 204:206:207:208=1.3:26:21:52. Thus each ion of formula $Pb(R)_n$ gives rise to four mass peaks in addition to the peaks resulting from ions containing C^{13} and D atoms. A method for obtaining the isotope abundance ratios and applying them to the computation of the monoisotopic spectra has been described in detail [1, 2].

Table 2 summarizes the principal ions in the 70-v monoisotopic spectra of 10 lead alkyls, including tetramethyl and tetraethyllead. The abundances are relative to the most abundant ion taken as 100. Observed molecule ions are in boldfaced type. The sensitivities (ion current per unit of pressure in the sample reservoir) of the most abundant ions are expressed as relative to the sensitivity of the $C_3H_7^+$ ion of *n*-butane. These appear in the last line of the table.

4. Discussion

The hydrocarbon ions in general, and particularly the methyl ions in the lead alkyl mass spectra, may exhibit variations in relative abundance for instrumental reasons, and conclusions based thereon are subject to some uncertainty. Nevertheless, some interesting results are observed. The relative abundance of the CH_3^+ ions in tetramethyllead, the methylethylleads, and tetraethyllead consistently decreases with the number of $Pb–CH_3$ linkages. In the methylbutylleads the CH_3^+ abundance is affected by the configuration of the butyl radical as a low CH_3^+ abundance occurs for the *n*-butyl, whereas a high abundance is observed for the tertiary butyl compound.

The abundance of $C_2H_5^+$ ions also follows a logical relation to molecular structure, except in the case of tetraethyllead. Formation of the $C_2H_5^+$ ion by dissociation of the $Pb—C_2H_5$ linkage is relatively less probable than formation of CH_3^+ from $Pb(CH_3)_4$.

The relation of abundance of propyl and butyl ions to molecular structure is evidently complicated. The formation of $C_3H_7^+$ ions is relatively improbable in the tetrapropyl compound, and analogous to the tetraethyllead. The increased abundance in the trimethyl-*tert*-butyllead is unexpected because of the complicated dissociation process involved and the low abundance in the tetra-*iso*-butyllead. The abundance of the $C_4H_9^+$ ion in the *sec*-butyl compound is not consistent with the order of bond energies: primary>secondary>tertiary.

TABLE 2. *Principal ions in the monoisotopic spectra of some lead alkyls* [a]

Ion	$Pb(R^1)_4$	$Pb(R^1)_3(R^2)$	$Pb(R^1)_2(R^3)_2$	$Pb(R^1)(R^3)_3$	$Pb(R^3)_4$	$Pb(R^2)_4$	$Pb(R^1)_3(R^4)$	$Pb(R^1)_2(R^5)$	$Pb(R^1)_3(R^6)$	$Pb(R^7)_4$
CH_3	5.35	3.44	2.06	1.42	0.21	1.45	1.02	2.85	12.5	3.58
C_2H_5	-----	0.96	1.50	1.98	1.57	1.82	4.78	5.57	0.31	2.21
C_3H_7	-----	-----	-----	-----	-----	1.16	0.47	1.41	3.19	0.85
C_4H_9	-----	-----	-----	-----	-----	-----	.97	10.2	2.84	5.17
Pb	69.7	76.1	78.1	72.6	46.2	85.3	76.4	67.4	67.1	86.8
PbH	3.24	16.6	30.1	43.5	39.2	32.8	34.3	21.2	5.74	33.7
$PbCH_2$	6.35	5.93	4.44	1.36	0.63	6.42	6.12	4.68	5.38	6.00
$PbCH_3$	87.8	100.0	95.1	78.6	.60	100.0	99.1	87.1	87.5	100.0
PbC_2H_4	-----	-----	0.72	-----	1.11	27.5	0.23	0.16	-----	1.15
PbC_2H_5	0.53	11.8	31.3	69.6	100.0	14.7	.61	.79	0.91	41.0
PbC_2H_6	25.0	15.0	3.58	0.14	-----	2.79	13.8	10.4	24.0	11.9
PbC_3H_7	-----	3.12	3.46	-----	-----	-----	-----	-----	-----	-----
PbC_3H_7	0.27	0.38	1.43	1.63	0.26	14.0	-----	0.35	-----	3.97
PbC_3H_8	.81	10.0	16.5	17.9	-----	9.69	-----	-----	2.22	13.5
PbC_3H_9	100.0	81.3	3.12	1.42	-----	62.0	100.0	100.0	100.0	49.3
PbC_4H_9	-----	-----	-----	0.19	0.19	1.04	36.5	9.24	0.28	1.61
PbC_4H_{10}	-----	-----	1.67	5.50	14.5	3.54	-----	-----	-----	4.24
PbC_4H_{11}	-----	44.4	100.0	11.9	3.24	34.7	0.32	0.16	-----	42.1
PbC_4H_{13}	-----	-----	18.5	100.0	0.43	23.3	.67	.15	-----	39.5
PbC_5H_{10}	-----	-----	-----	-----	.13	0.66	-----	.55	-----	13.5
PbC_6H_{12}	-----	-----	0.09	-----	76.7	10.0	68.0	27.0	-----	0.36
PbC_6H_{16}	-----	-----	1.06	10.4	0.18	0.27	-----	0.30	-----	-----
PbC_7H_{17}	-----	-----	-----	-----	-----	3.02	-----	-----	-----	1.21
PbC_7H_{18}	-----	-----	-----	0.96	-----	0.46	0.17	1.79	0.10	0.53
PbC_8H_{21}	-----	-----	-----	-----	-----	7.31	-----	-----	-----	.45
$PbC_{12}H_{27}$	-----	-----	-----	-----	-----	-----	-----	-----	-----	.24
Sensitivity relative to *n*-butane *m/e*=43	0.69	0.60	0.89	0.86	1.2	0.72	0.76	0.94	0.95	0.89

[a] $R^1=CH_3$, $R^2=C_2H_5$, $R^3=C_3H_7$, $R^4=n\text{-}C_4H_9$, $R^5=s\text{-}C_4H_9$, $R^6=t\text{-}C_4H_9$, $R^7=iso\text{-}C_4H_9$.

Hydrocarbon ions apparently resulting from rearrangement during ionization-dissociation processes have been noted previously for tetramethyllead [1]. Traces of impurities in the compounds used in this research effectively masked such ions and prevent further discussion concerning their origin.

Lead atom ions are of comparable abundance in all of the compounds. The abundance of PbH^+ ions, although comparable for most of the compounds, is relatively low in the tetramethyllead and the trimethyl-*tert*-butyllead.

The $PbCH_3^+$ ion is one of the principal ions in all of the lead alkyl spectra except tetraethyllead. Although the latter requires rearrangement to form the monomethyllead ion, the tetrapropyllead and tetra-*iso*-butylleads also require rearrangement, and the $PbCH_3^+$ ion is the most abundant ion in the spectra of these compounds.

The abundances of the $PbC_2H_5^+$ ion are generally consistent with the structure of the lead alkyls, e. g., the abundance increases with substitution of ethyl radicals for methyl groups of tetramethyllead. The low abundance of this ion in the methylbutyl compounds is consistent with structure. However, the tetrapropyllead and tetra-*iso*-butyllead compounds are exceptions. Formation of this ion by dissociation of a hydrogen atom from a dimethyllead configuration evidently occurs with low probability.

The abundances of the dimethyllead ion, $PbC_2H_6^+$, are also generally consistent with molecular structure. Increased substitution of ethyl radicals for methyl radicals in the methyl-ethyl leads results in decreased abundance. Formation of this ion in tetrapropyllead and the butyl leads is by rearrangement. The $PbC_2H_7^+$ ions are evidently hydrides of the dimethyllead ion formed by rearrangement.

As expected, the trimethyllead ion, $PbC_3H_9^+$, is abundant for molecules having 3 or 4 methyl groups. The relatively large abundance of this ion observed in the tetrapropyllead and tetra-*iso*-butyllead spectra suggests a dihydride of the monopropyllead $H_2PbC_3H_7^+$. This is suggested by the apparent high stability of the ion configuration, PbR_3^+, in which three bonding orbitals of the central lead atom are occupied by hydrogen atoms or alkyl groups. Such stability is demonstrated by the large abundances of the $Pb(CH_3)_3^+$ ions of tetramethyllead, trimethylethyllead, and the trimethylbutyllead, the $Pb(CH_3)_2C_2H_5^+$ ion of dimethyldiethyllead, the $Pb(CH_3)(C_2H_5)_2^+$ ion of methyltriethyllead and the $Pb(C_2H_5)_3^+$ ion of tetraethyllead. Tetrapropyllead and tetra-*iso*-butyllead are evidently exceptions to this, probably for steric reasons. However, the trimethyl-*n*-butyllead spectrum includes an abundant ion, $PbC_6H_{15}^+$, which very probably has the trialkyl configuration, $Pb(CH_3)_3C_4H_9$.

Ions heavier than $PbC_6H_{15}^+$ are relatively rare. Molecule ions of only five of the lead alkyls were observed with abundances as large as 1 percent of the most abundant ion. This fact complicates the mass spectrometer analysis of mixtures of these compounds, particularly for those containing small amounts of lower molecular weight compounds.

5. References

[1] V. H. Dibeler, J. Research NBS **49,** 235 (1952) RP2358.
[2] V. H. Dibeler and F. L. Mohler, J. Research NBS **47,** 337 (1951) RP2259.
[3] L. Friedman, A. P. Irsa, and G. Wilkinson, J. Am. Chem. Soc. **77,** 3689 (1955).
[4] R. M. Farquhar, G. H. Palmer, and K. L. Aitken, Nature **172,** 860 (1953).
[5] V. H. Dibeler, Anal. Chem. **27,** 1958 (1955).
[6] R. C. Taylor and W. S. Young, Ind. Eng. Chem., Anal. Ed. **17,** 811 (1945).
[7] E. M. Charlet, Consolidated Electrodynamics Corp., Pasadena, Calif., Group Report No. 14 (March 1950).
[8] Catalog of mass spectral data, American Petroleum Institute, Carnegie Institute of Technology, Pittsburgh, Pa. (1952).

WASHINGTON, March 15, 1956.

Journal of Research of the National Bureau of Standards Vol. 57, No. 1, July 1956 Research Paper 2693

Frequency Response of Second-Order Systems With Combined Coulomb and Viscous Damping[1]

Thomas A. Perls[2] and Emile S. Sherrard

Curves obtained with an analog computer are presented for the magnification factor versus frequency ratio of second-order systems with combined coulomb and viscous damping. The ranges of the parameters are as follows: Viscous damping ratio from 0.05 to 5.0, in 15 steps; coulomb damping ratio from 0 to 0.9, in 11 steps; and frequency ratio from 0 to 2.0. Boundaries between regions with 0, 1, and 2 stops per half-cycle are also shown.

1. Introduction

The increasing importance of vibration measurements for both military and nonmilitary applications has stimulated the production of a large variety of vibration-measuring instruments in recent years. This activity in design and manufacture has not been matched by progress in the analysis of the response of vibration instruments, or in the extension or modernization of previous analyses of their response. It is still frequently assumed, in the application of these instruments, that the response of an actual vibration instrument is identical with the response of an ideal instrument in which the damping is entirely "viscous," i. e., proportional to the velocity of the mass or "seismic element." The actual response may differ significantly from the ideal response if the damping varies with other than the first power of the velocity, or is dependent on displacement, or if any appreciable amount of coulomb damping is present. This last type of damping, sometimes referred to as dry or sliding friction, exerts on the moving element a force that is constant in magnitude and always acts in the direction opposite to the velocity of the moving element.

Coulomb damping is usually present in a mechanical second-order system such as is illustrated in figure 1. Here, in addition to the coulomb damping, a spring force and a viscous damping force are shown as acting upon the seismic element. The motion of such a system has been analyzed by Den Hartog[3] in a 1931 paper in which results are presented graphically in a series of figures. For application to vibration instruments in present use, Den Hartog's results require extension to larger values of viscous friction and a larger range of frequencies.

The present paper extends these results through the ranges applicable to such inertial instruments as accelerometers and jerkmeters. These inertial instruments are usually designed for viscous damping between 0.6 and 0.7 of critical damping, and are usually employed between zero frequency and a maximum frequency less than the resonance frequency (of the mass and spring). Particular emphasis is therefore placed in this paper upon results for viscous damping between 0.6 and 0.7 of critical damping, and for frequencies between zero and the resonance frequency.

Results are presented graphically in figures 2 to 17. These curves extend from zero to twice resonance frequency, and are presented so as to be readily applicable to vibration instruments used below their resonance frequency. They were determined without particular difficulty through the use of an analog computer. The original program called for the computation of an additional set of curves for frequencies between twice the resonance frequency and 50 times the resonance frequency. These curves would have been applicable to devices such as seismometers and velocity meters, which are ordinarily employed at frequencies above their resonance frequency. Unfortunately, the analog computer accuracy proved poor at these high frequencies. The computation of displacement at high frequencies consisted essentially of the double integration of the difference of a sinusoidal forcing function and the coulomb friction. When the analog computer attempted this double integration, its results contained appreciable errors caused by drifting and hunting. The size of these errors caused a termination of the high-frequency computations. Hence, only curves applicable to vibration instruments usually employed below their resonance frequency are presented in this paper.

[1] This work was conducted under a program of basic instrumentation research and development sponsored by the National Bureau of Standards, the Office of Naval Research, the Air Research and Development Command and the Atomic Energy Commission.

[2] Now at the Missile Systems Division ,Lockheed Aircraft Corp., Van Nuys, Calif.

[3] J. P. Den Hartog, Forced vibrations with combined coulomb and viscou friction, Trans. Am. Soc. Mech. Eng. **53**, APM 53-9, 107–115 (1931).

2. Differential Equation for Vibration Instruments

Figure 1 shows a typical vibration instrument with its frame rigidly attached to a sinusoidally vibrating structure having a motion $X \cos \omega t$. The displacement, x, of the seismic element relative to the frame of the instrument satisfies the differential equation:

$$M\ddot{x}+C\dot{x}+Kx\pm F=MX\omega^2 \cos \omega t, \qquad (1)$$

where (see fig. 1)

M=mass of seismic element.
C=viscous damping force per unit velocity.
K=restoring force exerted by the spring per unit displacement.
F=coulomb damping force, assumed constant in magnitude and changing sign so as always to oppose the motion.
X=amplitude of forcing motion.
$\omega=2\pi f$=angular frequency of forcing motion.

A number of equations in Den Hartog's paper give a complete literal solution of this equation with the right-hand side of the equation replaced by a term $P \cos (\omega t+\varphi)$, where P is the amplitude of a "periodic disturbing force." For practical application Den Hartog expressed his results by a set of computed curves of magnification factor versus frequency ratio for seven values of viscous damping ratio between 0 and 0.5 of critical damping, and for a number of values between 0 and 0.9 of the ratio of coulomb damping force to peak disturbing force. Most of Den Hartog's curves extend over a frequency range of 0.5 to 2.0; the one for zero viscous damping extends over a frequency range of 0 to 2.0. Curves for zero coulomb damping (i. e., viscous damping only) are also available elsewhere.[4] In the present paper, all the curves extend over the frequency ratio range between 0 and 2.0. They are given for 15 values of viscous damping ratio between 0.05 and 5.0, and for 11 values of coulomb damping ratio between 0 and 0.9.

3. Summary of Results

The curves shown in figures 2 to 17 are drawn through points plotted by an analog computer. Each figure presents a family of curves for a constant value of C/C_c, the ratio of viscous damping C, to critical viscous damping, $C_c=2\sqrt{KM}$. Each curve of the family is a plot of magnification factor or acceleration response $x_0\omega_n^2/\ddot{X}$ versus the frequency ratio, ω/ω_n, where x_0 is the maximum value of the displacement x, $\omega_n=\sqrt{K/M}$ is the undamped resonance frequency of the mass-spring system, and $\ddot{X}=\omega^2 x$ is the peak acceleration of the forcing motion. For inertial instruments, the term "acceleration response" seems appropriate for $x_0\omega_n^2/\ddot{X}$ because this quantity may be interpreted as the product of two important instrument characteristics: $x_0/\ddot{X}$, the response (displacement) of the seismic element per unit acceleration applied to the instrument, and ω_n^2, the resonance frequency of the instrument, to which instrument sensitivity is inversely proportional.

Each curve of the family is drawn for a particular value of the parameter $a_F/\ddot{X}$, where a_F is the minimum acceleration that must be applied to the instrument to overcome coulomb friction and produce motion. This parameter $a_F/\ddot{X}$ is equivalent to the parameter F/P used by Den Hartog. Either may be obtained from the other by employing the relations $F=Ma_F$ and $P=M\ddot{X}$.

The dashed line plotted in each figure is a boundary line between steady-state motions with no stop and one stop per half-cycle. In the region above this boundary, the steady-state motion is continuous without stops. In the region immediately below this boundary, the motion stops once each half-cycle.

Only these two regions, nonstop and one-stop motion, were computed for $C/C_c \geq 0.2$ and $\omega/\omega_n \geq 0.1$. For $C/C_c \leq 0.1$, four regions characterized by no stop, one stop, two stops, or more than two stops each half-cycle were computed. When more than two regions occur, the magnification factor versus frequency ratio curves become very irregular for ω/ω_n less than about 0.4. For $\omega/\omega_n \leq 0.1$, larger and larger amounts of computing time would be required for accurately determining the magnification factor as C/C_c becomes smaller and smaller. Hence for $C/C_c=0.2$, 0.1, and 0.05, the curves are terminated at $\omega/\omega_n=0.1$.

4. Accuracy of Results

The curves of figures 2 to 17 are plotted to permit reading the magnification factor to within 1 percent of the full scale of each figure. These curves were drawn through points plotted by an analog computer. Over-all accuracy of the points plotted by the analog computer, which consisted of elements with an accuracy of ± 0.1 percent of rated output, is estimated at ± 0.3 percent of the full-scale magnification factor. A number of check points computed manually and by the computer agreed with each other to within ± 1.0 percent. Total computer errors and drafting errors are believed to introduce, in any figure, inaccuracies of no more than 1 percent of the full-scale magnification factor of each figure.

It is believed that greater accuracy in computation would have resulted from the use of a digital computer that employed Den Hartog's literal equations. However, an estimate of total costs showed

[4] See, for example, C. S. Draper, W. McKay, and S. Lees, Instrument engineering. II. Mathematics (McGraw-Hill Book Co., Inc., New York, N. Y., 1953).

analog computation to be more economical. One reason was the availability in the analog computer's auxiliary equipment of a plotting board, which could partially process the results of the computer study by plotting points of the magnification-factor curves. The other important important advantage of the analog computer was its use of eq (1) rather than the involved literal equations of Den Hartog's paper, which would have been employed by the digital computer. Use of the analog computer avoided the expenditures necessary for a careful scrutiny of these equations for possible misprints.

5. General Effects of Coulomb Friction Upon Instrument Response

The presence of coulomb friction makes instrument response dependent on the amplitude of the sinusoidal excitation. This amplitude dependence is shown graphically in figure 18, which is a cross-plot of the data for $C/C_c=0.65$, as given in figure 10. In figure 18, magnification factor is plotted versus $\ddot{X}/a_F$ for various constant values of ω/ω_n.

The asymptotes shown as horizontal lines in the right-hand portion of figure 18 represent the magnification factors at vibration amplitudes sufficiently large to make negligible the effect of coulomb friction. An inspection of the figure shows that, for $C/C_c=0.65$, $\ddot{X}/a_F$ must be ≥ 25 if the actual response is to be within 5 percent of the asymptote for all values of $\omega \leq \omega_n$.

Rules similar to this can be stated for other values of C/C_c. For $C/C_c \geq 0.3$ and for $0 \leq \omega/\omega_n \leq 1.0$, a general rule of thumb for estimating the error introduced by coulomb friction is to assume that this error is equal to the error at $\omega/\omega_n=0$. According to this general rule, a given percentage value of $a_F/\ddot{X}$ results in that same percentage reduction of magnification factor from its ideal ($a_F/\ddot{X}=0$) value. This rule is a good approximation for the reduction in response for C/C_c in the range 0.6 to 0.7. As the value of C/C_c moves further and further outside this range, the approximation becomes poorer and poorer. However, the damping in most inertial instruments is between 0.6 and 0.7 of critical damping; hence, this rule is useful for practical inertial instruments.

A physical example of the effect of coulomb fraction upon instrument response is shown in figure 19. This figure reproduces an oscillogram from two different velocity meters mounted back to back and subjected to the same sinusoidal forcing function. The upper trace shows that one instrument is stopping once each half-cycle as the result of coulomb friction. The lower trace shows the other to be exhibiting essentially ideal behavior.

Figure 20 shows the time variation of displacement and velocity for various values of $a_F/\ddot{X}$, for a low value of viscous friction ($C/C_c=0.1$), and a low value of frequency ratio ($\omega/\omega_n=0.1$). These records were made during the computer study. Each set of two traces is for a different value of $a_F/\ddot{X}$. At $a_F/\ddot{X}=0.3$, one-stop motion occurs, as evidenced by the long dwell of the velocity trace on the (central) zero line. For $a_F/\ddot{X}$ equal to 0.5, the second trough of the damped sinusoidal oscillation in the velocity trace approaches the zero line. At $a_F/\ddot{X}=0.525$, this trough reaches the zero, and the motion stops twice during each half-cycle. Further increase of $a_F/\ddot{X}$ to 0.55 furnishes an additional restraint, which prevents another start after the motion stops at nearly the same point of the velocity trough. Thus we have again one stop per half-cycle. The motion remains one-stop until displacement and velocity decrease sufficiently for a stop to occur at the first trough of the velocity, giving two-stop motion once more. This occurs at approximately $a_F/\ddot{X}=0.8$. However, an increase of $a_F/\ddot{X}$ to 0.9 furnishes the additional restraint necessary to prevent another start. Thus motion again becomes one-stop.

As C/C_c decreases from 0.1, the damped sinusoid of velocity becomes less damped and it is conceivable that for $\omega/\omega_n \leq 0.1$, motion may stop not only at the third, second, or first trough of the velocity, but also at a fourth, fifth, or higher-order trough of the velocity. In such cases, the response of the instrument becomes very irregular.

The analog computer study was performed by W. McCool and B. Zimmerman of the Naval Research Laboratory. The authors thank Messrs. McCool and Zimmerman for their suggestions and excellent cooperation in this study. M. Abramowitz and R. Dressler supplied information on the use of the digital computer. W. A. Wildhack continually furnished stimulating ideas during the investigation. A. Bucek prepared the curves and illustrations shown in this report.

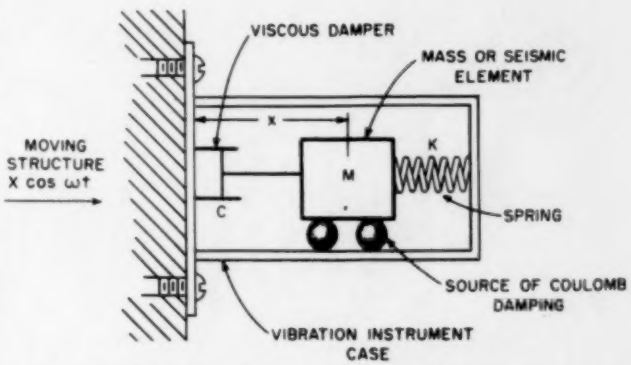

FIGURE 1. *Typical mechanical vibration instrument.*

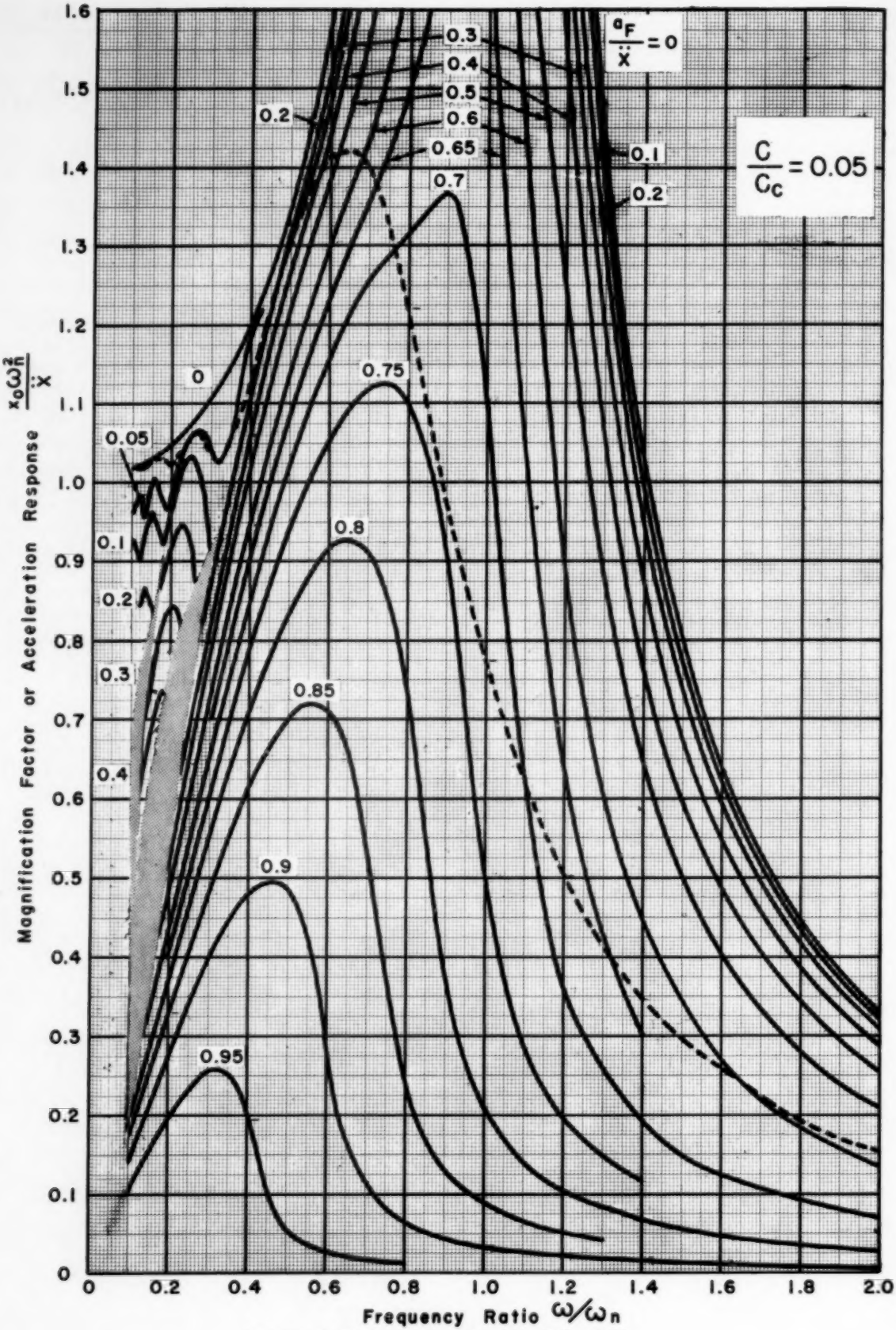

FIGURE 2. *Instrument response for $C/C_c = 0.05$.*

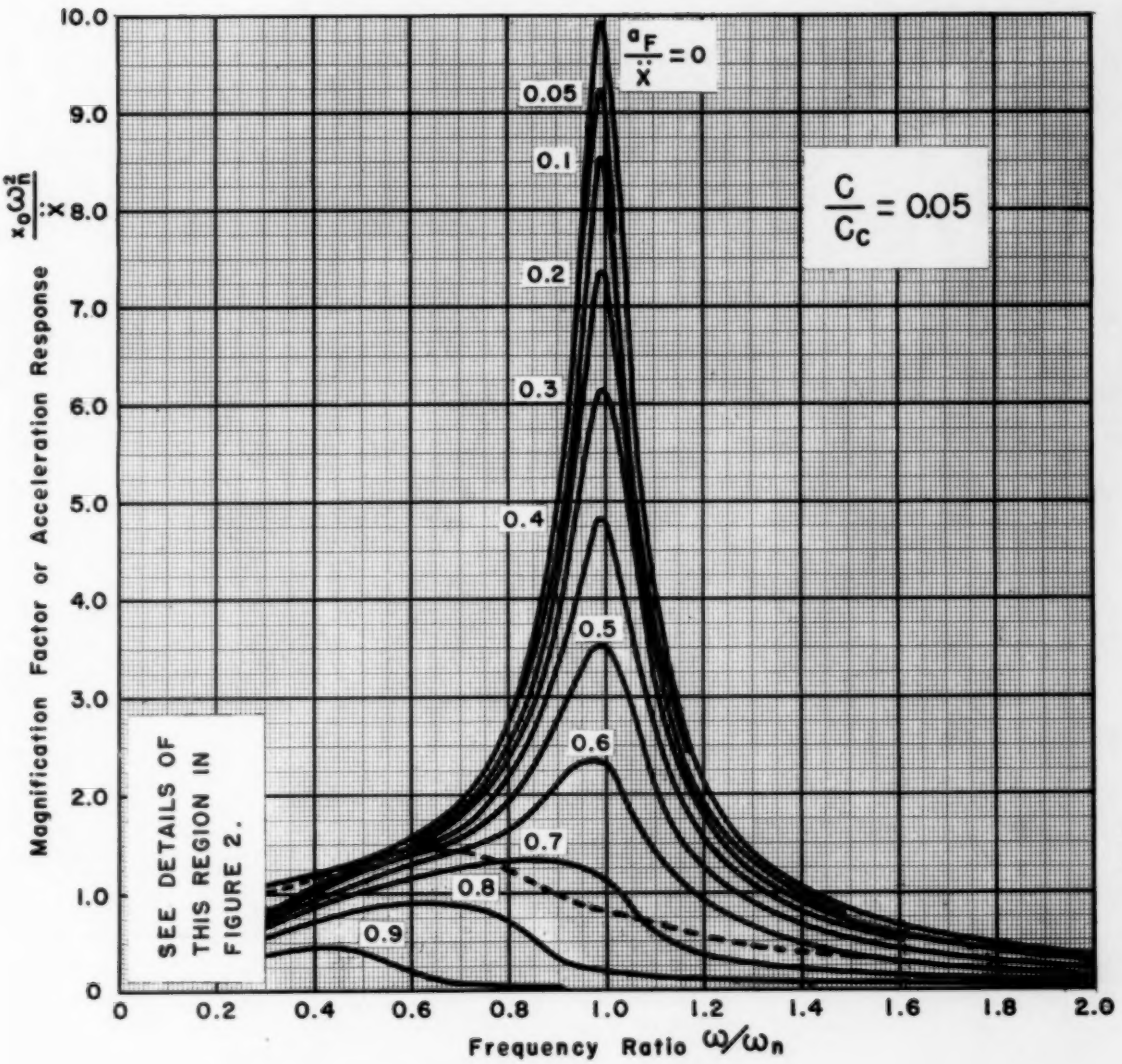

FIGURE 3. *Instrument response for $C/C_c = 0.05$.*

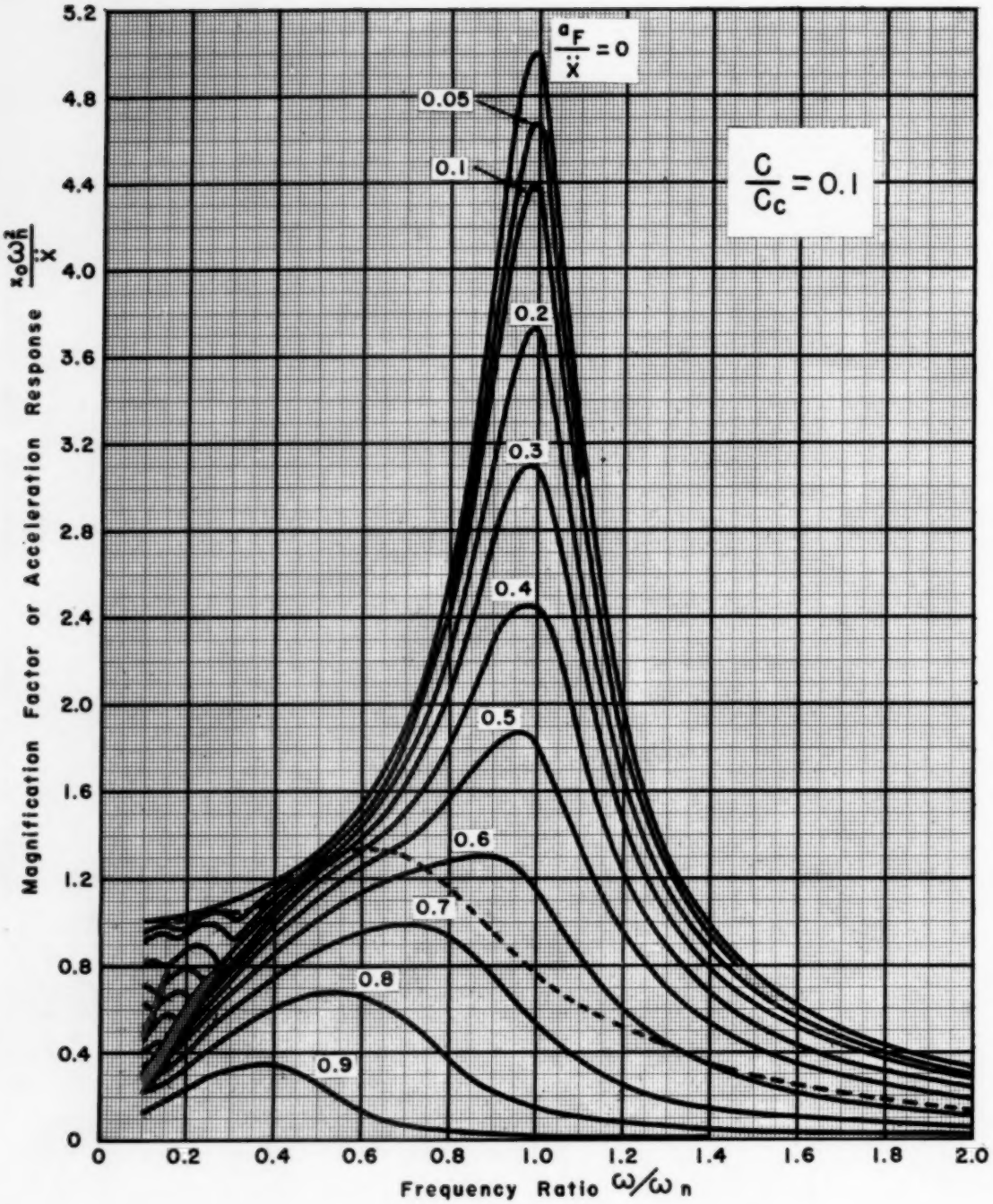

FIGURE 4. *Instrument response for* $C/C_c = 0.10$.

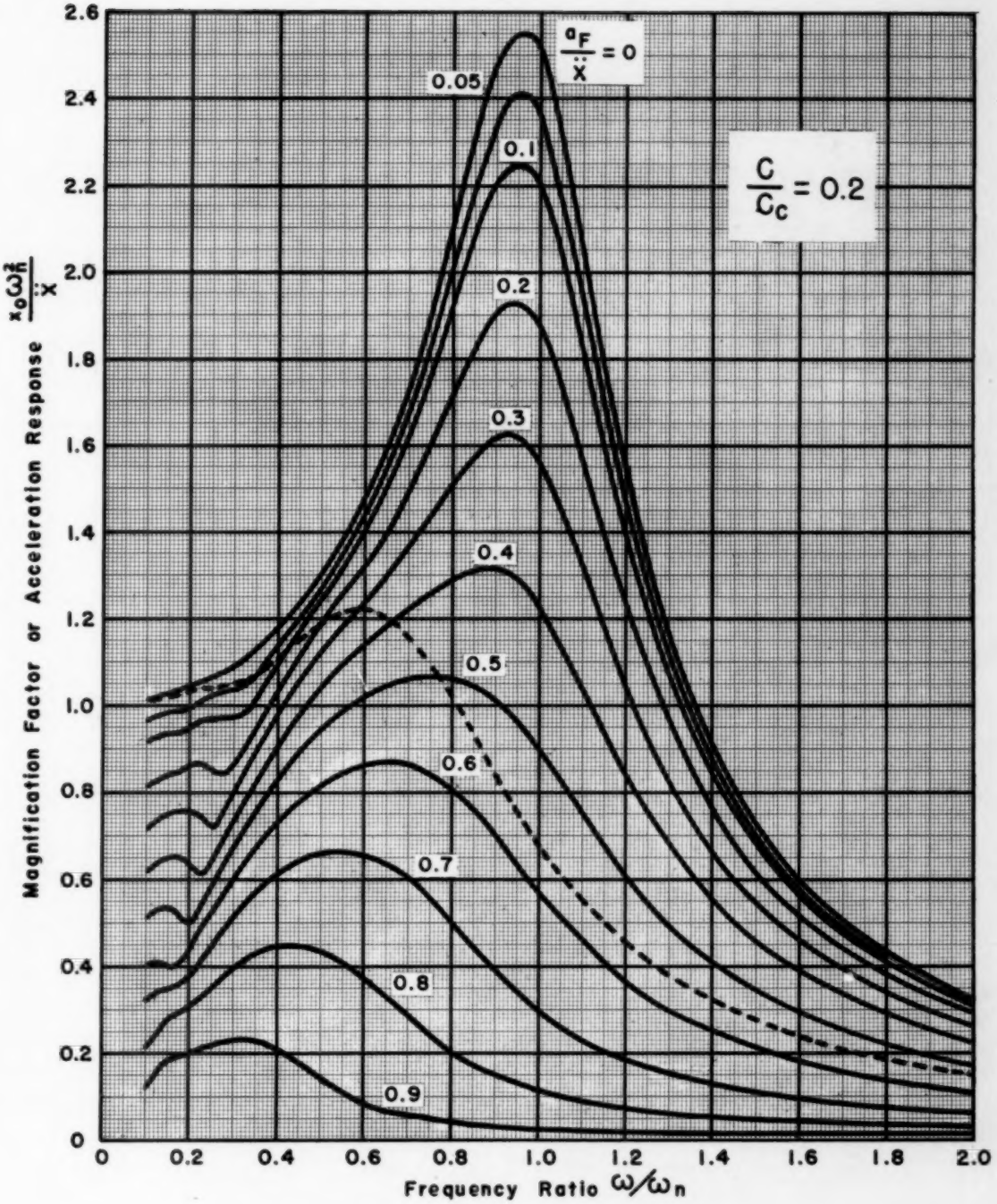

FIGURE 5. *Instrument response for* $C/C_c = 0.20$.

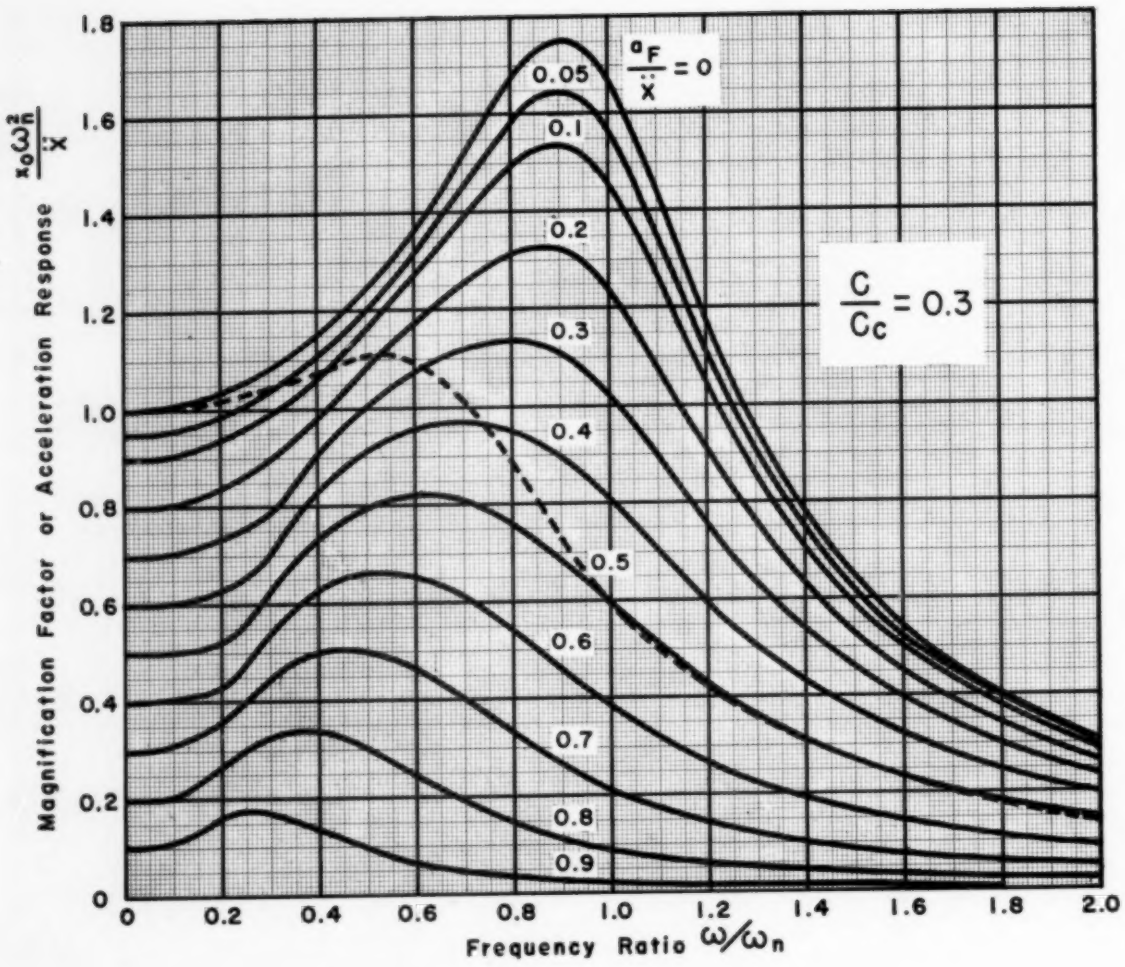

FIGURE 6. *Instrument response for* $C/C_c = 0.30$.

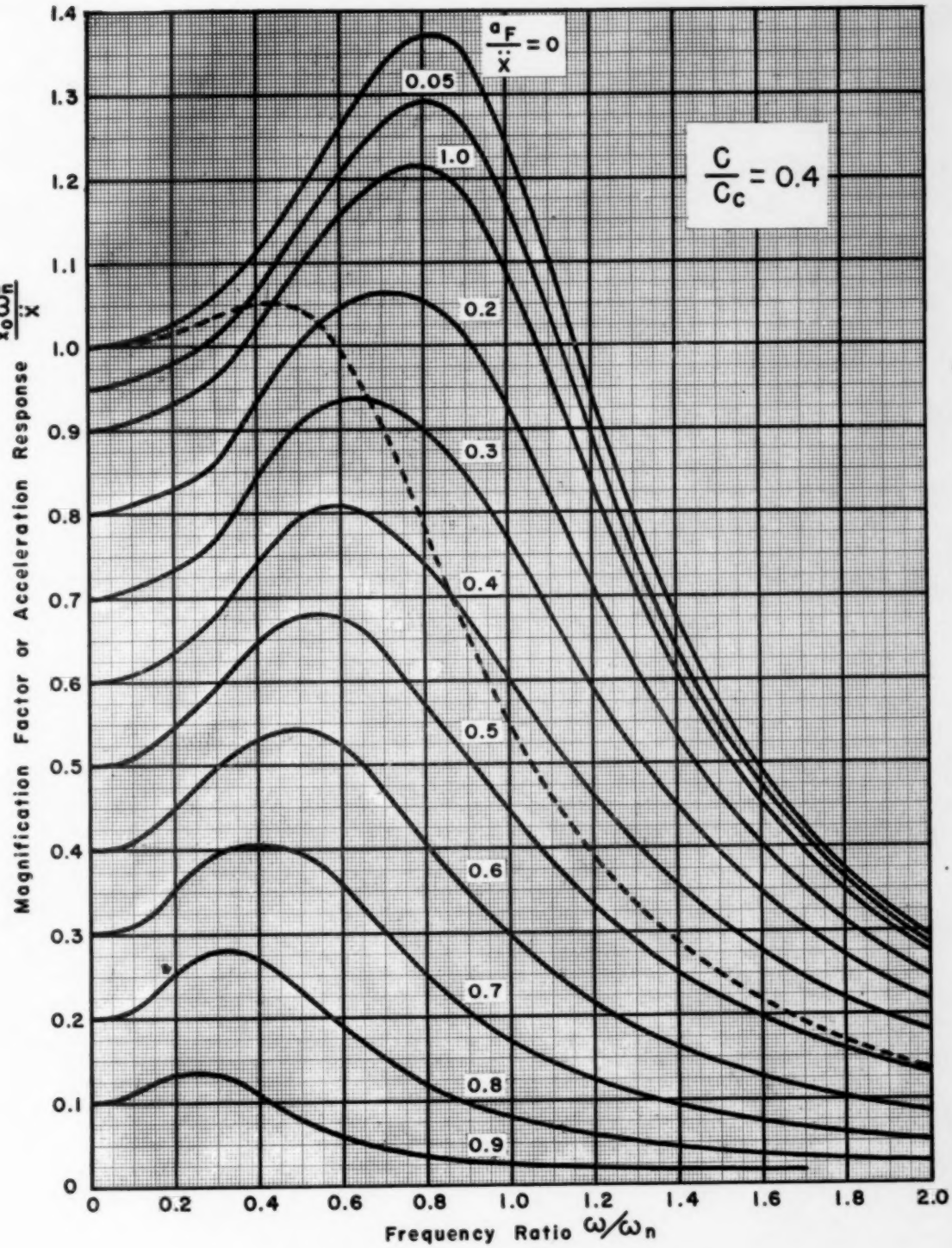

FIGURE 7. *Instrument response for* $C/C_c = 0.40$.

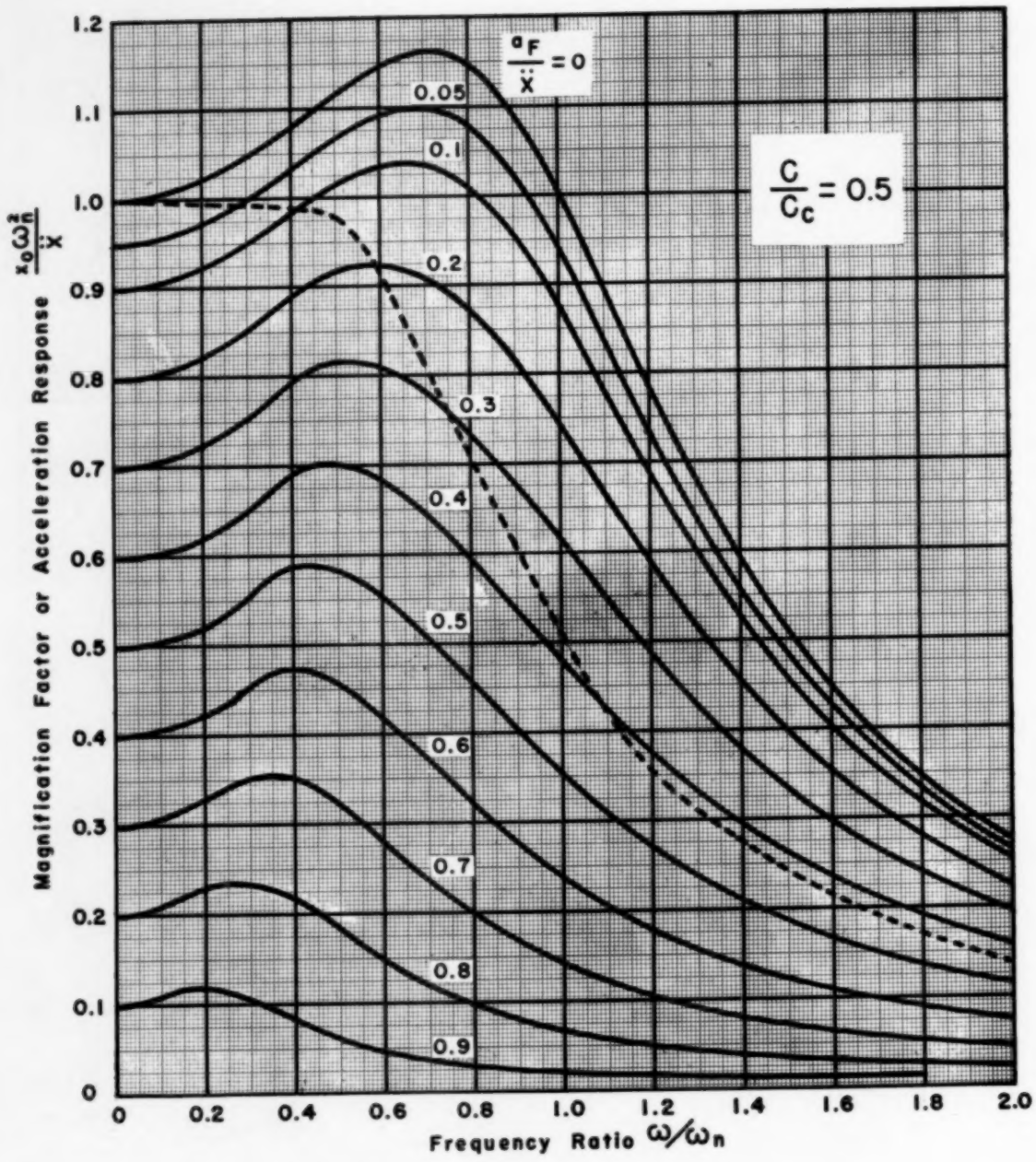

FIGURE 8. *Instrument response for $C/C_c=0.50$.*

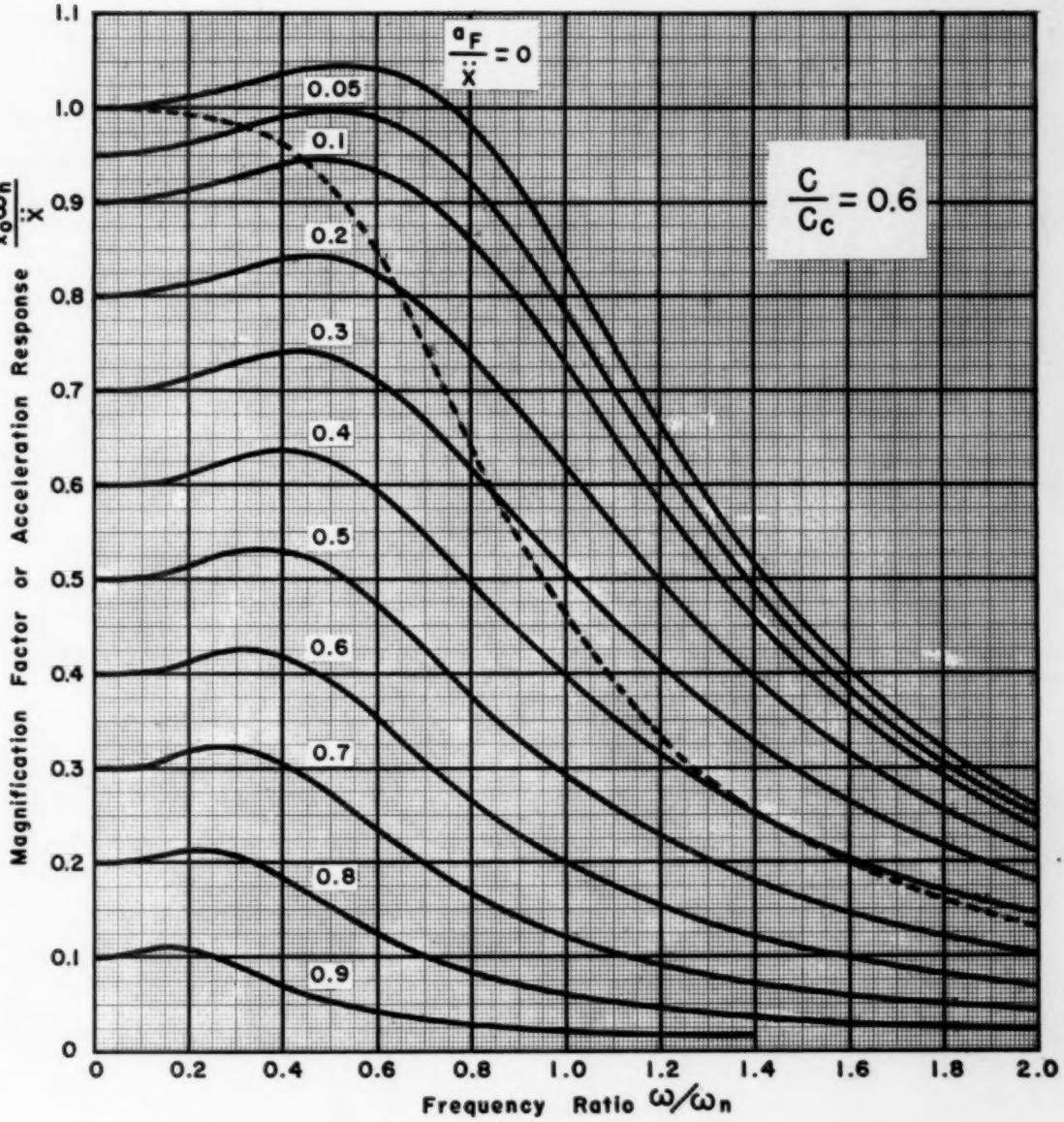

FIGURE 9. *Instrument response for* $C/C_c = 0.60$.

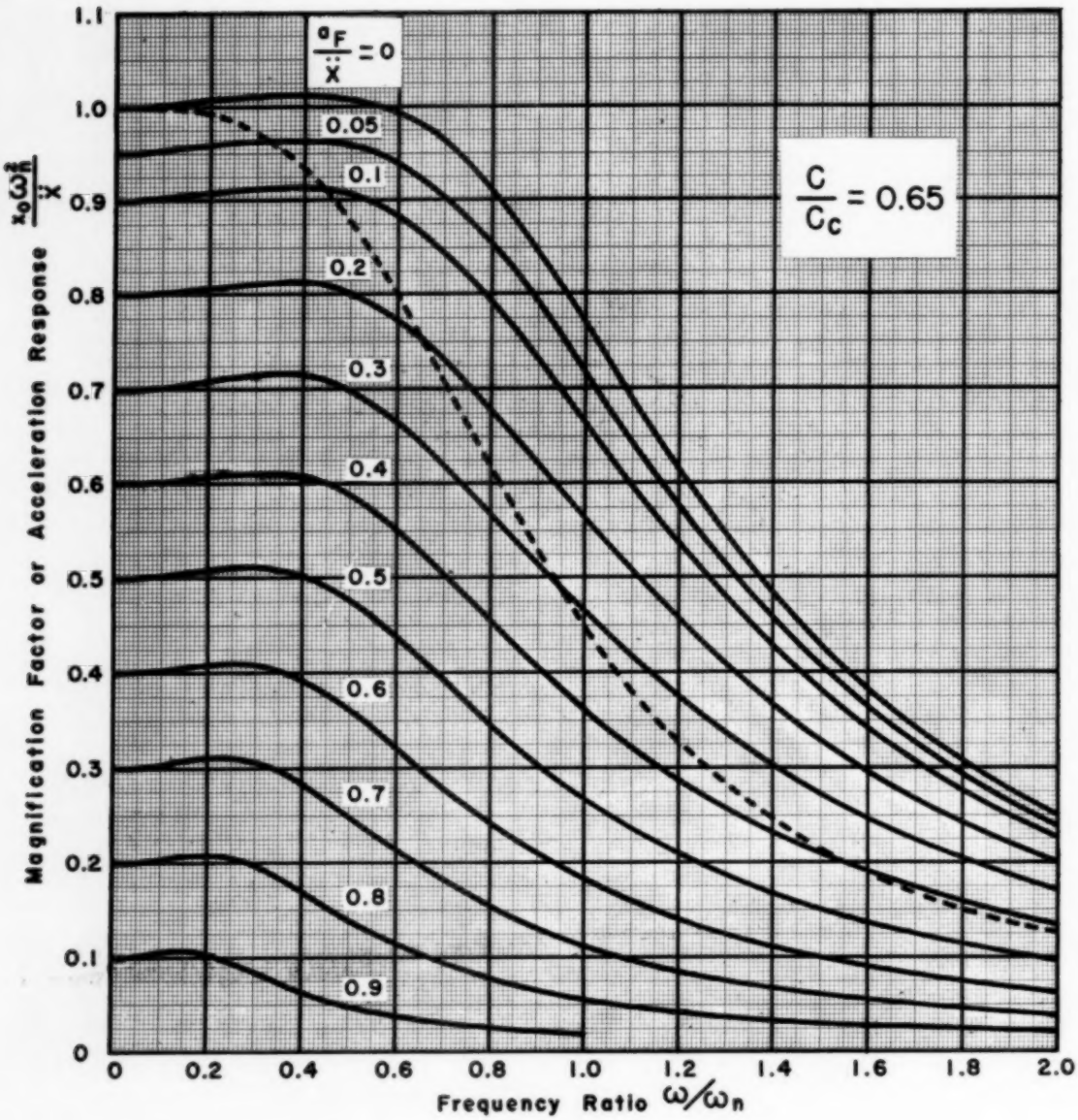

FIGURE 10. *Instrument response for $C/C_c=0.65$.*

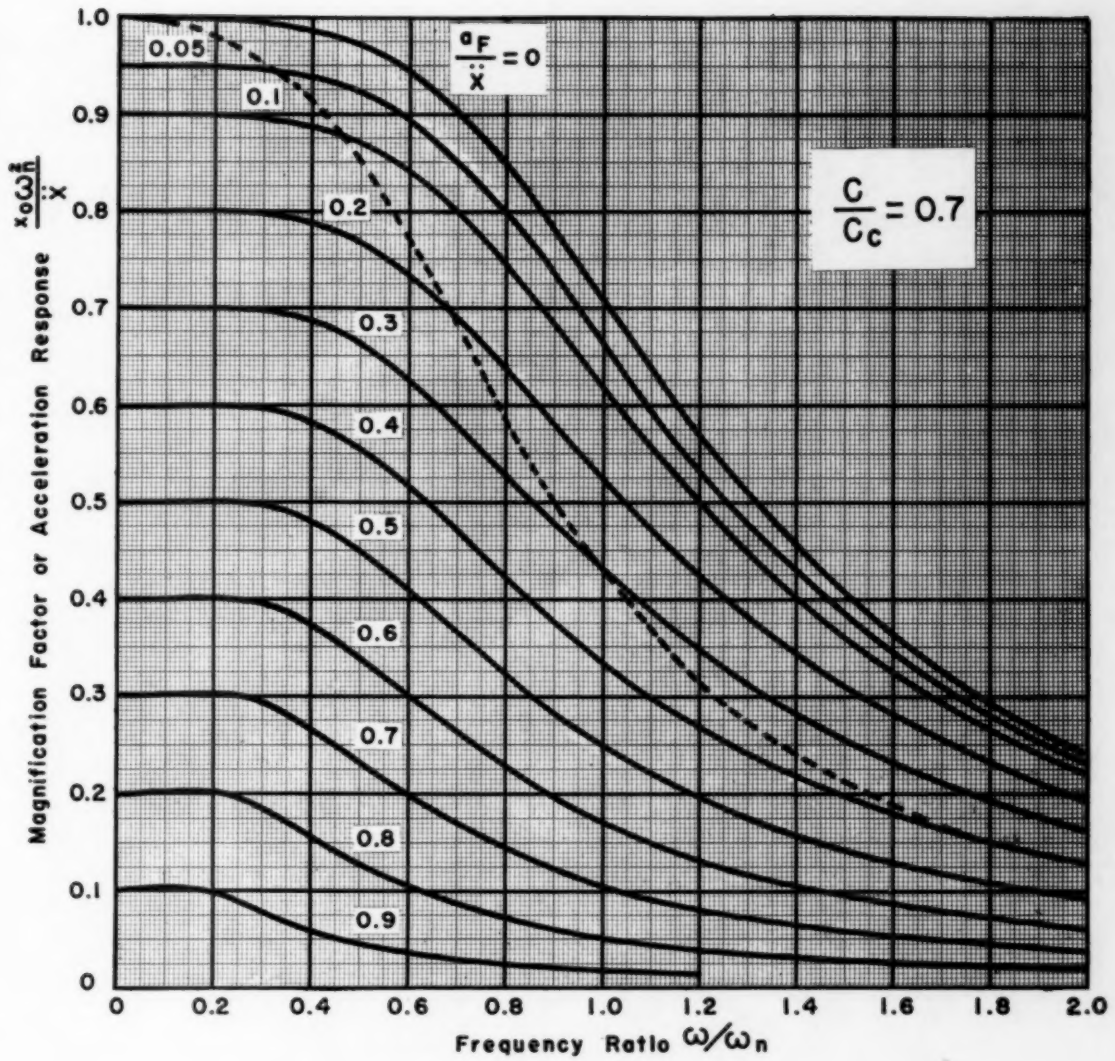

FIGURE 11. *Instrument response for* $C/C_c = 0.70$.

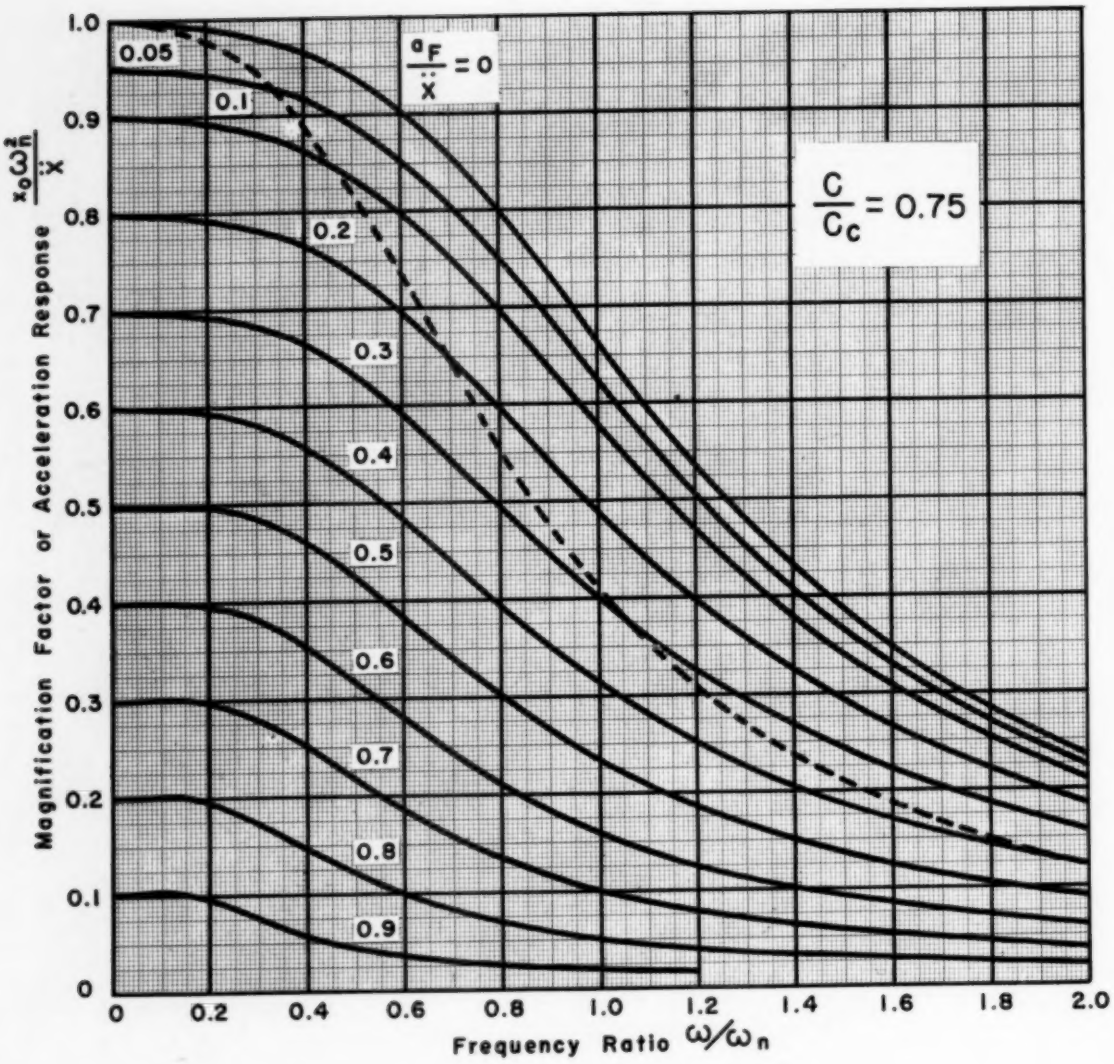

FIGURE 12. *Instrument response for $C/C_c=0.75$.*

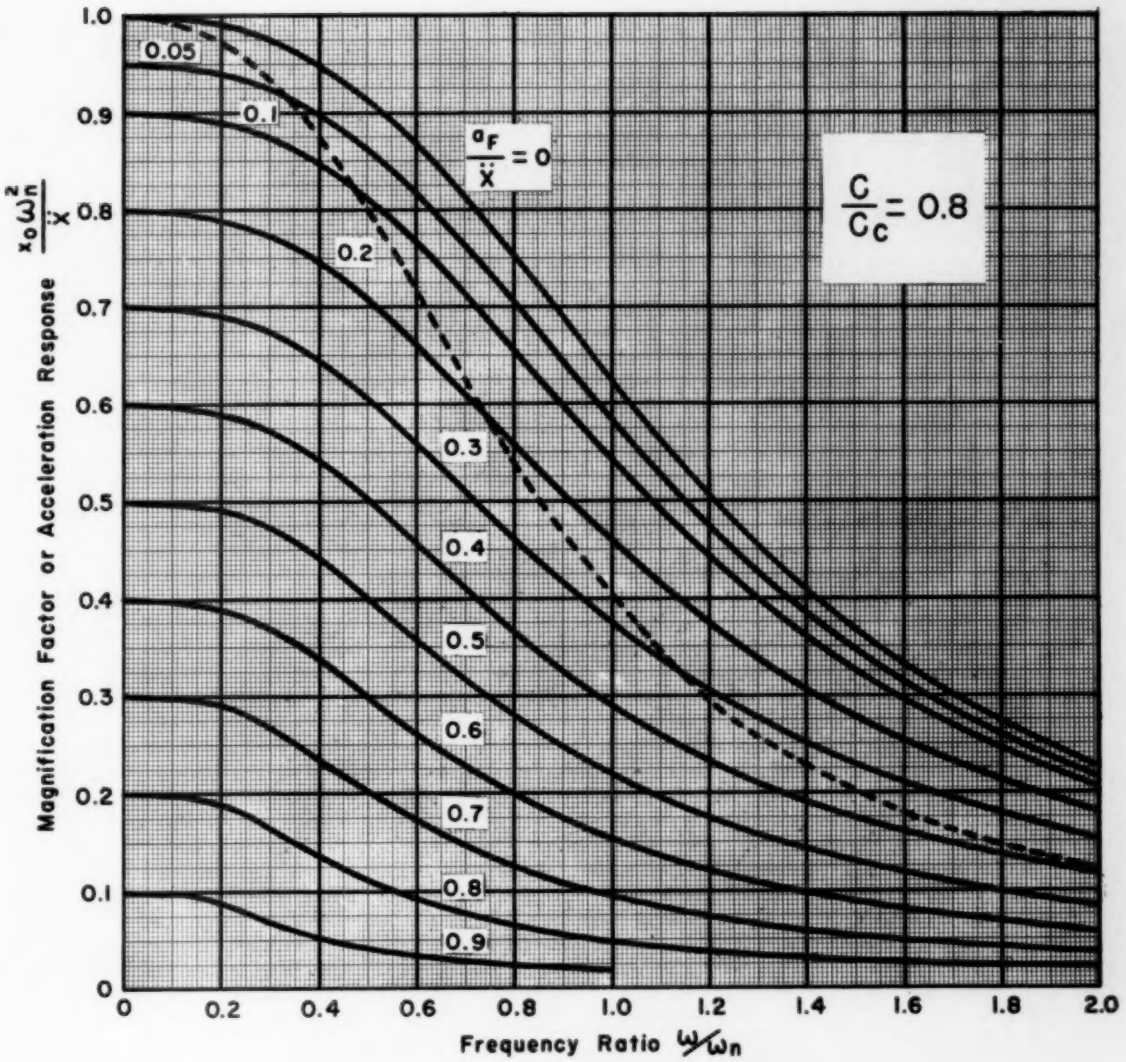

FIGURE 13. *Instrument response for* $C/C_c = 0.80$.

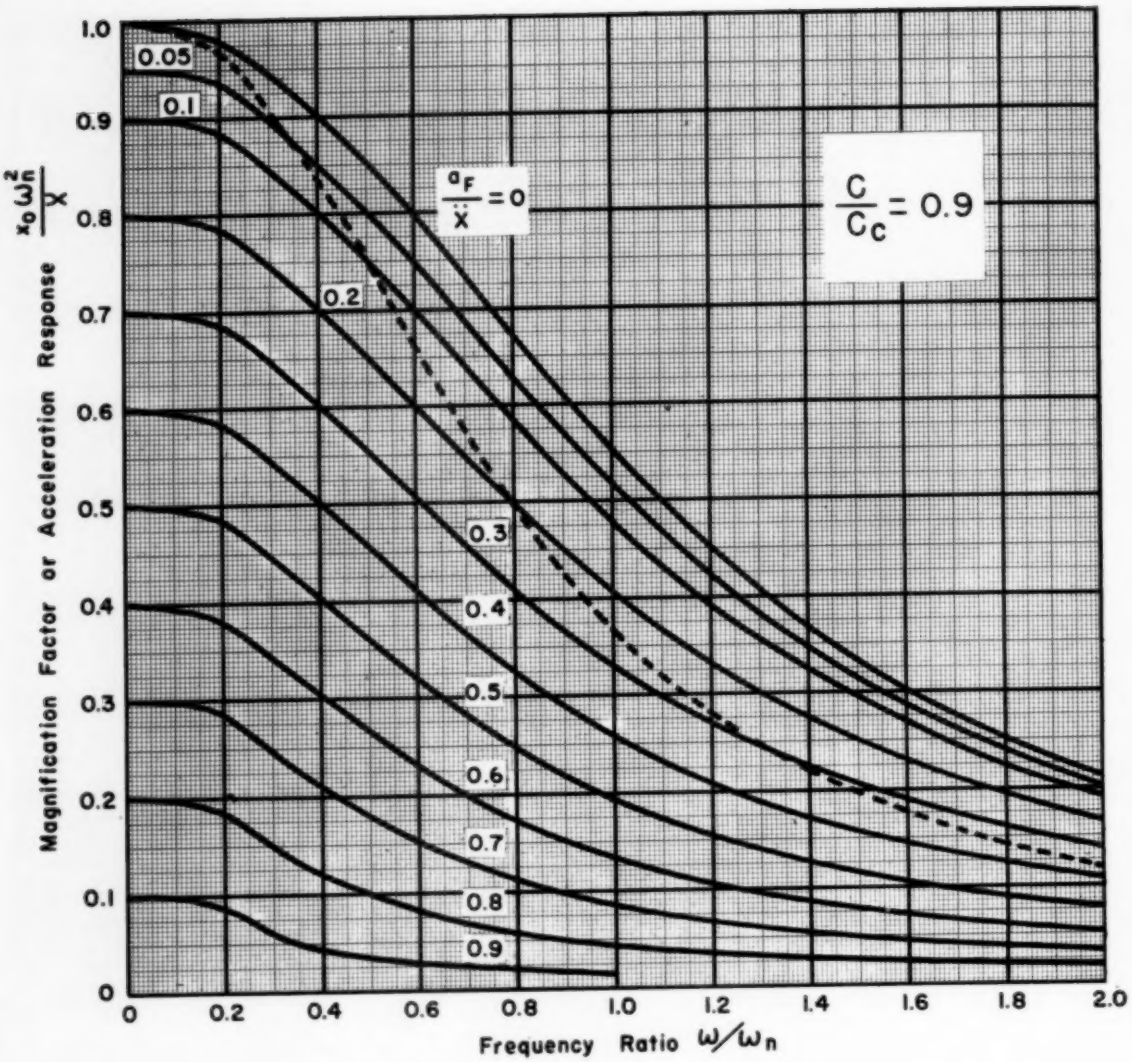

FIGURE 14. *Instrument response for $C/C_c = 0.90$.*

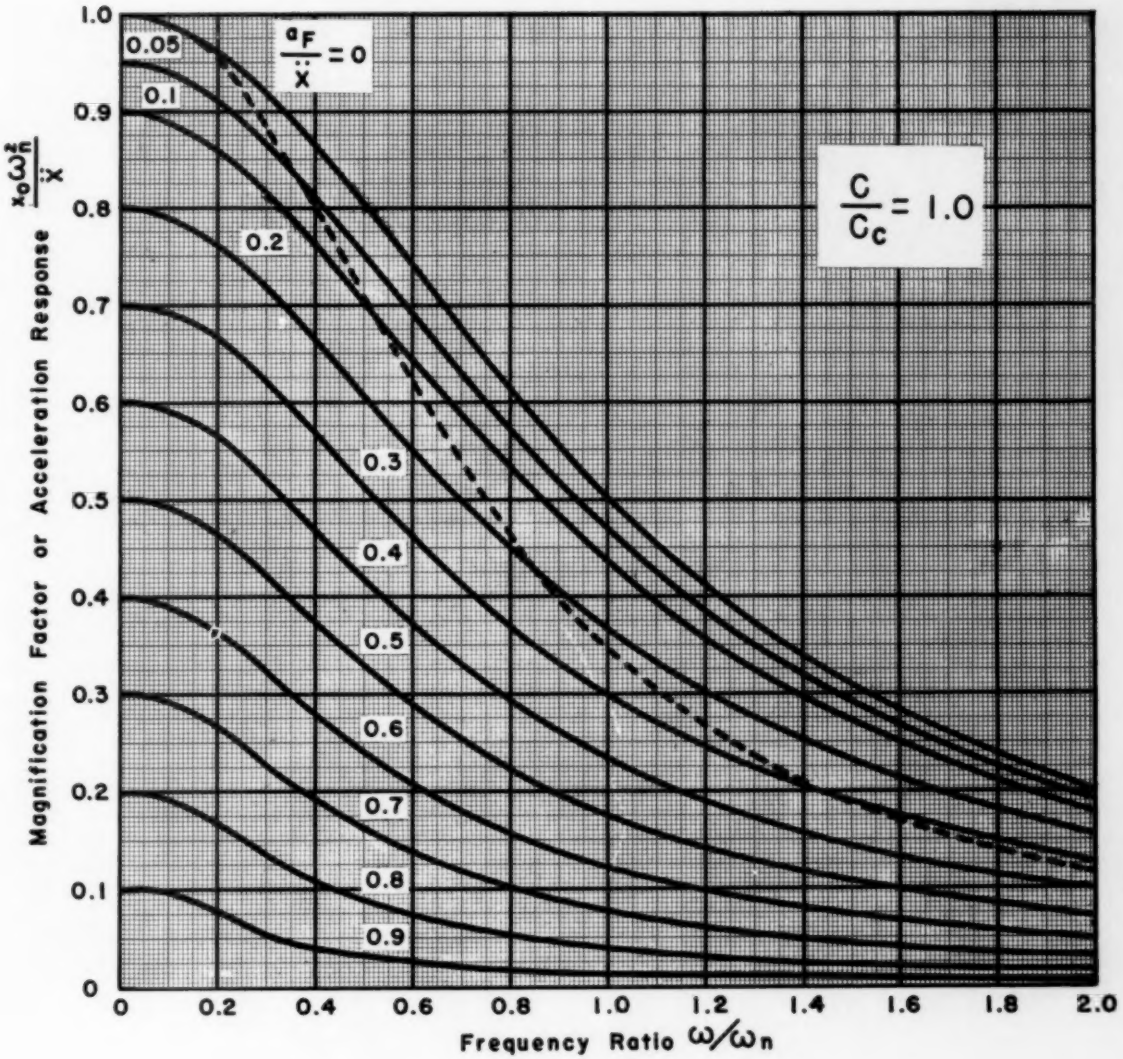

FIGURE 15. *Instrument response for* $C/C_c = 1.0$.

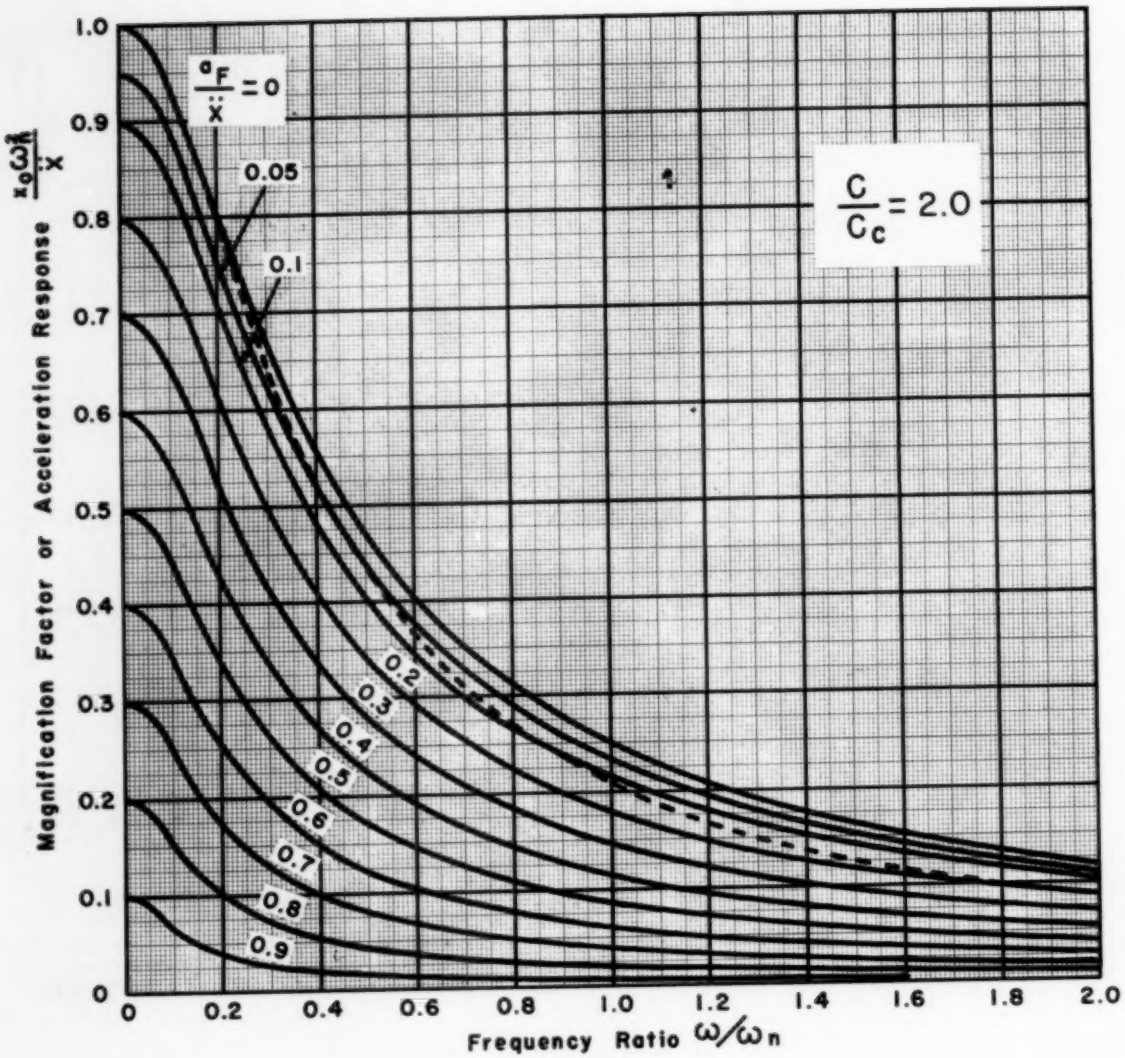

FIGURE 16. *Instrument response for $C/C_c = 2.0$.*

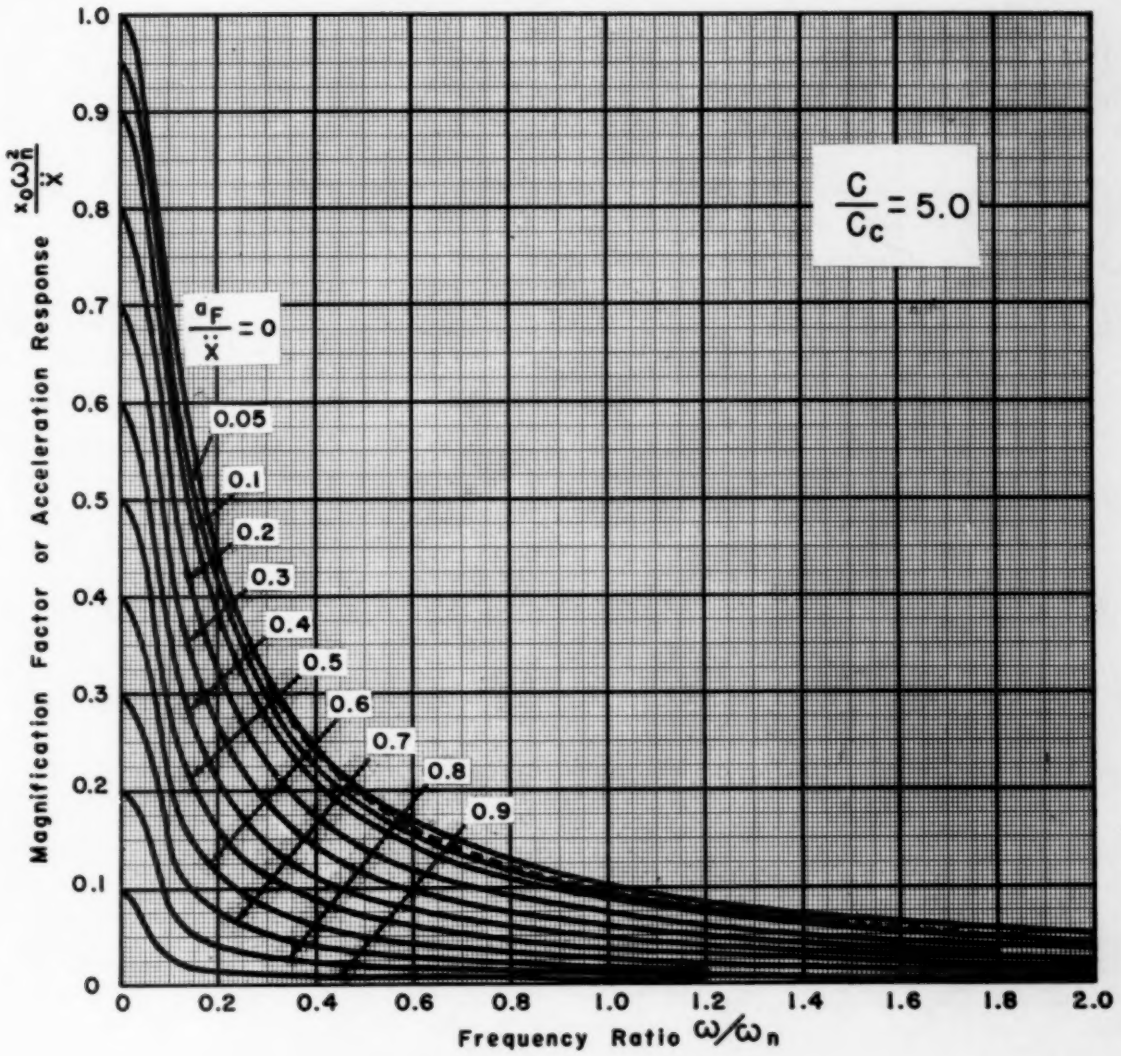

FIGURE 17. *Instrument response for $C/C_c=5.0$.*

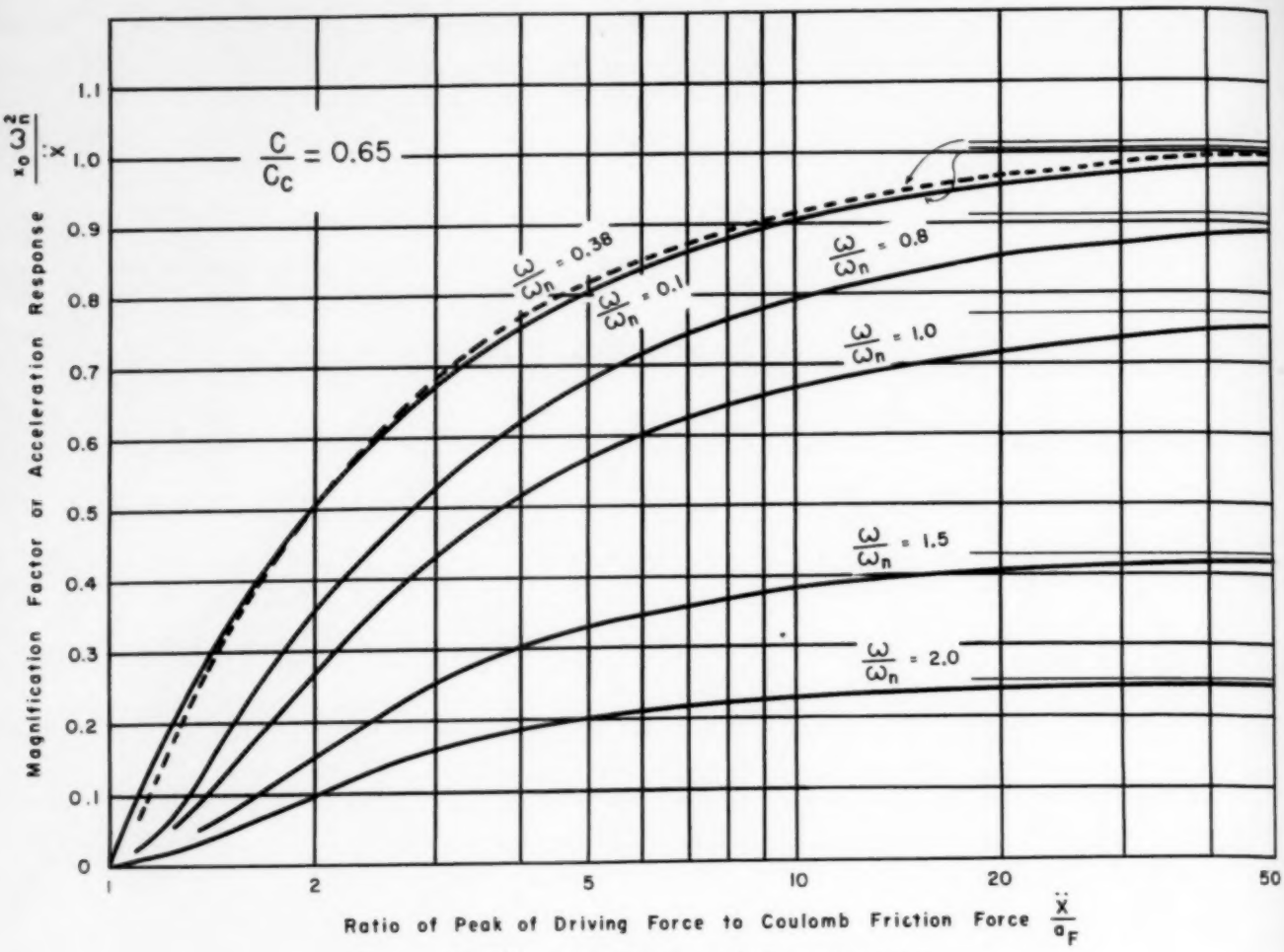

FIGURE 18. *Effect of amplitude upon instrument response.*

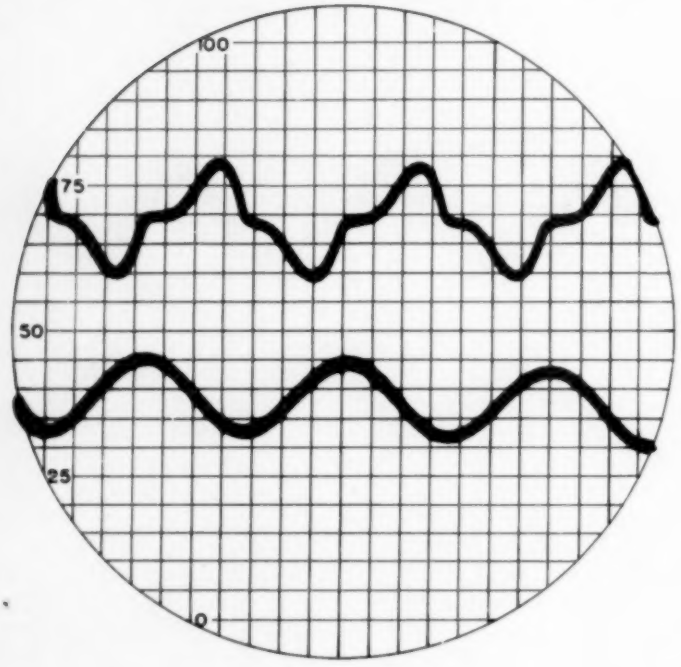

FIGURE 19. *Experimental response of two different vibration instruments.*

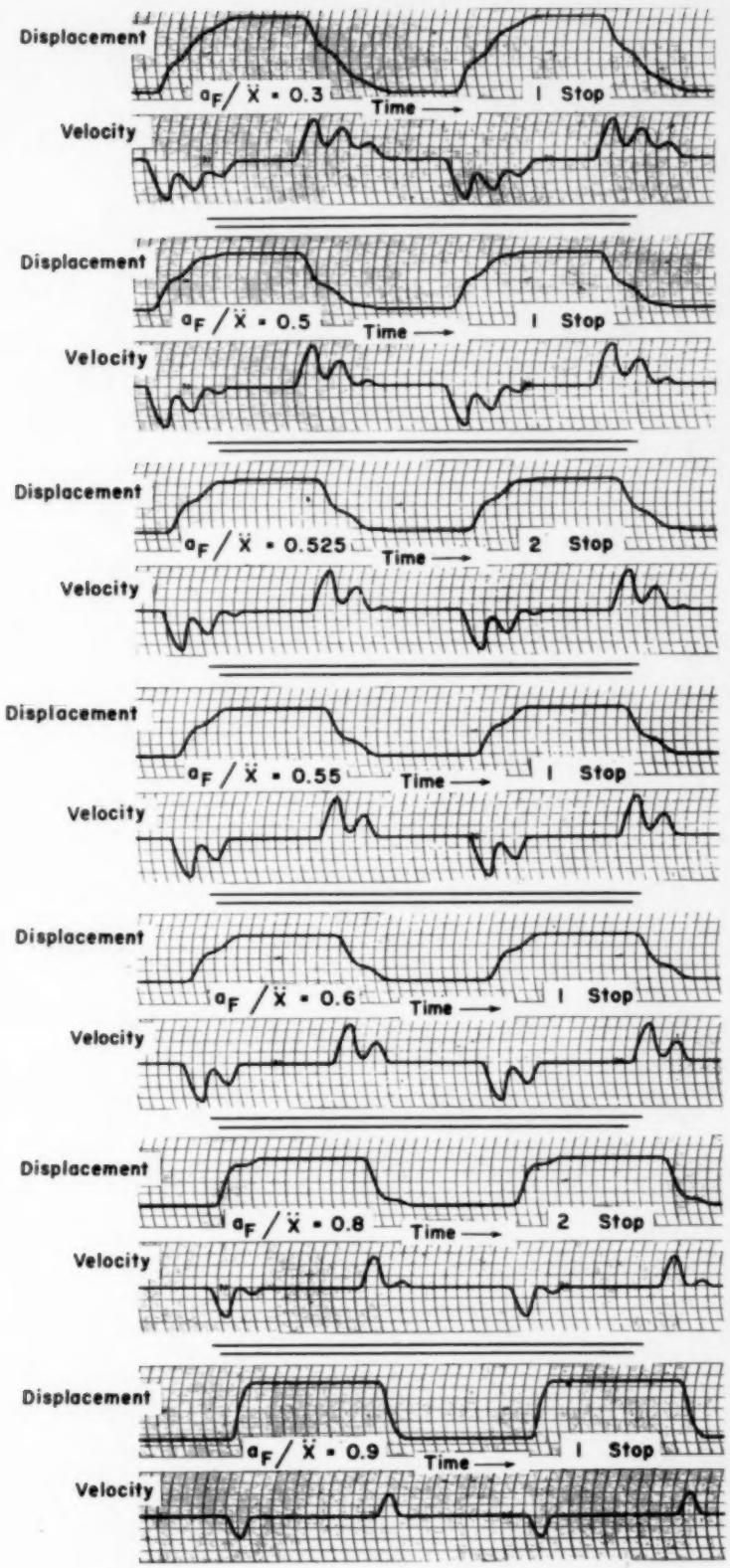

FIGURE 20. *Computed response of vibration instrument.*

WASHINGTON, April 3, 1956.

Recent Publications of the National Bureau of Standards

Journal of Research of the National Bureau of Standards, volume **56**, No. 5, May 1956 (RP2672 to RP2679, incl.). Annual subscription $4.00.

Technical News Bulletin, volume **40**, No. 5, May 1956. 10 cents. Annual subscription $1.00.

Basic Radio Propagation Predictions for August 1956. Three months in advance. CRPL 141. Issued May 1956. 10 cents. Annual subscription $1.00.

Research Papers

Journal of Research, volume 56, No. 5, May 1956. Single copies of the Journal vary in price. Single copies of Research Papers appearing in the Journal are not available for sale. The Superintendent of Documents, U. S. Government Printing Office, Washington 25, D. C., will reprint 100 or more copies of a Research Paper. Requests for the purchase price should be mailed promptly to that office.

RP2672. Characteristics of an image-forming system. Roland V. Shack.

RP2673. Advances in the design and application of the radiofrequency permeameter. Alvin L. Rasmussen, Albert W. Enfield, and Alfred Hess.

RP2674. A new computer for calculating the water content of gases. A. W. Diniak and E. R. Weaver.

RP2675. Vibrational constants of acetylene-d_2. Harry C. Allen, Jr., L. R. Blaine, and Earle K. Plyler.

RP2676. Heat capacity of polyisobutylene from 0° to 380° K. George T. Furukawa and Martin L. Reilly.

RP2677. Preparation of barium titanyl oxalate tetrahydrate for conversion to barium titanate of high purity. W. Stanley Clabaugh, Edward M. Swiggard, and Raleigh Gilchrist.

RP2678. A five-band recording spectroradiometer. C. S. McCamy.

RP2679. Polarographic determination of lead and cadmium in zinc-base alloys, using electrolytic separations at controlled potential. John K. Taylor and Stanley W. Smith.

Circulars

C566. Bibliography of solid adsorbents. Victor Deitz. $3.75.

C571. Electron physics tables. L. Marton, C. Marton, and W. G. Hall. 50 cents.

Building Materials and Structures Reports

BMS145. Fire effects and fire controls in nitrocellulose photographic-film storage. J. V. Ryan, J. W. Cummings, and A. C. Hutton. 20 cents.

Publications in Other Journals

Measurements on the saturation vapour pressure of liquid helium in the range 1.4° K–4.2° K. E. Ambler and R. P. Hudson. Bul. Inter. Inst. Refrig. (177 Blvd. Malesherbes, Paris (17e), France) Commun. 147, 605 (Sept. 2–8, 1955).

High-speed machine computation of ideal gas thermodynamic functions. I. The isotopic water molecules. Abraham S. Friedman and Lester Haar. J. Chem. Phys. (57 E. 55th St., New York 22, N. Y.) **23**, No. 12, 2351 (Dec. 1954).

High-speed machine computation of ideal gas thermodynamic functions. II. The diatomic free radicals of the isotopic hydrides of oxygen and sulfur. Lester Haar and A. S. Friedman. J. Chem. Phys. (57 E. 55th St., New York 22, N. Y.) **23**, No. 5, 869 (1955).

Electron affinity of atomic oxygen. Lewis M. Branscomb and Stephen J. Smith. Phys. Rev. (57 E. 55th St., New York 22, N. Y.) **98**, No. 4, 1028 (1955).

Experimental cross section for photodetachment of electrons from H^- and D^-. Lewis M. Branscomb and Stephen J. Smith. Phys. Rev. (57 E. 55th St., New York 22, N. Y.) **98**, No. 4, 1028 (1955).

Cycle strain tester for leather. T. J. Kilduff and J. R. Kanagy. J. Am. Leather Chemists' Assoc. (Univ. of Cincinnati, Cincinnati 21, Ohio) **50**, No. 10, 489 (1955).

Magnetic cooling. E. Ambler and R. P. Hudson. Proc. Phys. Soc. (London) (1 Lowther Gardens, Prince Consort Rd., London SW7, England) **18**, 251 (1955).

Pairs of matrices with property L. II(1). T. S. Motzkin and Olga Taussky. Trans. Am. Math. Soc. (80 Waterman St., Providence, R. I.) **80**, No. 2, 387–401 (Nov. 1955).

A bend-test method of determining the stress required to cause creep in tension. J. B. Wachtman, Jr., and L. H. Maxwell. Am. Soc. Testing Materials (1916 Race St., Philadelphia 3, Pa.) Bulletin No. 211, (Jan. 1956).

On generating functions of the Jacobi polynomials. Peter Henrici. Pacific J. Math. (Univ. of Calif. Press, Berkeley and Los Angeles, Calif.) **5**, Supplement 2 (1955).

Transient fields of a vertical dipole over a homogeneous curved ground. James R. Wait. Can. J. Phys. (National Research Council, Ottawa, Canada) **34**, 27–35 (1956).

The normalizer of certain nodular subgroups. Morris Newman. Can. J. Math. (Univ. of Toronto, Toronto, Ontario, Canada) **8**, No. 1, 29–31 (1956).

Commutator for periodically changing the direction and magnitude of direct currents. F. Ogburn and H. Salmon. Plating (The American Electroplaters' Society, American Bldg., 445 Broad St., Newark 2, N. J.) **43**, 343 (1956).

Publications for which a price is indicated are available only from the Superintendent of Documents, U. S. Government Printing Office, Washington 25, D. C. (foreign postage, one-third additional). Reprints from outside journals are not available from the National Bureau of Standards but can often be obtained from the publishers.

UNIVERSITY OF MICHIGAN
GENERAL LIBRARY
DOCUMENTS DIVISION
1276 ANN ARBOR MICH

UNITED STATES
GOVERNMENT PRINTING OFFICE
DIVISION OF PUBLIC DOCUMENTS
WASHINGTON 25, D. C.

OFFICIAL BUSINESS

PENALTY FOR PRIVATE USE TO AVOID PAYMENT OF POSTAGE, $300 (GPO)

Journal of Research of the National Bureau of Standards Vol. 57, No. 1 July 1956

Contents

		Page
Mixed path ground wave propagation: 1. Short distances. James R. Wait.	RP2687	1
Effect of object frequency on focal position of four photographic objectives. Fred W. Rosberry.	RP2688	17
An examination of the 1955 helium vapor-pressure scales of temperature. E. Ambler and R. P. Hudson.	RP2689	23
Heats of formation of xonotlite, hillebrandite, and foshagite. Edwin S. Newman.	RP2690	27
Effect of camera tipping on the location of the principal point. Francis E. Washer.	RP2691	31
Mass spectra of some lead alkyls. Edith I. Quinn, Vernon H. Dibeler, and Fred L. Mohler.	RP2692	41
Frequency response of second-order systems with combined coulomb and viscous damping. Thomas A. Perls and Emile S. Sherrard.	RP2693	45

Single copies of the above Research Papers are not available for sale, but the Superintendent of Documents, U. S. Government Printing Office, Washington 25, D. C., will reprint 100 or more copies, and request for the purchase price should be mailed promptly to that Office.

[A list of recent NBS publications is given on page 3 of the cover.]

For sale by the Superintendent of Documents, U. S. Government Printing Office, Washington 25, D. C. Price 60 cents (single copy). Subscription price: $4.00 a year; $1.25 additional for foreign mailing. Single copies vary in price.

UNITED STATES GOVERNMENT PRINTING OFFICE, WASHINGTON : 1956